UNIVERSITÉ DE STRASBOURG

THÈSE

présentée par :

Xiaopo ZHENG

soutenue le : **07 Octobre 2020**

pour obtenir le grade de : **Docteur de l'université de Strasbourg**

Discipline : Sciences de l'imagerie

Spécialité : Télédétection

Land surface temperature retrieval in urban areas from high spatial resolution thermal infrared data

THÈSE dirigée par :

   M. Zhao-Liang LI   Directeur de Recherches, CNRS, France

RAPPORTEURS :

   M. J. SOBRINO   Professeur, Université de Valence, Espagne

   M. X. BRIOTTET   Directeur de Recherches, ONERA, France

AUTRES MEMBRES DU JURY :

   Mme F. NERRY   Directeur de Recherches, CNRS, France

   M. H.WU   Directeur de Recherches, CAS, Chine

   Mme J. LABED   Maître de Conférence, UdS, France

   M. B-H. TANG   Directeur de Recherches, CAS, Chine

II

Acknowledgements

From the very beginning of my thesis, which should be the day that I applied for this doctoral position, to the very end of this wonderful journey, there are so many people I wish to acknowledge with my sincere gratitude.

First and foremost, I would like to extend my sincerest thanks to my supervisor Pr. Zhao-Liang LI. During my doctoral study, I cannot remember how many difficulties and frustrations I have ever met, but each time, I can get professional instructions and precious suggestions from Pr. LI. I am very impressed and inspired by his conscientious academic spirit, immense knowledge, and open-minded personality. With his continuous guidance, I can finally finish my thesis.

Second, I would like to thank my dearest colleagues in our team – TRIO/ICube - for being so kind and generous. Special thanks to Pr. NERRY Françoise, Pr. ZALLAT Jihad, Pr. YÉSOU Hervé, Pr. Jérôme COLIN, and Dr. Laure Roupioz for their kind help during my research and for teaching me French.

Third, I would like to thank the reporters of my thesis, M. J. SOBRINO and M. X. BRIOTTET; and the jury members, Mme F. NERRY, M. H.WU, Mme J. LABED, and M. B-H. TANG; for their valuable comments, which are really helpful for this thesis as well as for my future researches.

Four, I would like to thank all the Ph.D students I met here in France: Xinke ZHONG, Xiaojing HAN, Yuanyuan CHEN, Ye YUAN, Shuangqi TANG, Jianming YANG, Lihong LIU, Wenhui YU, Chenchen LIU, Hongyu LI, Wenping YU, Xiangyang LIU, Yazhen JIANG, Menglin SI, Jing LI, Zefeng XING, Lei HE, Mingsong LI, Xinyu LAN, Ling WU, Ying YANG, Changsen ZHAO, et. al, for their help, encouragement, and the memorable times we have spent together. Special thanks to three of my best friends: Ronghai HU, Xiucheng YANG, and Fujiao TANG, for their very kind assistants at the very beginning of my doctoral study, even before I arrived in France. With their help, I could get adapt to the new life quickly.

Five, the financial support by China Scholarship Council (CSC) is quite appreciated. Besides, I would also like to thank my two guarantors when signing the contract with CSC: Pr. Huazhong REN and Dr. Zhongling GAO. Without their generous help, I can never get

the opportunity to complete my doctoral study in France.

Last but not least, I would like to thank my family: my grandparents, my parents, my sister and brother-in-law, my fiancée, et. al, for their unconditional support, sacrifices, self-giving care, and endless love, which enable me to focus on my study and research. I also would like to thank everyone I met and everything I experienced. Maybe they are not mentioned here, but they are always in my heart.

Finally, I would like to finish with a Chinese proverb as self-encouragement:

"As heaven maintains vigor through movements, a gentle man should constantly strive for self-perfection.

As earth's condition is receptive devotion, a gentle man should hold the outer world with broad mind."

Abstract

Land surface temperature (LST) is one of the most important Earth System Data, which could be used to characterize the Earth surface processes relating to the energy and hydrology balance. Thus, it is required in a variety of the researches including the monitoring of the urban environment, which requires the accurate urban LST as one of the most essential input parameters. However, there are still some factors influencing the LST retrieval accuracy in urban areas especially for high spatial resolution satellite TIR measurements but have not been well addressed in existing LST retrieval algorithms yet: (1) the adjacency effect in the TIR spectral region; (2) the impact of the three-dimensional (3-D) structures and their radiation on the TIR measurements; (3) the dependence of the existing LST retrieval algorithms on the accurate prior knowledge of the atmosphere and/or the Earth surface emissivity. This thesis is dedicated to developing an improved LST retrieval method for high spatial resolution satellite TIR measurements of urban areas with consideration of these three factors. Firstly, the forward adjacency effect radiative transfer model (FAERTM) has been developed to provide a useful tool for correcting the adjacency effect; Then, the analytical thermal infrared radiative transfer model over urban areas (ATIMOU) has been deduced to help to address the impact of the 3-D structures and their radiation. Next, the prior-knowledge-free (PKF) LST retrieval method has been developed to get rid of the dependence on accurate atmospheric parameters and/or the Earth surface emissivity during the LST retrieval. Finally, the preliminary exploration on developing an improved LST retrieval method for high spatial resolution satellite TIR measurements of urban areas has been given. Results show that the urban LST could be retrieved with a RMSE of 3.33 K if the PKF LST retrieval method has been applied to the urban TOA measurements directly. When implementing the improved LST retrieval method, the urban LST retrieval RMSE decreases to 1.06 K, indicating the good performance of the improved LST retrieval method for high spatial resolution TIR measurements of urban areas, in which the three mentioned factors influencing the LST retrieval accuracy in urban areas have been addressed by the proposed FAERTM, ATIMOU, and PKF LST retrieval method respectively.

Keywords: LST, TIR, radiative transfer, adjacency effect, three-dimensional

Résumé

La température de la surface terrestre (LST) est l'une des données les plus importantes du système terrestre, qui pourrait être utilisée pour caractériser les processus de la surface de la Terre liés à l'équilibre énergétique et hydrologique. Ainsi, il est requis dans une variété de recherches, y compris la surveillance de l'environnement urbain, qui nécessite la LST urbain précis comme l'un des paramètres d'entrée les plus essentiels. Cependant, certains facteurs influencent encore la précision de la récupération du LST dans les zones urbaines, en particulier pour les mesures TIR par satellite à haute résolution spatiale, mais n'ont pas encore été bien pris en compte dans les algorithmes de récupération du LST existants: (1) l'effet d'adjacence dans la région spectrale TIR; (2) l'impact des structures tridimensionnelles (3-D) et de leur rayonnement sur les mesures TIR; (3) la dépendance des algorithmes de récupération de LST existants de la connaissance préalable précise de l'atmosphère et/ou de l'émissivité de la surface de la Terre. Cette thèse est consacrée au développement d'une méthode améliorée de récupération du LST pour les mesures TIR par satellite à haute résolution spatiale des zones urbaines en tenant compte de ces trois facteurs. Premièrement, le modèle de transfert radiatif à effet d'adjacence (FAERTM) a été développé pour fournir un outil utile pour corriger l'effet d'adjacence; Ensuite, le modèle analytique de transfert radiatif TIR sur les zones urbaines (ATIMOU) a été déduit pour corriger l'impact des structures 3-D et de leur rayonnement. Ensuite, la méthode de récupération du LST sans connaissance préalable (PKF) a été développée pour se débarrasser de la dépendance à l'égard de paramètres atmosphériques précis et/ou de l'émissivité de la surface de la Terre pendant la récupération du LST. Enfin, l'exploration préliminaire sur le développement d'une méthode améliorée de récupération du LST pour les mesures TIR par satellite à haute résolution spatiale des zones urbaines a été donnée. Les résultats montrent que la LST urbain pourrait être récupéré avec un RMSE de 3,33 K si la méthode PKF a été appliquée directement aux mesures TOA urbaines. Lors de la mise en œuvre de la méthode améliorée de récupération du LST, la RMSE de récupération du LST urbain diminue à 1,06 K, indiquant les bonnes performances de la méthode améliorée de récupération du LST pour les mesures TIR à haute résolution spatiale des zones urbaines, dans lesquelles les trois facteurs mentionnés influençant la précision de la récupération du LST dans les zones urbaines ont été traitées respectivement par la méthode proposée - FAERTM, ATIMOU et PKF LST.

Mots-clés: LST, TIR, transfert radiatif, effet d'adjacence, tridimensionnel

List of abbreviations

LST	Land surface temperature
LSE	Land surface emissivity
TIR	Thermal infrared
MW	Microwave
3-D	Three-dimensional
IFOV	Instantaneous field of view
FAERTM	Forward adjacency effect radiative transfer model
ATIMOU	Analytical thermal infrared radiative transfer model over urban areas
PKF	Prior-knowledge-free
MODTRAN	MODerate resolution atmospheric TRANsmission code
VIS-NIR	Visible and near infrared
PSF	Point spread function
ASPF	Aerosol scattering phase function
SRF	Spectral response function
DART	Discrete anisotropic radiative transfer mode
FWHM	Full width at half maximum
TIGR	Thermodynamic Initial Guess Retrieval
RMSE	Root-mean-square error
MMD	Maximum-minimum emissivity difference
NEΔT	Noise-equivalent differential temperature
SW	Split window
TES	Temperature/Emissivity separation
TOA	Top of atmosphere
BOA	Bottom of atmosphere

Contents

List of Figures

List of Tables

1 | **Introduction**

1.1. Background

Land surface temperature (LST) is one of the most important Earth System Data, which could influence the ecosystems at both regional and global scales (Hulley et al., 2019; King, 1999; Merchant et al., 2013). All the Earth surface processes relating to the energy and hydrology balance could be parameterized by the LST directly or indirectly (Jackson et al., 1985; Jackson et al., 1977; Running et al., 1994; Sellers et al., 1988; Vining and Blad, 1992). Thus, it is required in a variety of the researches including the monitoring of the urban environment (Anderson et al., 2008; Karnieli et al., 2010; Kustas and Anderson, 2009; Li et al., 2013a; Zhang et al., 2008). As we all know, cities always act as the center of a certain region in many spheres such as the population, administration, transportation, economy, education, culture, et. al, that are crucial for human civilizations (Gu et al., 2012; Guo et al., 2019). According to the Population Reference Bureau in 2019, more than half of the populations in the world live in the urban areas and the number is still rising (Bureau, 2019). Therefore, it is very important to study the urban environment in detail, which requires the accurate urban LST as one of the most essential input parameters (Jiang et al., 2018; Lau et al., 2016; Oltra-Carrio et al., 2014; Voogt and Oke, 1997).

Benefiting from remote sensing technology, the regional and global LSTs nowadays could be efficiently retrieved from the thermal infrared (TIR) and microwave (MW) measurements of the Earth surface (Duan et al., 2017; Martins et al., 2019; Zhang et al., 2019). However, the MW measurements generally have low spatial resolution and are very sensitive to soil moisture and surface roughness. Besides, they yield the "sub-surface temperature" instead of the "skin temperature" provided by TIR remote sensing. The TIR observations are consequently more suitable for obtaining high accuracy LSTs (Cook et al., 2014; Freitas et al., 2013; Malakar et al., 2018; Spacesystems and Team, 2001a; Wan, 2014; Wan et al., 2015a).

After decades of development, a wide variety of LST retrieval algorithms have been developed for different kinds of TIR sensors, on the basis of which, most of the current

LST products have been generated (Li et al., 2013a; Sattari and Hashim, 2014). It can be concluded that, for most circumstances regarding to natural flat surfaces and moderate/low spatial resolution TIR images, the LST could be retrieved within the accuracy of 1.0 K using the existing LST retrieval algorithms. However, these algorithms still have their limitations especially regarding to the accurate urban LST retrieval from high spatial resolution satellite TIR measurements.

First, the regardless of the adjacency effect in the TIR spectral region.

In fact, the adjacency effect has been confirmed to be significant in the visible and near infrared spectral region and has already been well studied (Duan et al., 2015; Sanders et al., 2001; Tanre et al., 1981; Vermote et al., 1997). It is shown that the strength of the adjacency effect generally decreases with increasing wavelength (Reinersman and Carder, 1995; Sanders et al., 2001) and decreasing image spatial resolution (Duan et al., 2015; Kaufman, 1982; Kaufman et al., 1994). Therefore, the adjacency effect has always been neglected with commonly used TIR images since they have relatively long observation wavelengths and coarse spatial resolutions. However, with continued development of remote sensing technology, high spatial resolution TIR images are attainable nowadays and the spatial resolution could increase further. Consequently, the adjacency effect could also increase significantly (Zheng et al., 2019b). But the adjacency effect in the TIR domain still does not attract enough attention and few studies focus on this topic (Duan et al., 2020). The regardless of the adjacency effect may result in additional biases in the retrieved LSTs. Thus, there is a need to quantitatively discuss the magnitude of the adjacency effect on such high spatial resolution TIR images, and to make an effort to take the adjacency effect into account in the retrieval of accurate LSTs.

Second, the impact of the three-dimensional (3-D) structures and their radiation on the TIR measurements.

When referring to the urban areas, the 3-D structures of the Earth surface would make the TIR radiative transfer processes more complex comparing with that of flat Earth surface (Oke, 1987; Qu, 2011). First of all, a certain amount of energy would be trapped inside the 3-D structures due to the multiple reflections, which could introduce additional radiations to the satellite TIR measurements (Fontanilles et al., 2010; Fontanilles et al., 2008). Additionally, during daytime of a cloudless day, the obstructions of solar irradiance inevitably exist in urban areas leading to the temperatures of sunlit and shadowed areas significantly different, which aggravate the thermal heterogeneity of the urban areas

(Fontanilles et al., 2008; Gastellu-Etchegorry et al., 2015). Moreover, as the viewing angle changes, the compositions inside the sensor's IFOV may be different resulting from the occlusions between the 3-D manmade constructions, leading to the anisotropic satellite observed signals through various viewing angles (Baghdadi and Zribi, 2016; Jiang et al., 2018). All these could have nonnegligible impact on the satellite observed radiance but have not been considered into the existing LST retrieval algorithms yet. Therefore, the quantitative relationships between the parameters of urban street canyons and their corresponding impact on the TIR measurements need to be well studied and addressed to improve the LST retrieval accuracy in urban areas.

Third, the dependence of the existing LST retrieval algorithms on the accurate prior knowledge of the atmosphere and/or the Earth surface emissivity.

Although many excellent LST retrieval algorithms have already been proposed, they all require accurate prior knowledge (atmospheric parameters and/or emissivity of the Earth surface) to retrieve LST from satellite TIR measurements (Zheng et al., 2019a). That being said, the performances of the existing LST retrieval algorithms have been greatly dependent on the accuracy of the prior knowledge (Li et al., 2013a; Sattari and Hashim, 2014). However, such prior knowledge is not always obtainable in actual applications at pixel scale (Ren et al., 2020). Consequently, the LST retrieval accuracy may be unable to meet the requirement of better than 1.0 K as required by many other disciplines under certain circumstances (Sobrino et al., 2016). Improvements on existing LST retrieval algorithms or new LST retrieval methods are demanded to retrieve accurate LST from satellite TIR measurements directly without dependence on any prior knowledge.

1.2. Objectives and structures of this thesis

This thesis is dedicated to the investigation of the factors influencing the satellite TIR measurements and the LST retrieval accuracy, the final purpose of which is to develop an improved LST retrieval method for high spatial resolution satellite TIR measurements of urban areas.

Specifically, four research objectives have been involved in this thesis as below:

(1) To quantitively investigate the adjacency effect in the TIR spectral region under different atmospheric and imaging conditions.

(2) To quantitively investigate the impact of the 3-D structures and their radiation on the

TIR measurements.

(3) To explore some new methods which could be used to retrieve accurate LST from satellite TIR measurements directly without dependence on the prior knowledge.

(4) To make a primary exploration on developing an improved LST retrieval method for high spatial resolution satellite TIR measurements of urban areas on the basis of the researches aiming at the first three objectives.

Additionally, the relationships between these four specific research objectives have been illustrated in the Fig. 1-1.
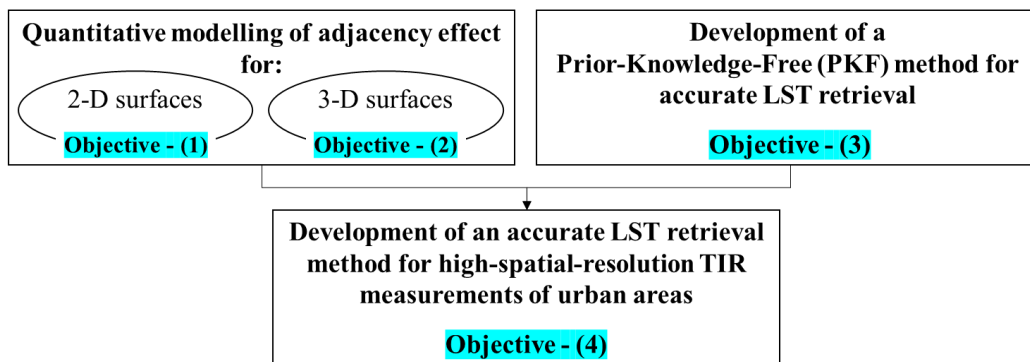
Fig. 1-1. Illustration of the relationships between the four specific research objectives of this thesis.

Following the research objectives, this thesis is organized into six chapters:

Chapter 1 gives a general introduction over the LST retrieval researches, including the analyses of the factors that may influence the LST retrieval accuracy from high spatial resolution satellite TIR measurements of urban areas, and the objectives and organizations of this thesis.

The following three chapters (chapter 2 aiming at the first objective, chapter 3 aiming at the second objective, and chapter 4 aiming at the third objective) are based on three published articles during my doctoral study.

Chapter 2 presents the forward adjacency effect radiative transfer model (FAERTM), on the basis of which, the adjacency effect under different atmospheric and imaging conditions for flat surfaces has been well studied. From another aspect, this chapter provides a useful tool to address the adjacency effect from the satellite TIR measurements. (*Based on X. Zheng, Z.-L. Li, X. Zhang, and G. Shang, "Quantification of the adjacency effect on measurements in the thermal infrared region," IEEE Transactions on Geoscience and Remote Sensing, vol. 57, no. 12, pp. 9674-9687, Jul. 2019.*)

Chapter 3 presents the analytical thermal infrared radiative transfer model over urban areas (ATIMOU), which provides quantitative relationships between the parameters of urban street canyons and their corresponding impact on the TIR measurements. That is, a method which could be used to correct the impact of the 3-D structures and their radiation on the TIR measurements has been proposed in this chapter. (*Based on X. Zheng, M. Gao, Z.-L. Li, K.-S. Chen, X. Zhang, and G. Shang, "Impact of 3-d structures and their radiation on thermal infrared measurements in urban areas," IEEE Transactions on Geoscience and Remote Sensing, vol. Early Access, no. Early Access, pp. 1-15, May 2020.*)

Chapter 4 develops a new LST retrieval method, which could be used to retrieve the accurate LST from satellite TIR measurements directly without dependence on the prior knowledge of atmospheric parameters and the Earth surface emissivities. (*Based on X. Zheng, Z.-L. Li, F. Nerry, and X. Zhang, "A new thermal infrared channel configuration for accurate land surface temperature retrieval from satellite data," Remote Sensing of Environment, vol. 231, no. (2019) 111216, pp. 1-12, May 2019.*)

Chapter 5 covers a preliminary exploration on developing an improved LST retrieval method for high spatial resolution satellite TIR measurements of urban areas on the basis of the researches in chapter 2, chapter 3, and chapter 4.

Chapter 6 summarizes the conclusions and perspectives.

2 | Quantification of the adjacency effect on measurements in the TIR region

Sensor-observed energy from adjacent pixels, known as the adjacency effect, influences land surface reflectivity retrieval accuracy in optical remote sensing. As the spatial resolution of thermal infrared (TIR) images increases, the adjacency effect may influence land surface temperature (LST) retrieval accuracy in TIR remote sensing. However, to my knowledge, few studies have focused on quantifying this adjacency effect on TIR measurements. In this chapter, a forward adjacency effect radiative transfer model (FAERTM) was developed to quantify the adjacency effect on high spatial resolution TIR measurements. The model was verified to be in good agreement with moderate resolution atmospheric transmission (MODTRAN) code, with a discrepancy < 0.15 K. The adjacency effect on target pixel observations was found to be negligible beyond 3 km from the line of sight. Variations in aerosol type only slightly influenced adjacency effect magnitude. However, the adjacency effect quickly increased with increasing image spatial resolution, adjacent pixel temperature, and aerosol density. According to simulation results, the adjacency effect can be > 3 K in some cases. These findings indicate that the adjacency effect should be considered when retrieving LSTs from TIR measurements, at least in some specific conditions. The proposed FAERTM provides a useful model for quantifying and addressing the adjacency effect on TIR measurements.

2.1. Introduction

Land surface temperature (LST) is an important input parameter for many domains, including evapotranspiration, vegetation monitoring, and global climate change (Anderson et al., 2008; Karnieli et al., 2010; Kustas and Anderson, 2009; Li et al., 2013a; Zhang et al., 2008). Remote sensing provides an efficient method for obtaining regional and global LST images. LSTs are generally retrieved using microwave (MW) and thermal infrared (TIR) spectral measurements. However, even though MWs can penetrate through clouds, MW measurements have low spatial resolution (Liu et al., 2013). Furthermore, these yield the "sub-surface temperature" instead of the "skin temperature" provided by TIR remote sensing, and MW measurements are also sensitive to soil moisture and surface roughness (Duan et al., 2017; Wen et al., 2003). TIR observations are consequently more suitable for obtaining LSTs. A wide variety of LST retrieval algorithms have been developed over several decades (Li et al., 2013a; Sattari and Hashim, 2014); these can be roughly classified into four categories: single-channel methods (Jimenez-Munoz and Sobrino, 2003; Ottle and Vidal-Madjar, 1992; Qin et al., 2001b), multi-channel methods (such as the split window (SW) method (Becker and Li, 1990; Coll and Caselles, 1997; McMillin, 1975; Qin et al., 2001a; Sobrino et al., 1996; Wan and Dozier, 1996) and temperature emissivity separation (TES) method (Gillespie et al., 1998)), dual-angle methods (Chedin et al., 1982), and day/night methods (Wan and Li, 1997; Watson, 1992). All of these methods have been designed to remove atmospheric and land surface emissivity (LSE) effects and perform well for current TIR images (Becker, 1987; Becker and Li, 1995; Li and Becker, 1993; Li et al., 2013b). However, to our knowledge, the adjacency effect has not been considered during the derivation of these LST retrieval methods.

The adjacency effect is defined as sensor-observed energy reflected or emitted from adjacent pixels (Burazerovic et al., 2013; Richter et al., 2006). Its influence has already been well addressed in the visible and near infrared (VIS-NIR) spectral region (Duan et al., 2015; Sanders et al., 2001; Tanre et al., 1981; Vermote et al., 1997). Existing methods for addressing the adjacency effect in this region are based either on empirical relations to avoid time-consuming operations, which is practical for operational purposes (Ouaidrari and Vermote, 1999; Richter, 1990, 1998; Tanre et al., 1987; Tanre et al., 1981; Thome et al., 1998), or on the atmospheric point spread function (PSF), which has a specific physical meaning but requires detailed atmospheric parameters (Kaufman, 1984; Otterman and Fraser, 1979; Pearce, 1986; Reinersman and Carder, 1995; Sanders et al., 2001; Semenov

et al., 2011; Yang et al., 2009). The strength of the adjacency effect has been shown to generally decrease with increasing wavelength (Reinersman and Carder, 1995; Sanders et al., 2001) because the scattering intensity of atmospheric particles is inversely dependent on wavelength (Ångström, 1929; Eck et al., 1999; Kaskaoutis and Kambezidis, 2006; Reinersman and Carder, 1995; Sanders et al., 2001). Besides, according to previous studies (Duan et al., 2015; Kaufman, 1982; Kaufman et al., 1994), the adjacency effect is usually not significant in low-spatial-resolution images. Therefore, the adjacency effect has generally been neglected with current TIR images, since they have long observation wavelengths and coarse spatial resolutions. However, with continued development of remote sensing technology, high spatial resolution TIR images can now be acquired, and there is therefore a need to quantitatively discuss the magnitude of the adjacency effect on such high spatial resolution TIR images.

The objective of this chapter is to develop a forward adjacency effect radiative transfer model (FAERTM) in order to quantify the adjacency effect for different atmospheric and imaging conditions, especially for high spatial resolution TIR measurements.

This chapter is organized as follows. Section 2.2 describes the development of the forward adjacency effect radiative transfer model. Section 2.3 describes the input parameters for experiments. Section 2.4 compares the proposed model with moderate resolution atmospheric transmission (MODTRAN) code. Section 2.5 analyzes the adjacency effect for different atmospheric and imaging conditions. Finally, section 2.6 summarizes the main findings.

2.2. Development of the forward adjacency effect radiative transfer model

In MODTRAN, the adjacency effect can only be simulated if image spatial resolution is ignored. To quantitatively study the adjacency effect for various atmospheres and image spatial resolutions, the FAERTM is therefore developed.

2.2.1. Radiative transfer equation of FAERTM

For simplification purposes, the following three assumptions were adopted. First, the land surface is flat, without rugged terrain and buildings. Second, observations are acquired vertically, which is usually true for high spatial resolution images. Third, the proportion of energy that has been scattered more than twice is insignificant. With these assumptions,

adjacent pixels can only affect observed target radiance through atmospheric scattering. Bearing in mind that the energy source in the TIR region is thermal radiation (rather than sunlight), the total spectral radiance (L_λ) received by the remote sensor can be divided into five components (Fig. 2-1). The radiative transfer equation of FAERTM can thus be expressed as follows:

$$L_\lambda = B_\lambda\left(T_{b\lambda}\right) = \tau_\lambda \varepsilon_\lambda B_\lambda\left(T_s\right) + \tau_\lambda\left(1-\varepsilon_\lambda\right)L_{\downarrow\lambda} + L_{\uparrow\lambda} + L_{1\lambda} + \tau_\lambda\left(1-\varepsilon_\lambda\right)\frac{L_{2\lambda}}{1-\rho_\lambda S_\lambda} \qquad \text{Eq. 2-1}$$

where λ is the wavelength and B_λ is the Planck function. Here, $T_{b\lambda}$ is equivalent channel brightness temperature considering the adjacency effect, τ_λ is direct atmospheric transmittance, ε_λ and T_s are LSE and LST, $L_{\downarrow\lambda}$ and $L_{\uparrow\lambda}$ are atmospheric downwelling and upwelling radiance respectively, ρ_λ is land surface reflectance, and S_λ is atmospheric spherical albedo at the bottom of the atmosphere. The last two items on the right-hand side of Eq. 2-1 describe the adjacency effect: $L_{1\lambda}$ is the single scattered adjacent pixel radiance (Fig. 2-1d) and $L_{2\lambda}$ is the adjacent pixel radiance that has been reflected by the atmosphere (Fig. 2-1e), with $(1-\rho_\lambda S_\lambda)$ representing illumination enhancement due to the trapping mechanism. The critical problem of FAERTM is then to model L_1, and L_2:

$$L = B\left(T_b\right) = \tau\varepsilon B\left(T_s\right) + \tau\left(1-\varepsilon\right)(L_\downarrow + \frac{L_2}{1-\rho S}) + L_\uparrow + L_1 \qquad \text{Eq. 2-2}$$

with the subscript λ omitted for simplicity.
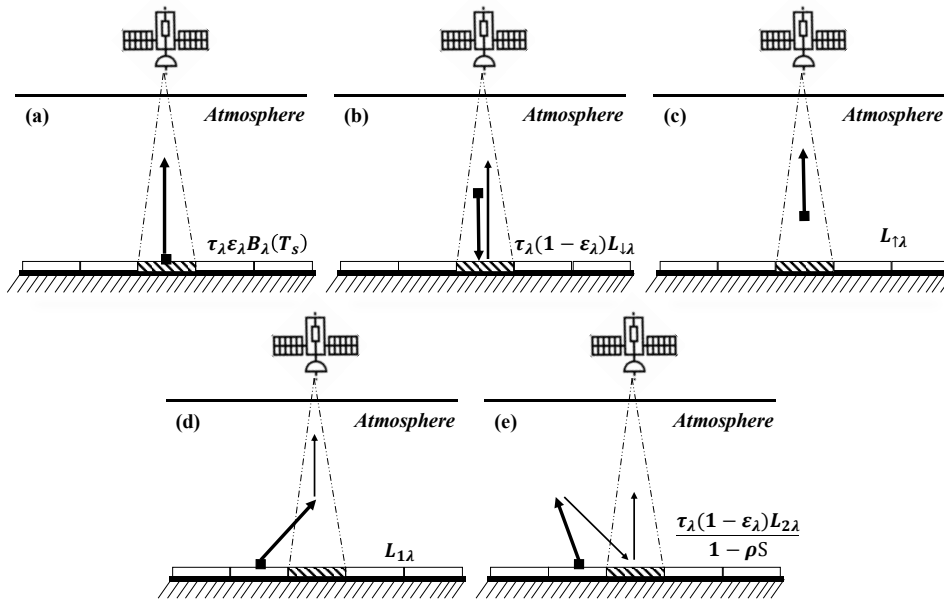
Fig. 2-1. Radiation sources of at-sensor observations. The surface patches with and without shading represent target and adjacent pixels, respectively. Solid cubes indicate emission sources. The five sources include (a) target-emitted radiance; (b) target-reflected atmospheric downwelling radiance; (c) atmospheric upwelling radiance; (d) single scattered adjacent pixel radiance; and (e) adjacent pixel radiance that has been reflected by the atmosphere and then reflected by the target pixel.

2.2.2. Single scattered adjacent pixel radiance (L_1)

We assume an adjacent pixel $A_{i,j}$ with LST and LSE of $T_{i,j}$ and $\varepsilon_{i,j}$, respectively (Fig. 2-2). The emitted radiance of this adjacent pixel ($R_{i,j}$) can be given by:

$$R_{i,j} = \varepsilon_{i,j}B(T_{i,j}) + (1 - \varepsilon_{i,j})L_{\downarrow} \qquad \text{Eq. 2-3}$$

where $L_{\downarrow}$ is atmospheric downwelling radiance. Based on the radiative transfer theory, the radiance ($R1_{i,j}$) that arrives at an infinite thin atmosphere (C_h) at height h in the instantaneous field-of-view (IFOV) can be expressed by:

$$R1_{i,j} = R_{i,j}e^{-t\left(\left|\overrightarrow{A_{i,j}C_h}\right|\right)} \qquad \text{Eq. 2-4}$$

where $t(|\overrightarrow{A_{i,j}C_h}|)$ is the optical depth of the atmosphere between $A_{i,j}$ and C_h.

Let dt_h^{sca} be the atmospheric scattering optical depth of the infinite thin atmosphere C_h. The scattered radiance ($R1_{i,j}^{sca}$) when light passes through dt_h^{sca} is given by:

$$R1_{i,j}^{sca} = R1_{i,j}dt_h^{sca} \qquad \text{Eq. 2-5}$$

The fraction ($\psi 1$) of scattered energy that is scattered into the sensor direction can be calculated by introducing the scattering phase function (P), which is related to the wavelength and scattering angle. Assuming that the area of $A_{i,j}$ and the sensor are both small, according to the reciprocity theorem, the fraction of scattered energy is the same when source and receiver are exchanged (Jarosz, 2008). If the sensor is considered as the radiation source, $\psi 1$ therefore equals the fraction of scattered energy that is scattered into $A_{i,j}$ (Kneisys et al., 1996):

$$\psi 1 = P(\lambda, \theta)\Omega_{A_{i,j} \rightarrow C_h} \qquad \text{Eq. 2-6}$$

Here, $\theta = \arccos\left(\frac{\overrightarrow{C_hA_{i,j}}\cdot\overrightarrow{C_hT}}{|\overrightarrow{C_hA_{i,j}}||\overrightarrow{C_hT}|}\right)$ is the angle between the vector $\overrightarrow{C_hA_{i,j}}$ and $\overrightarrow{C_hT}$ in Fig. 2-2. The letter T represents the position of the target pixel and $\Omega_{A_{i,j} \rightarrow C_h}$ is the solid angle that the adjacent pixel $A_{i,j}$ expands to the scattering point C_h. Both $\Omega_{A_{i,j} \rightarrow C_h}$ and θ are related to imaging spatial resolution.

If the size of $A_{i,j}$ fails to meet the small area assumption of the reciprocity theorem, it can be divided into several small patches; $\psi 1$ of each patch can then be calculated. The sum of the fractions for each small patch describes $\psi 1$ for $A_{i,j}$.

Assuming the atmospheric optical depth between C_h and sensor O is $t(|\overrightarrow{C_h O}|)$, the proportion of $A_{i,j}$ emitted radiance ($R1_{i,j}^{sensor}$) that can be observed by the sensor is given by:

$$R1_{i,j}^{sensor} = R1_{i,j}^{sca} \psi 1 e^{-t\left(\left|\overrightarrow{C_h O}\right|\right)}$$

Eq. 2-7

Substituting Eq. 2-4 ~ Eq. 2-6 into Eq. 2-7, we get:

$$R1_{i,j}^{sensor} = R_{i,j} e^{-t\left(\left|\overrightarrow{A_{i,j} C_h}\right|\right)} e^{-t\left(\left|\overrightarrow{C_h O}\right|\right)} P(\lambda,\theta) \Omega_{A_{i,j} \to C_h} dt_h^{sca}$$

Eq. 2-8
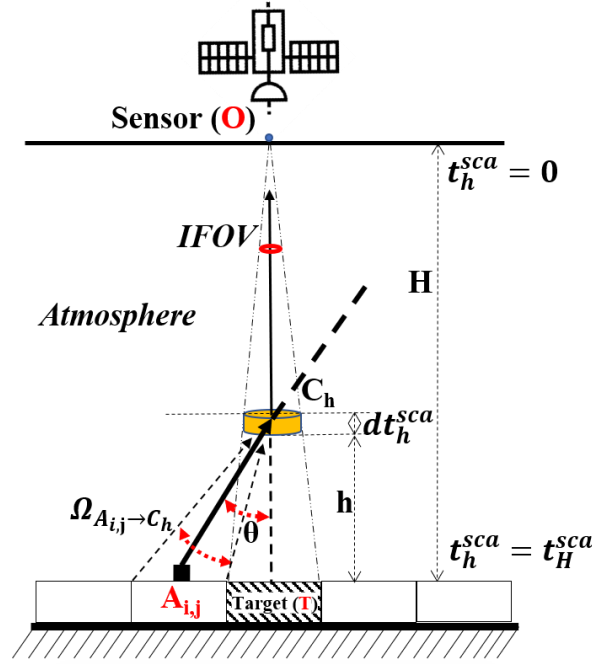
Fig. 2-2. Illustration of single scattered adjacent pixel radiance (L_1).

When integrating $R1_{i,j}^{sensor}$ vertically through the whole IFOV, the contribution of $A_{i,j}$ to the final observed radiance ($L_{i,j}^1$) can be expressed by:

$$L_{i,j}^1 = \int_{t_H^{sca}}^{0} R_{i,j} e^{-t\left(\left|\overrightarrow{A_{i,j} C_h}\right|\right)} e^{-t\left(\left|\overrightarrow{C_h O}\right|\right)} P(\lambda,\theta) \Omega_{A_{i,j} \to C_h} dt_h^{sca}$$

Eq. 2-9

After integrating $L_{i,j}^1$ over all adjacent pixels, the single scattered adjacent pixel radiance (L_1) can be given by:

$$L_1 = \int_{-\infty}^{+\infty} \int_{-\infty}^{+\infty} L_{i,j}^1 \, di \, dj$$

Eq. 2-10

where subscripts i, j represent the position of the adjacent pixels.

2.2.3. Target-reflected adjacent pixel radiance (RAD)

While the target pixel reflects atmospheric downwelling irradiance upward, the atmosphere can also reflect ground upwelling radiance downward, i.e., back to the ground (Fig. 2-3). This atmosphere-reflected downward radiance can be reflected by the target pixel into the sensor, contributing to the adjacency effect.

Assuming that land surface temperature and emissivity for background pixels are T_{bck} and ε_{bck} respectively, the radiance (L_2) emitted from the ground and reflected by the atmosphere can be given by:

$$L_2 = \varepsilon_{bck} B\left(T_{bck}\right) S \qquad \text{Eq. 2-11}$$

where S is the atmospheric spherical albedo at the bottom of the atmosphere. Considering the trapping mechanism between land surface and atmosphere, an illumination enhancement factor, which is actually the sum of a geometric sequence, is introduced to compensate for atmosphere-reflected ground radiance:

$$\frac{L_2}{1\text{-}\rho S} = \frac{\varepsilon_{bck} B\left(T_{bck}\right) S}{1\text{-}\rho S} \qquad \text{Eq. 2-12}$$

here, $\rho = 1 - \varepsilon_{bck}$, representing land surface reflectance.

If the land surface is heterogeneous, T_{bck} and ε_{bck} should refer to averaged land surface temperature and emissivity, which can be estimated by introducing the PSF as the ground weighting function. Assuming $g_{i,j}$ is the PSF, or the ground weighting function for a given atmosphere, then T_{bck} and ε_{bck} can be given by:

$$\varepsilon_{\text{bck}} = \int\limits_{-\infty}^{+\infty}\int\limits_{-\infty}^{+\infty} \varepsilon_{i,j} g_{i,j}\, di dj \qquad \text{Eq. 2-13}$$

$$T_{bck} = B^{-1}\left(\frac{\int\limits_{-\infty}^{+\infty}\int\limits_{-\infty}^{+\infty} \varepsilon_{i,j} B(T_{i,j}) g_{i,j}\, di dj}{\varepsilon_{bck}}\right) \qquad \text{Eq. 2-14}$$

where subscripts i, j represent the position of the land surface pixels. B^{-1} is the inverse of the Planck function.

In order to obtain $g_{i,j}$, Eq. 2-9 in Section 2.2.2 was reconsidered. From Eq. 2-9, it can be easily shown that the unnormalized value of $g_{i,j}$ ($g_{i,j}^{unnormal}$) is defined as:

$$g_{i,j}^{unnormal} = \int_{t_H^{sca}}^{0} e^{-t\left(\left|\overline{A_{i,j}C_h}\right|\right)} e^{-t\left(\left|\overline{C_hO}\right|\right)} P(\lambda,\theta)\Omega_{A_{i,j}\to C_h} dt_h^{sca} \qquad \text{Eq. 2-15}$$

After normalization of $g_{i,j}^{unnormal}$, $g_{i,j}$ can be given by:

$$g_{i,j} = \frac{g_{i,j}^{unnormal}}{\int_{-\infty-\infty}^{+\infty+\infty} g_{i,j}^{unnormal} \, didj} \qquad \text{Eq. 2-16}$$

Finally, by combining Eq. 2-12 ~ Eq. 2-16, the target-reflected adjacent pixel radiance (*RAD*) can be acquired by:

$$RAD = \tau(1-\varepsilon)\frac{L_2}{1-\rho S} = \tau(1-\varepsilon)\frac{\varepsilon_{bck}B(T_{bck})S}{1-(1-\varepsilon_{bck})S} \qquad \text{Eq. 2-17}$$

where τ is direct atmosphere transmittance and ε is target pixel emissivity. When the land surface is homogenous, ε_{bck} should be the same as ε.
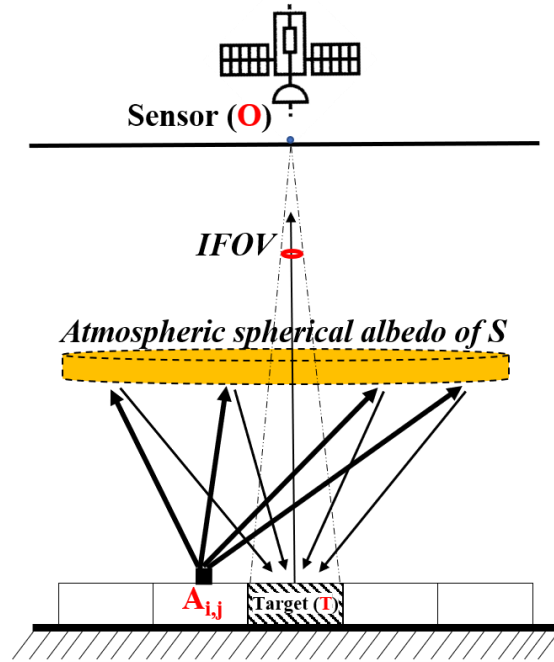
Fig. 2-3. Illustration of target-reflected adjacent pixel radiance.

2.2.4. Radiance contributed by target pixel and atmosphere

The first three terms on the right-hand side of Eq. 2-2 (Fig. 1-1(a)–(c)) can be calculated after acquiring τ, $L_\downarrow$, and $L_\uparrow$. In this study, MODTRAN was used to calculate these

parameters for different atmospheric conditions. Since the single scattered adjacent pixel radiance (L_1) and the target-reflected adjacent pixel radiance (RAD) were considered separately in FAERTM (see Eq. 2-2), the $L_\downarrow$ and $L_\uparrow$ should be the intrinsic atmospheric radiance which is actually the atmospheric radiance neglecting the scattered radiation from ground. However, the MODTRAN output path thermal radiance (related to $L_\uparrow$) and ground reflected radiance (related to $L_\downarrow$) would contain the contribution of land surface radiation if the land surface temperature was left as default in MODTRAN. Therefore, in order to exclude the influence of land surface radiation on intrinsic atmospheric quantities, in this study, $L_\uparrow$ and $L_\downarrow$ were calculated using MODTRAN by setting $\varepsilon = 1.0$, $T_s =$ 0.00001 K and $\varepsilon = 0.0$, $T_s =$ 0.00001 K, respectively.

2.2.5. Quantification of adjacency effect on satellite TIR measurements

If the adjacency effect terms [L_1, $\tau(1-\varepsilon)\frac{L_2}{1-\rho S}$] are omitted from Eq. 2-2, FAERTM can be reduced to the traditional thermal infrared radiative transfer equation (Becker and Li, 1990; Wan and Dozier, 1996; Wan and Li, 1997):

$$L = B\left(T_b^0\right) = \tau \varepsilon B\left(T_s\right) + \tau\left(1-\varepsilon\right)L_\downarrow + L_\uparrow \qquad \text{Eq. 2-18}$$

where T_b^0 is the equivalent channel brightness temperature of the satellite TIR measurement, without considering adjacency effect. In fact, Eq. 2-18 is the basic function, based on which commonly-used LST retrieval algorithms were developed. However, because the temperature and emissivity of adjacent pixels are always not equal to zero, the scattered adjacent pixels' radiation will also contribute to observed target pixel radiance. When using existing LST retrieval algorithms, target pixel temperature retrieval accuracy can therefore be affected, even if adjacent pixels have the same temperature and emissivity as the target pixel. The adjacency effect (here defined as observed target radiation difference between a case with adjacent pixels' radiation and one without) therefore merits further research. In order to intuitively represent the adjacency effect, the difference (ΔT_b) between T_b and T_b^0 will be used in the following sections:

$$\Delta T_b = T_b - T_b^0 \qquad \text{Eq. 2-19}$$

Additionally, land surface has always been assumed to be homogenous in practical applications. Under such circumstance, a simplified radiative transfer equation using the total transmittance (direct plus diffuse) was presented in the previous study (Adler-Golden et al., 2014). In the radiative transfer equation Eq. 2-18, if the total transmittance is also

used rather than the direct one, the diffuse transmittance will provide the adjacency radiance from background. Consequently, the adjacency effect arises only from target-background contrast. In this study, instead of simply replacing the direct transmittance with total transmittance in Eq. 2-18, a more detailed equation Eq. 2-20 was provided to calculate the satellite-observed radiance of homogenous surfaces, as expressed by:

$$L = B\left(T_b^1\right) = \tau\varepsilon B\left(T_s\right) + \tau\left(1-\varepsilon\right)(L_\downarrow + \frac{L_2^{hom}}{1-\rho S}) + L_\uparrow + L_1^{hom} \qquad \text{Eq. 2-20}$$

where L_1^{hom} and L_2^{hom} have the same meanings as in Eq. 2-2 but are calculated under the assumption that adjacent pixels have the same temperature and emissivity as the target pixel. The adjacency effect, now defined as observed target radiation difference between a case with target-to-background-radiation-contrast and one without, should thus be explored. Therefore, the difference (δT_b) between T_b and T_b^1 was also investigated in this study:

$$\delta T_b = T_b - T_b^1 \qquad \text{Eq. 2-21}$$

2.3. Simulation description

2.3.1. Scenario input simulation parameters

As shown in Section 2.2, in addition to direct atmospheric transmittance, atmospheric downwelling, and upwelling radiance, which can be obtained from MODTRAN (Kneisys et al., 1996), FAERTM also requires the temperature and emissivity of the target and adjacent pixels, scattering phase function, scattering optical depth, and atmospheric spherical albedo at the bottom of the atmosphere to calculate the adjacency effect. Different simulation input combinations were selected to provide a variety of atmospheric and imaging scenarios. According to previous studies, in the TIR region, scattering is mainly caused by aerosol particles for flat surfaces, and the adjacency effect in TIR spectral region therefore depends mainly on aerosol (Ångström, 1929; Cimini et al., 2010; Reinersman and Carder, 1995). In this study, two typical aerosol types and four visibilities were used as simulation inputs. The required direct atmospheric transmittance and atmospheric downwelling and upwelling radiance were calculated using the 1976 U.S. Standard atmosphere profiles as an example, because the adjacency effect performs similarly for other atmospheric types provided input aerosol parameters remain unchanged. In terms of imaging conditions, the adjacency effect was studied with varying wavelengths, image spatial resolutions, and temperatures and emissivities of target and adjacent pixels. Five

pre-set ranges were given to study the spatial extent of the adjacency effect. Moreover, the remote sensor was placed on a satellite platform at an altitude of 705 km. The detailed input simulation parameters are listed in Table 2-1.

Table 2-1. Scenario input simulation parameters

Atmospheric conditions	
Atmosphere model	1976 U.S. Standard
Aerosol model	RURAL, URBAN
Atmospheric visibility	5, 10, 23, 40 km
Imaging conditions	
Wavelength	8, 9, 10, 11, 12 μm
Image spatial resolution	0.005, 0.01, 0.03, 0.06, 0.1, 0.25, 0.5, 1.0 km
Temperature of target pixel (TAT_LST)	270, 290, 310 K
Temperature of adjacent pixels	From TAT_LST – 30 K to TAT_LST + 30 K with a step of 10 K
Emissivity of target pixel	0.90, 0.98
Emissivity of adjacent pixels	0.90, 0.98
Calculation range of adjacency effect	1.0, 2.0, 3.0, 4.0, 5.0 km
Sensor altitude	705 km

2.3.2. Scattering phase function of FAERTM

Another important input of FAERTM is the aerosol scattering phase function (ASPF), which determines the radiation intensity of a certain direction after scattering (Kaufman et al., 1994; Liou, 2002). The scattering property of normal aerosol particles was measured in a laboratory in 1983, at wavelengths ranging from 0.2 to 40 μm (Kneizys et al., 1983). Then, an ASPF database was built based on the Mie scattering theory and embedded in MODTRAN (Kneisys et al., 1996). The database was reported to approximate exact phase functions within about 20% (Kneisys et al., 1996). In this study, we used this ASPF database to calculate the adjacency effect. As shown in Fig. 2-4, most scattered energy is concentrated in the forward direction within a scattering angle < 60°, which means that distant adjacent pixels would make an insignificant contribution to the final adjacency effect.
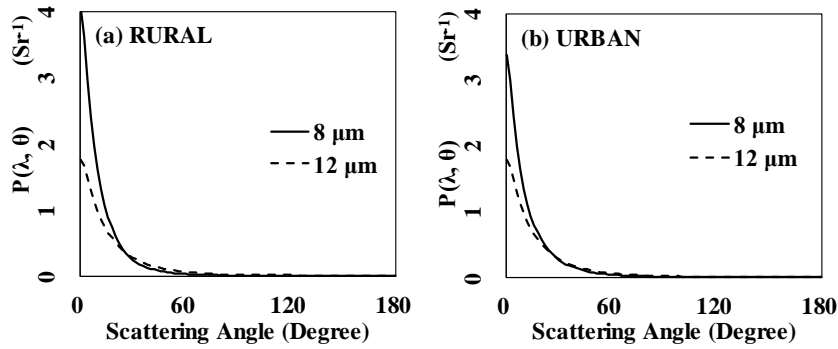
Fig. 2-4. Aerosol scattering phase function used in this study. Wavelengths of 8 and 12 μm were used as examples for two aerosol types: (a) RURAL and (b) URBAN.

2.3.3. Actual satellite data

In order to preliminarily investigate the adjacency effect in real satellite data, MODIS (Moderate Resolution Imaging Spectroradiometer) Land Surface Temperature and Emissivity (MOD11) (Wan et al., 2015a) data, with pixel size of 1000 m * 1000 m, were introduced to represent low spatial resolution data. ASTER (Advanced Spaceborne Thermal Emission and Reflectance Radiometer) Surface Kinetic Temperature (AST08) (Spacesystems and Team, 2001a) and Surface Emissivity (AST05) (Spacesystems and Team, 2001b) data, with pixel size of 90 m * 90 m, were used to represent high spatial resolution data. The study area was Zhangye, China (100°26'59" E, 38°55'33" N), where the main surface coverage types are the Gobi Desert and oases. The data used in this study were acquired on April 24, 2013 onboard the same platform TERRA (Fig. 2-5).
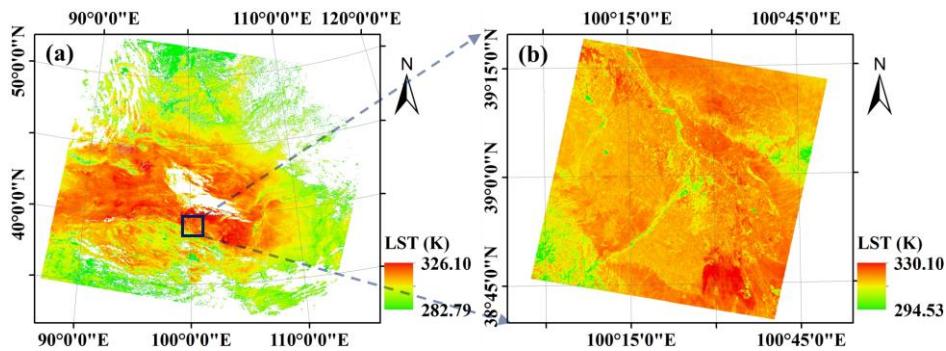
Fig. 2-5. LST images of the study area obtained from (a) MOD11 product of MODIS observations, and (b) AST08 product of ASTER observations.

2.4. Comparison between FAERTM and MODTRAN

In MODTRAN, the adjacency effect is modeled by setting the target pixel in a uniform background (Berk et al., 2008). The background is defined based on two parameters: "area-

averaged" temperature and "area-averaged" emissivity (Clough et al., 1992; Kneisys et al., 1996). These parameters are usually obtained by convoluting background LST and LSE with the atmospheric PSF. In this section, target and adjacent pixels were first assumed to be homogeneous. Our results are thus comparable with those from MODTRAN, without requiring calculation of the atmospheric PSF. Second, a scenario with two different surfaces was assumed, as can usually be found at the seashore. In this case, the land surface is heterogenous and the PSF is therefore needed, which can be estimated from Eq. 2-15 and Eq. 2-16.

2.4.1. For homogeneous land surfaces

In this case, adjacent pixels have the same LST and LSE as the target pixel. LSE was fixed at 0.9 while two LSTs (270 K, 310 K) were considered. The aerosol type was set as RURAL. Differences in simulated satellite brightness temperature between MODTRAN ($T_{MODTRAN}$) and FAERTM (T_{FAERTM}) were calculated (Fig. 2-6(a) and (b)). In addition, considering that the target-reflected adjacent pixel radiance (RAD) can be obtained in MODTRAN by comparing radiances reflected from a target pixel (LST=270 K, LST=310 K) and a non-emitted background (T_{bck}=0 K) with those from a homogeneous surface (T_{bck}=270K, T_{bck}=310 K), this portion of radiance calculated from FAERTM (RAD_{FAERTM}) was also separately compared with that from MODTRAN ($RAD_{MODTRAN}$) (Fig. 2-6 (c)).
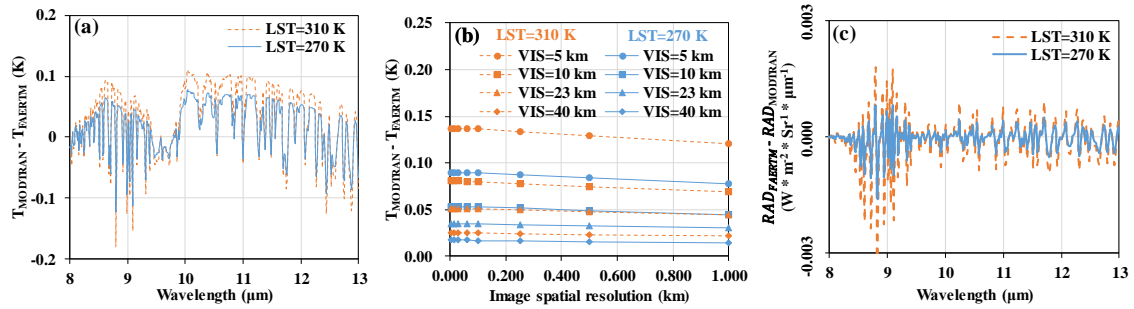
Fig. 2-6. Difference in satellite brightness temperature and target-reflected adjacent pixel radiance between MODTRAN and FAERTM simulations. LSE and aerosol type were fixed as 0.9 and RURAL, respectively. (a) Simulated satellite brightness temperature difference as a function of wavelength, with atmospheric visibility of 10 km and image spatial resolution of 0.03 km. (b) Simulated satellite brightness temperature difference for different atmospheric visibilities (VIS) and image spatial resolutions, with wavelength of 10 μm. (c) Difference in simulated target-reflected adjacent pixel radiance as a function of wavelength, with atmospheric visibility of 10 km.

As shown in Fig. 2-6(a) and (b), compared with MODTRAN, the proposed model slightly underestimated the adjacency effect for most of the spectral region. Since the difference in target-reflected adjacent pixel radiance between MODTRAN and FAERTM is small (Fig.

2-6(c)), the underestimation is likely caused by the neglect of multiple scattering in the L_1 calculation in this study; conversely, this is calculated in MODTRAN (Isaacs et al., 1987; Kneisys et al., 1996; Wang and Ryan, 1983; Wiscombe and Grams, 1976). Because more multiple scattering occurs in a turbid atmosphere than in a clear atmosphere, the difference between the proposed model and MODTRAN also increased as atmospheric visibility decreased (Fig. 2-6(b)). In addition, it is noticed that the discrepancies between the two models seem to follow the shape of the atmospheric transmissivity spectrum (Fig. 2-6(a)). The possible reason may be that the adjacency effect is in fact suppressed by atmospheric transmittance in both FAERTM and MODTRAN when considering satellite observations, because atmospheric optical depth was used to model the adjacency effect, as discussed in Sections 2.2.2 and Section 2.2.3. Therefore, smaller atmospheric transmittance would decrease the adjacency effect in both models, leading to a relatively smaller discrepancy between the two models in contrast to cases with larger atmospheric transmittances, and then making the discrepancies follows the shape of the atmospheric transmissivity spectrum along wavelength. But overall, even in extreme conditions, with atmospheric visibility of 5 km, LST of 310 K, and wavelength of 10 μm, the difference was no larger than 0.15 K with respect to an adjacency effect of 2.3 K calculated by MODTRAN. Therefore, the proposed model is accurate for capturing signal variation caused by the adjacency effect.

2.4.2. For heterogeneous land surfaces

In this case, a scenario with two different surfaces was considered, with the left part having emissivity of 0.9 and the right part having emissivity of 0.98 (Fig. 2-7). The temperature of the right part was fixed at 290 K while the temperature of the left part varied from 270 K to 310 K, with a step of 20 K. The target is located on the left border of the right part, with a pixel size of 0.03 * 0.03 km. Atmospheric visibility was set at 10 km and aerosol type was set as RURAL. The PSF required in this case was estimated from Eq. 2-15 and Eq. 2-16 given in Section 2.2.3. By inputting the scenario parameters, the difference in simulated satellite brightness temperature between MODTRAN ($T_{MODTRAN}$) and FAERTM (T_{FAERTM}) was calculated. The results at 10.0 μm were given as an example (Fig. 2-8).
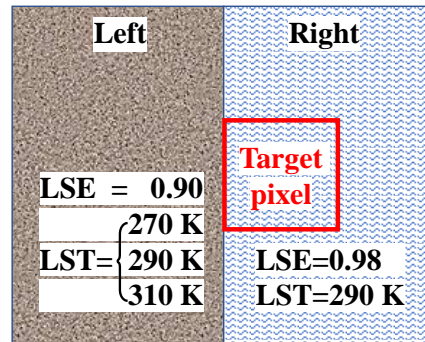
Fig. 2-7. Assumed scenario with two different surfaces. The target has the pixel size of 0.03 * 0.03 km.
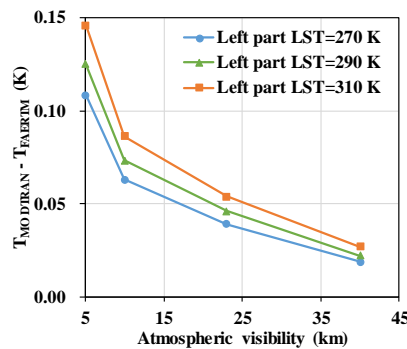
Fig. 2-8. Difference in simulated satellite brightness temperature between MODTRAN and FAERTM at 10 μm for the assumed scenario. The left part has emissivity of 0.9 and the right part has emissivity of 0.98. The temperature of the right part was fixed at 290 K while the temperature of the left part varied from 270 K to 310 K, with a step of 20 K. The aerosol type was set as RURAL.

As shown in Fig. 2-8, the differences in simulated satellite brightness temperature between MODTRAN and FAERTM coincide with those obtained for a homogeneous land surface. In fact, the results at wavelengths of 8.0, 9.0, 11.0 and 12.0 μm were also calculated and the difference was found to be smaller than that of 10.0 μm. For common cases, the validation results therefore showed that the discrepancy between FAERTM and MODTRAN is usually < 0.15 K.

2.5. Results

2.5.1. Adjacency effect dependence on horizontal and vertical calculation range

The integration range of the adjacency effect should be infinite horizontally and over the entire atmosphere vertically. However, aerosol density quickly decreases as altitude increases (Qiu et al., 2005). As shown in Fig. 2-9, aerosol scattering optical depth quickly approximates zero above 3 km; this means that calculation of scattered radiation > 3 km

only makes a very limited contribution to the total adjacency effect but increases calculation time. Additionally, when the adjacent pixel is far from the target pixel, the scattering angle increases, resulting in small ASPF values. Consequently, similarly to the VIS-NIR region, adjacency effect radiation is mainly related to adjacent pixels within several kilometers of the target pixel and scattered by the bottom atmospheres (Reinersman and Carder, 1995; Richter et al., 2006). It is therefore necessary to determine a horizontal and vertical cut-off distance for practical calculations. According to (Richter et al., 2006), the horizontal range of the adjacency effect usually has the same magnitude as the boundary aerosol scale height. For simplicity, in Fig. 2-10, the same value was therefore used both horizontally and vertically for each pre-set calculation range. Results showed that the adjacency effect first increased with the calculation range and then stabilized at about 3 km. The results for other input parameters such as LST, wavelength, and image spatial resolution showed a similar pattern. The horizontal and vertical cut-off range in this study was therefore set at 3 km.
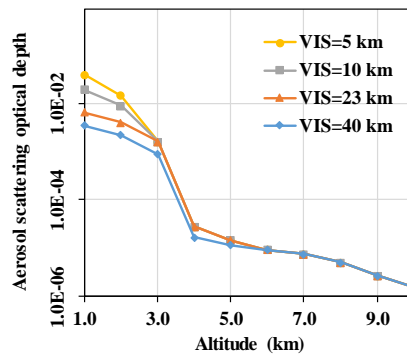
Fig. 2-9. Aerosol scattering optical depth as a function of altitude for different atmospheric visibilities (VIS). The wavelength and aerosol type were set as 10 μm and RURAL, respectively. The logarithmic y-axis was used.
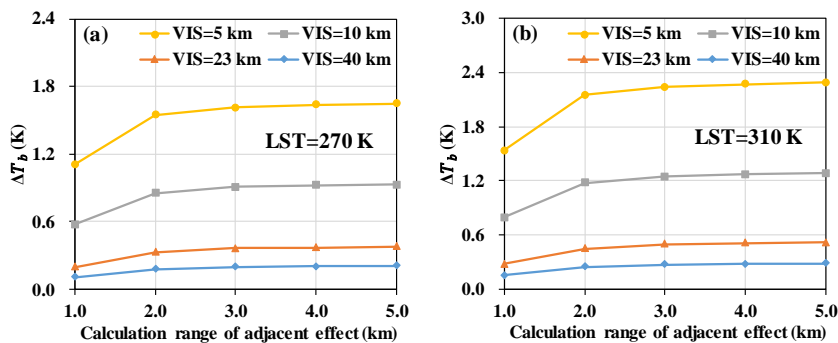
Fig. 2-10. Adjacency effect as a function of calculation range for different atmospheric visibilities (VIS). The wavelength, image spatial resolution, aerosol type, and LSE were set as 10 μm, 30 m, RURAL, and 0.90, respectively. The target and background temperature were the same, with LSTs of (a) 270 K and (b) 310 K.

2.5.2. Adjacency effect dependence on target and adjacent pixel emissivity

When the LSE of the target pixel decreased, the reflectance of the target pixel increased. As a result, the adjacency effect increased because more energy was reflected as the target pixel LSE changed from 0.98 to 0.90 (Fig. 2-11). However, the amount of increase was quite small, and different LSTs and atmospheric visibilities showed similar values. In fact, the proportion of energy scattered backward by the atmosphere in the TIR region is usually insignificant (Reck, 1976), indicating that the contribution of target-reflected adjacent pixel radiance is limited. Consequently, varying the target pixel LSE made no significant impact on the final sensor-observed radiance.
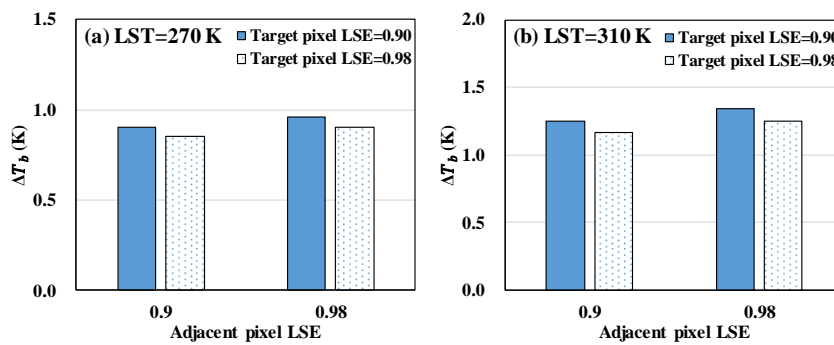
Fig. 2-11. Adjacency effect for different target and adjacent pixel emissivity combinations. The wavelength, image spatial resolution, aerosol type, and atmospheric visibility were 10 μm, 30 m, RURAL, and 10 km, respectively. The target and background temperature were the same, with LSTs of 270 K or 310 K.

2.5.3. Adjacency effect dependence on aerosol type and image spatial resolution

Results showed that the adjacency effect increased as image spatial resolution improved, regardless of LST (Fig. 2-12). For example, the adjacency effect was only about 0.3 K in images with a pixel size of 1.0×1.0 km. However, the adjacency effect increased by about three times as image spatial resolution increased to 5.0×5.0 m. When image spatial resolution was better than 0.03 km, the adjacency effect was no longer dominated by image spatial resolution but was mainly controlled by other parameters, such as LST.
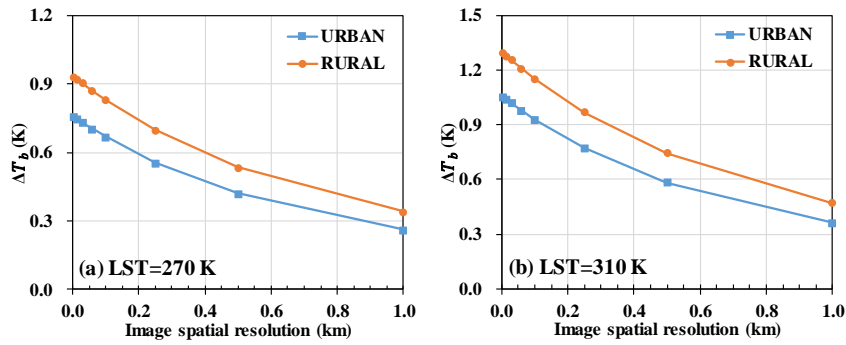
Fig. 2-12. Adjacency effect as a function of image spatial resolution for two different aerosol types. The wavelength, atmospheric visibility, and LSE were 10 μm, 10 km, and 0.98, respectively. Target and background temperature were the same, with LSTs of (a) 270 K and (b) 310 K.

Results also showed that the adjacency effect was more pronounced for RURAL than for URBAN aerosol types (Fig. 2-12). The difference varied from about 0.1 K to 0.2 K when image spatial resolution increased from 1.0 km to 5.0 m. However, in other respects, the adjacency effect for these two typical aerosol types was similar. The RURAL aerosol type was therefore used in the following analysis as an example.

2.5.4. Adjacency effect dependence on atmospheric visibility

Atmospheric visibility describes the scattering ability of the atmosphere. The lower the atmospheric visibility, the higher the atmospheric particle density, meaning that there should be a greater adjacency effect.

As shown in Fig. 2-13, when atmospheric visibility decreased, the adjacency effect soon became significant, reaching up to 1.6 K even for a cold surface with LST of 270 K. Additionally, the adjacency effect increased much more rapidly under conditions of large LST and high image spatial resolution. For example, in the case of an image spatial resolution of 0.03 km and LST of 310 K, the adjacency effect increased from 0.27 K to 2.25 K as atmospheric visibility decreased from 40.0 km to 5.0 km. In a case with image spatial resolution of 0.5 km and LST of 270 K, the adjacency effect only changed from 0.13 K to 0.91 K.
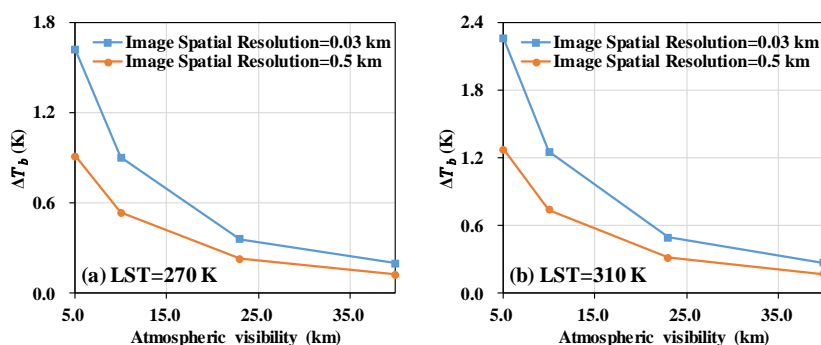
Fig. 2-13. Adjacency effect as a function of atmospheric visibility. The aerosol type, wavelength and LSE were RURAL, 10.0 μm and 0.98, respectively. The target and background temperature were set the same with the LST of (a) 270 K and (b) 310 K.

2.5.5. Adjacency effect dependence on target and adjacent pixel temperature

For a specific atmospheric profile, transmitted target pixel radiance and adjacency effect radiance are the two ground energy sources that affect the final sensor-observed radiation. Fig. 2-14 showed that the contribution of adjacent pixels to total observed radiance increased as adjacent pixel LST increased or target pixel LST decreased. The adjacency effect on satellite measurements therefore increased with increasing adjacent pixel LST (Fig. 2-15). Conversely, as target pixel LST increased, the adjacency effect decreased. We take as an example a common imaging condition with atmospheric visibility of 10 km, image spatial resolution of 30 m, and target pixel LST of 290K. Increasing adjacent pixel LST from 270 K to 310 K could result in the adjacency effect increasing by about 0.8 K (from 0.7 K to 1.5 K). Conversely, increasing target pixel LST from 270 K to 310 K leads to a decrease in the adjacency effect of about 0.4 K (from 1.3 K to 0.9 K), with maintaining adjacent pixel LST at 290 K.

In addition, we studied the adjacency effect, when defined as the observed target radiation difference between a case with target-to-background-radiation-contrast and one without [see Eq. 2-21] (Fig. 2-16). Results showed that, using this definition, the adjacency effect exists only when target pixel LST is different from adjacent pixel LST. The greater the difference, the larger the adjacency effect. For instance, given a common imaging condition with atmospheric visibility of 10 km, image spatial resolution of 30 m, and target pixel LST of 290 K, the adjacency effect increased from null to about 0.5 K with an increase in target-to-background-contrast from null to 30 K. With a fixed target-to-background-contrast, the adjacency effect was a little greater in cases where target pixel LST > adjacent pixel LST, compared to cases with target pixel LST < adjacent pixel LST.
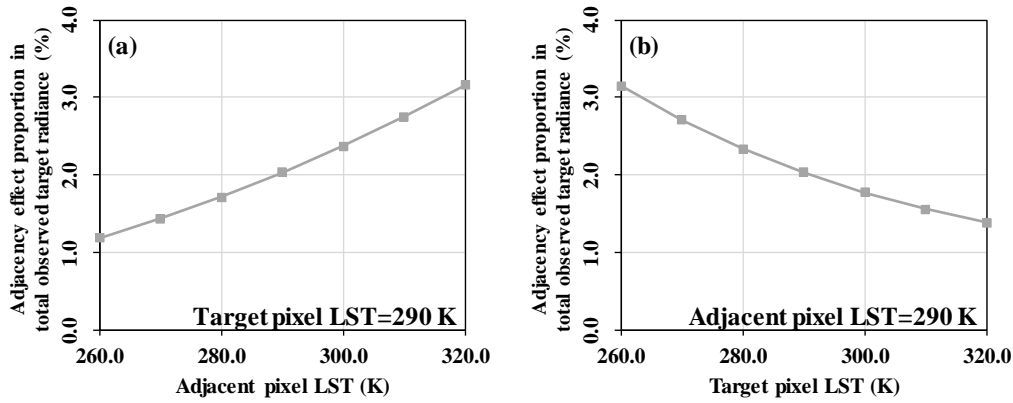
Fig. 2-14. The proportion of adjacency effect radiation in total observed target radiation as a function of (a) adjacent pixel LST, and (b) target pixel LST. Aerosol type, wavelength, image spatial resolution, and LSE were RURAL, 10 μm, 30 m, and 0.98, respectively.
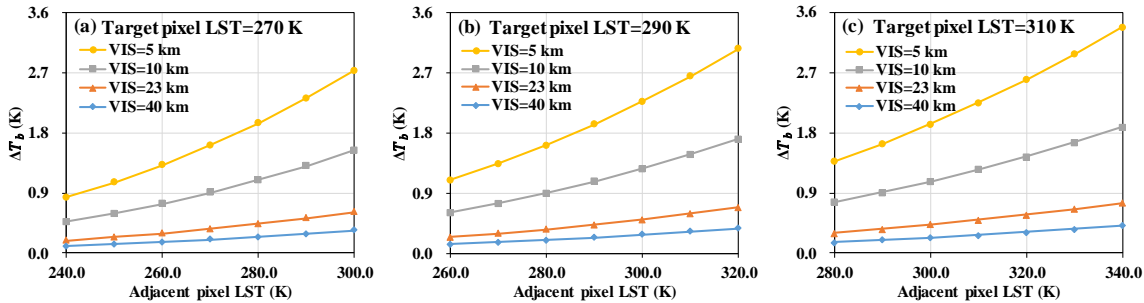
Fig. 2-15. Adjacency effect [defined as per Eq. 2-19] as a function of adjacent pixel temperature. Aerosol type, wavelength, image spatial resolution, and LSE were RURAL, 10 μm, 30 m, and 0.98, respectively. Target pixel temperature (TAT_LST) was (a) 270 K, (b) 290 K, and (c) 310 K. Adjacent pixel temperature varied from TAT_LST – 30 K to TAT_LST + 30 K, with a step of 10 K.
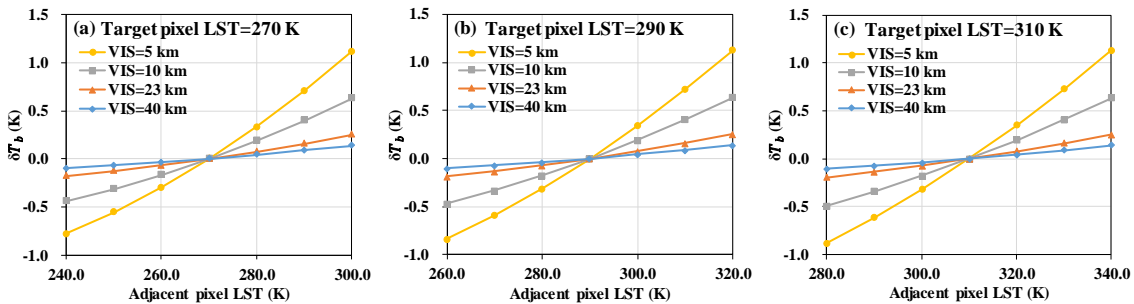
Fig. 2-16. Same as Fig. 2-15 but with adjacency effect defined by Eq. 2-21.

2.5.6. Adjacency effect dependence on wavelength

Changing the simulated wavelength produced different adjacency effect, mainly because some parameters used in FAERTM are wavelength-dependent, such as aerosol scattering optical depth and atmospheric transmittance [see Eq. 2-9 and Eq. 2-17]. As shown in Fig. 2-17 for both definitions Eq. 2-19 and Eq. 2-21, the adjacency effect decreased as wavelength increased, except for the wavelengths of 8.0 and 12.0 μm. The irregularity of

these two positions could be explained through analysis of aerosol scattering optical depth and atmospheric transmittance of the five wavelengths.

Given the 1976 U.S Standard atmospheric type and 10 km atmospheric visibility, transmittances were 0.51, 0.75, 0.73, 0.72, and 0.85 for wavelengths of 8.0, 9.0, 10.0, 11.0, and 12.0 μm, respectively. Aerosol scattering optical depth as a function of wavelength is given in Fig. 2-18. As expected, the smallest atmospheric transmittance and smallest aerosol scattering optical depth both occurred at 8 μm, resulting in a minimum adjacency effect at this wavelength.
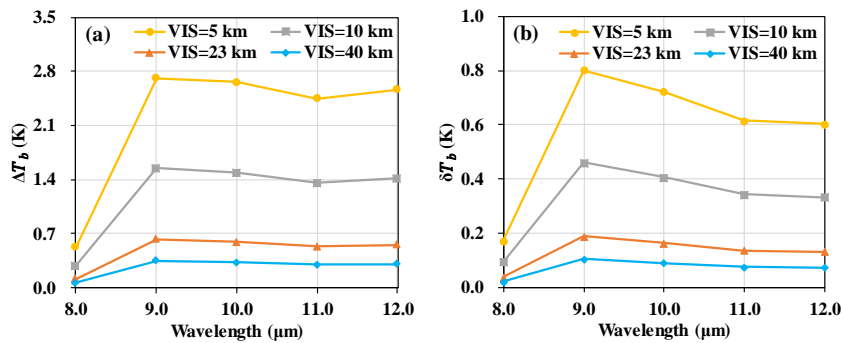
Fig. 2-17. Adjacency effect results, with this defined as per (a) Eq. 2-19, and (b) Eq. 2-21, as a function of wavelength for different atmospheric visibilities (VIS). Aerosol type, image spatial resolution, and LSE were RURAL, 30 m, and 0.98, respectively. Target and adjacent pixel temperatures were set as 290 K and 310 K, respectively.
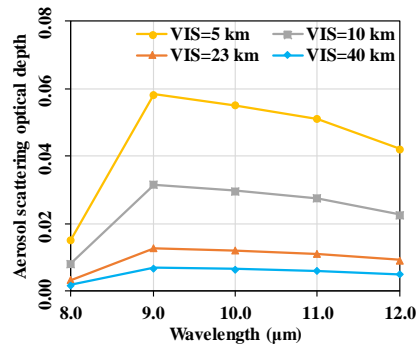
Fig. 2-18. Aerosol scattering optical depth (sum of the lower 3 km) as a function of wavelength for different atmospheric visibilities (VIS). Wavelength and aerosol type were set as 10 μm and RURAL, respectively.

Since aerosol scattering optical depth decreases with an increase in wavelength from 9.0 μm to 12.0 μm, the adjacency effect should decrease with wavelength if atmospheric transmittances were the same at these wavelengths. However, when considering atmospheric transmittances at wavelengths of 9.0, 10.0, 11.0, and 12.0 μm, the former three have similar values, but there is larger atmospheric transmittance at 12.0 μm. The decrease in the adjacency effect caused by decreasing aerosol scattering optical depth is therefore

compensated for by the increase in atmospheric transmittance at 12.0 μm; this is expected to explain the small anomaly observed at 12.0 μm.

2.5.7. Adjacency effect analysis on actual satellite data

In addition to the above point-based simulations, experiments using actual satellite data were also conducted, to preliminarily interpret adjacency effect magnitude in actual satellite measurements. MOD11, AST05, and AST08 products were used to provide the land surface radiation field. According to location and acquisition time of the selected study area images (see Section 2.3.3), atmospheric transmittance, downwelling, and upwelling radiance were calculated by using the Mid-Latitude Winter atmospheric type provided in MODTRAN. The RURAL aerosol type and atmospheric visibility of 10 km were used to compute single scattered and target-reflected adjacent pixel radiance. Since FAERTM is a monochromatic model, the adjacency effect was first calculated wavelength by wavelength, then weighted using the MODIS and ASTER channel spectral response function (SRF). The results for Band 31 of MODIS and Band 14 of ASTER are given as examples. As shown in Fig. 2-19, the adjacency effect, defined according to Eq. 2-19, was present in every pixel for both images. For MODIS data with pixel size of 1000 m * 1000 m (Fig. 2-19(a)), the maximum influence caused by the adjacency effect was about 0.5 K. For ASTER data with pixel size of 90 m * 90 m (Fig. 2-19(b)), even the minimum influence of the adjacency effect was > 1.0 K.

We also considered the adjacency effect, using its definition as observed target radiation difference between a case with target-to-background-radiation-contrast and one without Eq. 2-21. As shown in Fig. 2-20, under this definition, there was very limited influence of the adjacency effect on satellite measurements for MODIS imagery. In the case of the ASTER image, which has much higher spatial resolution, the adjacency effect for pixels at radiation edges (such as river or lake shores) was as high as 0.35 K. It can be assumed that in cases with higher spatial resolution measurements and larger target-background-contrast, the adjacency effect could be a little bit higher.
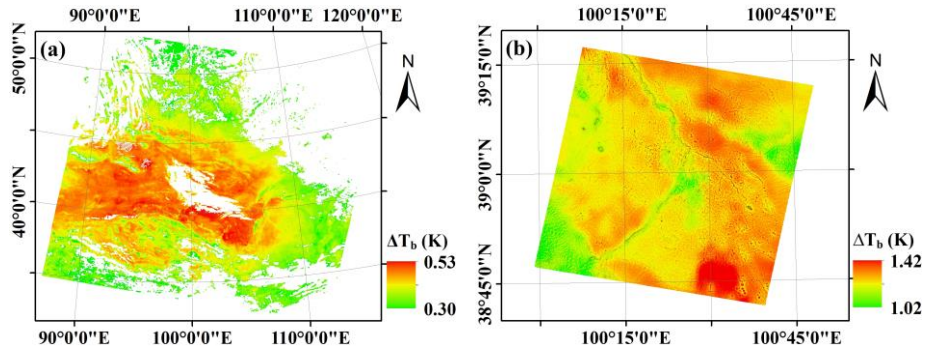
Fig. 2-19. Adjacency effect [defined as per Eq. 2-19] results based on (a) MOD11 product (Band 31 with bandwidth of 10.78 ~ 11.28 μm), and (b) AST05 and AST08 products (Band 14 with bandwidth of 10.95 ~ 11.65 μm). Atmospheric type, atmospheric visibility and aerosol type were Mid-Latitude Winter, 10 km, and RURAL, respectively.
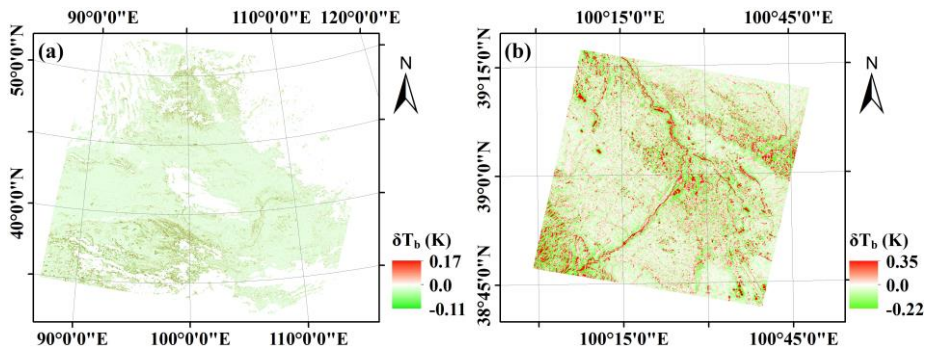
Fig. 2-20. Same as Fig. 2-19 but with adjacency effect defined by Eq. 2-21.

2.6. Discussions and conclusions

Prior works have documented the development of a number of LST retrieval algorithms over the last several decades, such as the split window method, which has been successfully used to generate global LST products (Becker and Li, 1990; Wan, 2014; Wan and Dozier, 1996). Existing LST retrieval algorithms assume a negligible adjacency effect or consider this to be already well addressed by TIR signals. To our knowledge, no studies have focused on quantifying the adjacency effect on TIR observations. As the TIR image spatial resolution improves nowadays, the adjacency effect on TIR satellite measurements needs to be studied to further improve LST retrieval accuracy. In this study, a physical adjacency effect simulation model, FAERTM, was developed. After comparison with MODTRAN, FAERTM was used to quantify the adjacency effect on TIR observations for different atmospheric and imaging conditions.

It is shown that the adjacency effect mainly originates from pixels within 3 km of the target and is not sensitive to aerosol type and LSE. Additionally, in contrast to scenarios with clear atmospheres, coarse image spatial resolution, and cold adjacent pixels, adjacency

effect magnitude increased with a decrease in atmospheric visibility, an improvement in image spatial resolution, or an increase in adjacent pixel radiation. In extreme conditions, the adjacency effect magnitude may even exceed 3.0 K. It is also shown that, as wavelength increased, the adjacency effect generally decreases, except at 8 μm; at this wavelength, atmospheric transmittance and aerosol scattering optical depth are both quite small, leading to most adjacency effect radiance being absorbed and thus not being observed by the sensor. This phenomenon has been confirmed using simulated path scattered radiance values from MODTRAN; the 8 μm wavelength always has lower values than other wavelengths. For example, in a moderate humidity (3.62 g/cm^2) and turbid (10 km) atmosphere, path-scattered radiance at 8 μm is about 4.63×10^{-9} (W Sr^{-1} cm^{-2} cm^{-1}), compared with 2.28×10^{-8} (W Sr^{-1} cm^{-2} cm^{-1}) at 9 μm.

These findings clearly show that the adjacency effect should be considered in the TIR region, at least for some specific cases, such as the atmospheric visibility is smaller than 23 km or the image spatial resolution is higher than 1.0 km. Otherwise, significant underestimations would be introduced to the satellite observations. For the purpose of further improving LST retrieval accuracy, the adjacency effect should either be independently addressed from TIR signals before applying commonly used LST retrieval algorithms or should be integrated into existing LST retrieval algorithms to develop new ones. For each of the two potential approaches, the proposed FAERTM could be a useful tool because it can be used to quantitatively calculate this effect for given atmospheric and land surface conditions.

3 | Modelling of the impact of 3-D structures and their radiation on TIR measurements in urban areas

Land surface temperature (LST) is a key parameter for many fields of study. Currently, LST retrieved from satellite thermal infrared (TIR) measurements is attainable with an accuracy of about 1.0 K for most natural flat surfaces. However, over urban areas, TIR measurements are influenced by three-dimensional (3-D) structures and their radiation that could degrade the performance of existing LST retrieval algorithms. Therefore, quantitative models are needed to investigate such impact. Current 3-D radiative transfer models are generally based on time-consuming numerical integrations whose solutions are not analytical, and are therefore difficult to exploit in the methods of physical retrieval of LST in urban areas. This paper proposes an analytical thermal infrared radiative transfer model over urban areas (ATIMOU) that considers the impact of 3-D structures and their radiation. The magnitude of this impact on TIR measurements is investigated in detail, using ATIMOU, under various conditions. Simulations show that failure to acknowledge this impact can potentially introduce a 1.87 K bias to the ground brightness temperature for street canyon whose ratio "wall height / road width" is 2.0, wall and road temperature is 300 K, wall emissivity is 0.906, and road emissivity is 0.950. This bias reaches 4.60 K if road emissivity decreases to 0.921, and road temperature decreases to 260 K. ATIMOU is also compared to the discrete anisotropic radiative transfer (DART) model. Small mean absolute error of 0.10 K was found between the models regarding the simulated ground brightness temperatures, indicating that ATIMOU is in good agreement with DART.

3.1. Introduction

Land surface temperature (LST) is one of the most important Earth surface parameters, as it is the key factor affecting the energy balance of the Earth and is required by studies of global warming, evaporation, urban heat islands, et. al (Anderson et al., 2008; Karnieli et al., 2010; Kustas and Anderson, 2009; Li et al., 2013a; Zhang et al., 2008). Thermal infrared (TIR) remote sensing provides a suitable and efficient way to obtain accurate LST information from the Earth's surface. Regional and global LST may be obtained, based on TIR measurements, using existing LST retrieval algorithms. After decades of improvement, various types of LST retrieval algorithms have been developed (Coll and Caselles, 1997; Jimenez-Munoz and Sobrino, 2003; Li et al., 2013a; Sattari and Hashim, 2014) and have achieved great success for natural flat surfaces (Chedin et al., 1982; Gillespie et al., 1998; McMillin, 1975; Ottle and Vidal-Madjar, 1992; Qin et al., 2001b; Sobrino et al., 1996; Wan and Li, 1997). However, in urban areas, three-dimensional (3-D) structures and their radiation affect satellite TIR measurements, especially in high spatial resolution images (Fontanilles et al., 2008; Pallotta et al., 2006), because the observed radiance would increase due to the radiation of the surroundings and reflections inside 3-D structures; the observed signal would be anisotropic through various viewing angles. Consequently, the performance of existing LST retrieval algorithms may deteriorate significantly if this impact is not well addressed in observed signals. Therefore, quantitative models are needed to investigate the impact of 3-D structures and their radiation on TIR measurements in urban areas.

To understand the anisotropic thermal behavior of urban areas, a number of previous researches have studied the 3-D surface modelling. Johnson *et al.* (Johnson et al., 1991) proposed the surface heat island model (SHIM) to address the effects of building 3-D geometries. Voogt (Voogt, 1995) developed a model to estimate the observed radiance in urban areas by considering five components: roof, sunlit and shadowed ground, sunlit and shadowed walls. Later, Krayenhoff *et al.* (Krayenhoff and Voogt, 2007) proposed a more detailed model—temperatures of urban facets in 3-D (TUF-3D)—to study urban surface temperatures for a variety of surface geometries and properties. In their model, buildings were divided into cubic cells and internal building temperature was also considered. These three models are excellent thermal tools with which to estimate energy balance and study urban climate (Masson, 2000); however, they do not allow for analysis of the dominating factors that impact satellite-observed TIR signals at the sensor level in detail (Fontanilles

et al., 2008). Gastellu-Etchegorry *et al.* (Gastellu-Etchegorry et al., 2004; Gastellu-Etchegorry et al., 2015; Guillevic and Gastellu-Etchegorry, 2003) extended the discrete anisotropic radiative transfer (DART) model to the TIR region, providing a modified model capable of simulating the sensor-observed TIR spectral radiance of 3-D scenes. Although the current version of DART can also allow a term by term analysis of the radiative contributors on the signal at sensor level, the model should be run several times which is not convenient for schematic case studies (Fontanilles et al., 2008; Pallotta et al., 2006). Thus, Pallotta *et al.* (Pallotta et al., 2006) developed another model to estimate the sensor-observed radiance. However, vertical surfaces such as building walls could only be processed approximately because this model used a regular grid to digitalize the relief. Fontanilles *et al.* (Fontanilles et al., 2008) proposed the thermal infrared radiance simulation with aggregation model (TITAN), which is able to study the main radiative sources in the urban areas observed by satellite. However, these three models all rely on discrete 3-D scenes of the Earth's surface and outputs were calculated based on time-consuming numerical integrations (Fontanilles et al., 2008). Additionally, as no analytical solutions have been provided for these models due to the complex calculation process involved, it is difficult to develop physical LST retrieval models for urban areas directly based on them. To our knowledge, the currently available analytical model for 3-D surface modelling is the one proposed by Caselles and Sobrino (Caselles and Sobrino, 1989), which was designed for orange groves but could be applied to urban areas assuming the emissivity of roof is the same as the building walls. However, this model was derived on the basis of the linearization of Planck function using the first-order Taylor expansion, which maybe not accurate when the temperatures of each component inside the street canyon is not close to the overall effective brightness temperature. Besides, all the multi-reflections have been ignored in their model leading to the increase of bias as emissivity decreases. Therefore, to study the relationships between parameters of street canyons and their corresponding TIR measurements, a more accurate analytical TIR radiative transfer model with consideration of the impact of 3-D structures and their radiation is required.

This chapter proposes a new model, the analytical thermal infrared radiative transfer model over urban areas (ATIMOU), which could provide analytical solutions of the ground and satellite TIR measurement in urban areas. Application of this model to different street canyon scenarios allows for detailed quantitative investigation of the impact of 3-D structures and their radiation on the TIR measurements. The ATIMOU is also compared to other existing models including the DART. This paper is organized as follows: Section 3.2

describes the mathematical formulations of the proposed model. Section 3.3 analyzes the magnitude of the impact of 3-D structures and their radiation on TIR measurement under different conditions. Section 3.4 provides the results of comparison between the proposed ATIMOU and other models. Finally, Section 3.5 summarizes the main findings.

3.2. Methodology

In this study, a street canyon in an urban area is defined as two buildings situated on either side of a road and oriented in a north-south direction. The 3-D structure is illustrated in Fig. 3-1. with W, L, and H representing the road width, road length, and wall height, respectively. Atmospheric spherical albedo at the bottom of the atmosphere is represented by ρ_A, and $L^\downarrow$ is the atmospheric downwelling radiance (wavelength λ is omitted here and hereafter for simplicity). The cross-section of the atmosphere above the road at the roof level, i.e. the plane $A_1A_2A_3A_4$ in Fig. 3-1., is denoted A. The emissivity of the roof, left wall (LW), road (Rd), and right wall (RW) are symbolized as ε_{roof}, ε_{LW}, ε_{Rd}, and ε_{RW}, respectively, while LST_{roof}, LST_{LW}, LST_{Rd}, and LST_{RW} are the corresponding temperatures. Moreover, two additional assumptions have been made for simplicity: (a) the walls of the building are all perpendicular to the ground and have the same height; (b) all facets are Lambertian and flat. Using the parameters of the scenario described above, the ATIMOU is developed in the following sections.
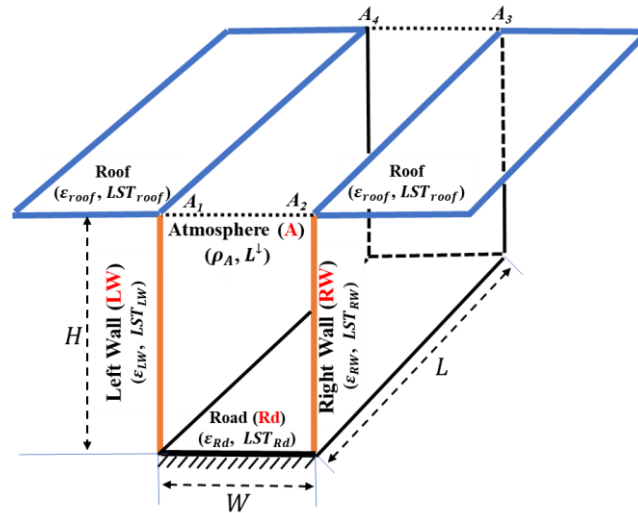
Fig. 3-1. Illustration of a street canyon in an urban area. W, L, and H are the road width, road length, and wall height, respectively. ρ_A is the atmospheric spherical albedo at the bottom of the atmosphere and $L^\downarrow$ is the atmospheric downwelling radiance. ε_{roof}, ε_{LW}, ε_{Rd}, and ε_{RW} are the emissivity of roof, left wall, road, and right wall respectively, whereas LST_{roof}, LST_{LW}, LST_{Rd}, and LST_{RW} are the corresponding temperatures.

3.2.1. Development of the analytical model for radiative transfer over a street canyon

When considering 3-D structures in urban areas, the compositions inside the instantaneous field of view (IFOV) may vary with viewing angle and IFOV size. Consequently, the impact of 3-D structures and their radiation on ground observed radiance of the target pixel could be different for different conditions.

To determine the ground observed radiance of the target pixel, the 3-D structure of an urban area was first projected onto the ground along the direction of view. Then the solid angles of the projections of each composition inside the IFOV of the sensor were calculated (Fig. 3-2), allowing the proportion of each composition in the target pixel to be determined. Finally, the ground observed radiance of the target pixel could be estimated using the weighted sum method Eq. 3-1. However, the radiance of each composition used in the weighted sum method should not be their self-emitted radiance; rather, it should be their surface-leaving radiance considering the impact of 3-D structures and their radiation. Since building roofs are not affected by 3-D structures and their radiation in urban areas, the corresponding ground observed radiance of a roof can be calculated using Eq. 3-2, according to the traditional radiative transfer model (Becker and Li, 1990; Wan and Dozier, 1996; Wan and Li, 1997).
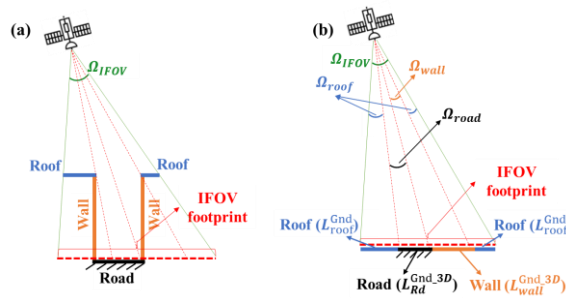
Fig. 3-2. Illustrations of (a) the viewing geometry of the 3-D structures in urban areas, (b) the two-dimensional projection of 3-D structures in urban areas. The solid angle of the entire IFOV of the sensor is represented by Ω_{IFOV}, whereas Ω_{roof}, Ω_{road}, and Ω_{wall} are the solid angles of the projections regarding to the components of roof, road, and wall inside the IFOV of the sensor, respectively.

$$L^{Gnd\_3D} = B\left(T^{Gnd\_3D}\right) = \frac{\Omega_{roof}}{\Omega_{IFOV}} L_{roof}^{Gnd} + \frac{\Omega_{road}}{\Omega_{IFOV}} L_{Rd}^{Gnd\_3D} + \frac{\Omega_{wall}}{\Omega_{IFOV}} L_{wall}^{Gnd\_3D} \qquad \text{Eq. 3-1}$$

in which

$$L_{roof}^{Gnd} = \varepsilon_{roof} B\left(LST_{roof}\right) + \left(1 - \varepsilon_{roof}\right) L^{\downarrow}$$

<div align="right">Eq. 3-2</div>

where L^{Gnd-3D} and T^{Gnd-3D} are, respectively, the ground observed radiance and brightness temperature of the target pixel with impact of 3-D structures and their radiation; $B(T)$ is the Planck function at temperature T; Ω_{IFOV} is the solid angle of the entire IFOV of the sensor; Ω_{roof}, Ω_{road}, and Ω_{wall} are the solid angles of the projections regarding to the components of roof, road, and wall inside the IFOV of the sensor, respectively, which are not only dependent on the viewing zenith and azimuth angles, but also dependent on the geometric parameters of the street canyon. Besides, the parallel projection method has been used in this study to determine the projected area of each component inside the sensor's IFOV along the viewing direction; L_{roof}^{Gnd} is the ground observed radiance of the roof and will not be affected by the 3-D structures and their radiation; and L_{Rd}^{Gnd-3D} and L_{wall}^{Gnd-3D} are, respectively, the ground observed radiance of the road and wall with the impact of 3-D structures and their radiation. Moreover, because the parallel projection method has been used as stated above, only one building wall could be observed by the remote sensor given a specific viewing direction. Therefore, assuming L_{LW}^{Gnd-3D} and L_{RW}^{Gnd-3D} are the ground observed radiance of the left wall and right wall with the impact of 3-D structures and their radiation, respectively, L_{wall}^{Gnd-3D} is then equal to L_{LW}^{Gnd-3D} or L_{RW}^{Gnd-3D} depending on the viewing angle. As a result, L_{Rd}^{Gnd-3D}, L_{LW}^{Gnd-3D}, and L_{RW}^{Gnd-3D} are the critical parameters for developing the analytical model.

When the 3-D structures in urban areas are taken into consideration, the environmental radiance above the road and wall is no longer determined solely by atmospheric downwelling radiance, but also by the radiation of surroundings and the reflections inside the 3-D structures. Inside the street canyon, energy is mainly exchanged among four components: the atmosphere, left wall, road, and right wall (Fig. 3-1.). As stated above, the ground observed radiance of the road is L_{Rd}^{Gnd-3D}, then the power that leaves the surface of road (Q_{Rd}) can be expressed by Eq. 3-3.

$$Q_{Rd} = L \cdot W \cdot \pi L_{Rd}^{Gnd-3D}$$

<div align="right">Eq. 3-3</div>

In addition, considering that the emissivity and temperature of the road are ε_{Rd} and LST_{Rd} respectively, the power that comes from the surroundings and arrives at the road is Q_{Rd}^{Evn-3D}, then the power that leaves the surface of road (Q_{Rd}) can also be expressed by:

$$Q_{Rd} = L \cdot W \cdot \pi \varepsilon_{Rd} B\left(LST_{Rd}\right) + \left(1 - \varepsilon_{Rd}\right) Q_{Rd}^{Evn-3D}$$

<div align="right">Eq. 3-4</div>

Combining Eq. 3-3 and Eq. 3-4, Eq. 3-5 could be obtained:

$$L \cdot W \cdot \pi L_{Rd}^{Gnd\_3D} = L \cdot W \cdot \pi \varepsilon_{Rd} B(LST_{Rd}) + (1 - \varepsilon_{Rd}) Q_{Rd}^{Evn\_3D} \qquad \text{Eq. 3-5}$$

in which

$$Q_{Rd}^{Evn\_3D} = L \cdot W \cdot \pi L_A^{Gnd\_3D} \cdot F_{A \to Rd} + L \cdot H \cdot \pi L_{LW}^{Gnd\_3D} \cdot F_{LW \to Rd} + L \cdot H \cdot \pi L_{RW}^{Gnd\_3D} \cdot F_{RW \to Rd} \qquad \text{Eq. 3-6}$$

where $L_A^{Gnd\_3D}$ is the radiance of the atmosphere with the impact of 3-D structures and their radiation, and $F_{X \to Rd}$ is the view factor from surface X to surface Rd ($X = A, LW, RW$), which represents the fraction of energy leaving surface X that reaches surface Rd.

Substituting Eq. 3-6 into Eq. 3-5, the equation below can be obtained:

$$-W \cdot L_{Rd}^{Gnd\_3D} + (1 - \varepsilon_{Rd})(W \cdot F_{A \to Rd} \cdot L_A^{Gnd\_3D} + H \cdot F_{LW \to Rd} \cdot L_{LW}^{Gnd\_3D}$$
$$+ H \cdot F_{RW \to Rd} \cdot L_{RW}^{Gnd\_3D}) + W \cdot \varepsilon_{Rd} B(LST_{Rd}) = 0 \qquad \text{Eq. 3-7}$$

Similarly, three equations can be obtained for the surfaces of atmosphere (A), left wall (LW), and right wall (RW) as below [see Eq. 3-8 ~ Eq. 3-10]:

$$-W \cdot L_A^{Gnd\_3D} + \rho_A (H \cdot L_{LW}^{Gnd\_3D} \cdot F_{LW \to A} + W \cdot L_{Rd}^{Gnd\_3D} \cdot F_{Rd \to A}$$
$$+ H \cdot L_{RW}^{Gnd\_3D} \cdot F_{RW \to A}) + W \cdot L^{\downarrow} = 0 \qquad \text{Eq. 3-8}$$

$$-H \cdot L_{LW}^{Gnd\_3D} + (1 - \varepsilon_{LW})(W \cdot L_A^{Gnd\_3D} \cdot F_{A \to LW} + W \cdot L_{Rd}^{Gnd\_3D} \cdot F_{Rd \to LW}$$
$$+ H \cdot L_{RW}^{Gnd\_3D} \cdot F_{RW \to LW}) + H \cdot \varepsilon_{LW} B(LST_{LW}) = 0 \qquad \text{Eq. 3-9}$$

$$-H \cdot L_{RW}^{Gnd\_3D} + (1 - \varepsilon_{RW})(W \cdot L_A^{Gnd\_3D} \cdot F_{A \to RW} + H \cdot L_{LW}^{Gnd\_3D} \cdot F_{LW \to RW}$$
$$+ W \cdot L_{Rd}^{Gnd\_3D} \cdot F_{Rd \to RW}) + H \cdot \varepsilon_{RW} B(LST_{RW}) = 0 \qquad \text{Eq. 3-10}$$

where $F_{P \to Q}$ represents the view factor from surface P to surface Q ($P, Q = Rd, A, LW, RW$ and $P \neq Q$). Combining Eq. 3-7 – Eq. 3-10, an equation system can be obtained with four unknowns, three of which are the required parameters $L_{Rd}^{Gnd\_3D}$, $L_{LW}^{Gnd\_3D}$, and $L_{RW}^{Gnd\_3D}$ [see Eq. 3-11].

$$A \begin{bmatrix} L_{Rd}^{Gnd\_3D} & L_A^{Gnd\_3D} & L_{LW}^{Gnd\_3D} & L_{RW}^{Gnd\_3D} \end{bmatrix}^T = \boldsymbol{B} \qquad \text{Eq. 3-11}$$

in which

$$A = \begin{bmatrix} -W & (1-\varepsilon_{Rd})W \cdot F_{A \to Rd} & (1-\varepsilon_{Rd})H \cdot F_{LW \to Rd} & (1-\varepsilon_{Rd})H \cdot F_{RW \to Rd} \\ \rho_A W \cdot F_{Rd \to A} & -W & \rho_A H \cdot F_{LW \to A} & \rho_A H \cdot F_{RW \to A} \\ (1-\varepsilon_{LW})W \cdot F_{Rd \to LW} & (1-\varepsilon_{LW})W \cdot F_{A \to LW} & -H & (1-\varepsilon_{LW})H \cdot F_{RW \to LW} \\ (1-\varepsilon_{RW})W \cdot F_{Rd \to RW} & (1-\varepsilon_{RW})W \cdot F_{A \to RW} & (1-\varepsilon_{RW})H \cdot F_{LW \to RW} & -H \end{bmatrix} \qquad \text{Eq. 3-12}$$

$$\boldsymbol{B} = \begin{bmatrix} -W \cdot \varepsilon_{Rd} B(LST_{Rd}) & -W \cdot L^{\downarrow} & -H \cdot \varepsilon_{LW} B(LST_{LW}) & -H \cdot \varepsilon_{RW} B(LST_{RW}) \end{bmatrix}^T \qquad \text{Eq. 3-13}$$

After the matrix manipulation of $\boldsymbol{A^{-1}B}$, the four unknowns can be obtained and L^{Gnd_3D}

can be expressed by an analytical equation after combining Eq. 3-1, Eq. 3-2, Eq. 3-11, Eq. 3-12, and Eq. 3-13, provided that the geometric and radiative properties of the street canyon are known. In addition, according to the traditional radiative transfer model, the satellite observed radiance (L^{TOA_3D}) and brightness temperature (T^{TOA_3D}) of the target pixel over a street canyon with impact of 3-D structures and their radiation could be expressed by:

$$L^{TOA\_3D} = B(T^{TOA\_3D}) = \tau(\theta)L^{Gnd\_3D} + L^{\uparrow}(\theta) \qquad \text{Eq. 3-14}$$

where $\tau(\theta)$ and $L^{\uparrow}(\theta)$ are the total atmospheric transmittance and atmospheric upwelling radiance along the viewing direction with zenith angle of θ, respectively.

3.2.2. Simplification of the analytical model for radiative transfer over a street canyon

In previous section, the exact solutions of $L_{Rd}^{Gnd\_3D}$, $L_{A}^{Gnd\_3D}$, $L_{LW}^{Gnd\_3D}$, and $L_{RW}^{Gnd\_3D}$ have been provided in the matrix form ($A^{-1}B$), because their analytical forms are very complex. Therefore, they are very difficult to use to analyze the relationships between the input parameters and the magnitude of the impact of 3-D structures and their radiation. In this section, these analytical solutions have been simplified after applying some reasonable assumptions.

Considering that the two walls are parallel to each other, some of the view factors in Eq. 3-12 are therefore equivalent. Assuming that the length of road and building is infinite, these view factors can be classified into two types: one is the view factor between "two infinitely long, directly opposed parallel plates of the same finite width" (Howell et al., 2010) represented by $F_{Rd \rightarrow A}$, $F_{A \rightarrow Rd}$, $F_{RW \rightarrow LW}$, $F_{LW \rightarrow RW}$; the other is the view factor between "two infinitely long plates of unequal widths, having one common edge, and at an angle of 90° to each other" (Howell et al., 2010) represented by $F_{A \rightarrow LW}$, $F_{Rd \rightarrow LW}$, $F_{A \rightarrow RW}$, $F_{Rd \rightarrow RW}$, $F_{LW \rightarrow A}$, $F_{RW \rightarrow A}$, $F_{LW \rightarrow Rd}$, and $F_{RW \rightarrow Rd}$. According to previous study (Howell et al., 2010), the former can be calculated using Eq. 3-15 and Eq. 3-16 while the latter can be calculated using Eq. 3-17 and Eq. 3-18.

$$F_{Rd \rightleftharpoons A} = F_{Rd \rightarrow A} = F_{A \rightarrow Rd} = \sqrt{1 + \left(\frac{H}{W}\right)^2} - \frac{H}{W} \qquad \text{Eq. 3-15}$$

$$F_{RW \rightleftharpoons LW} = F_{RW \rightarrow LW} = F_{LW \rightarrow RW} = \sqrt{1 + \left(\frac{W}{H}\right)^2} - \frac{W}{H} \qquad \text{Eq. 3-16}$$

$$F_{A,Rd \to LW,RW} = F_{A \to LW} = F_{Rd \to LW} = F_{A \to RW} = F_{Rd \to RW} = 0.5 \left[\frac{H}{W} + 1 - \sqrt{\left(\frac{H}{W}\right)^2 + 1} \right] \qquad \text{Eq. 3-17}$$

$$F_{LW,RW \to A,Rd} = F_{LW \to A} = F_{RW \to A} = F_{LW \to Rd} = F_{RW \to Rd} = 0.5 \left[\frac{W}{H} + 1 - \sqrt{\left(\frac{W}{H}\right)^2 + 1} \right] \qquad \text{Eq. 3-18}$$

After applying Eq. 3-15 ~ Eq. 3-18, the analytical solutions of $L_{Rd}^{Gnd\_3D}$, $L_{A}^{Gnd\_3D}$, $L_{LW}^{Gnd\_3D}$, and $L_{RW}^{Gnd\_3D}$ then can be expressed as follows:

$$\begin{bmatrix} L_{Rd}^{Gnd\_3D} \\[2mm] L_{A}^{Gnd\_3D} \\[2mm] L_{LW}^{Gnd\_3D} \\[2mm] L_{RW}^{Gnd\_3D} \end{bmatrix} = \begin{bmatrix} \dfrac{W \cdot (C_{11} - \rho_A C_1) \cdot \varepsilon_{Rd} B(LST_{Rd}) + W \cdot \rho_{Rd} C_{12} \cdot L^{\downarrow} + H \cdot \rho_{Rd} (\rho_A F_{Rd \rightleftharpoons A} + 1) C_2}{W \cdot m\_denom} \\[4mm] \dfrac{W \cdot (C_{11} - \rho_{Rd} C_1) \cdot L^{\downarrow} + W \cdot \rho_A C_{12} \cdot \varepsilon_{Rd} B(LST_{Rd}) + H \cdot \rho_A (\rho_{Rd} F_{Rd \rightleftharpoons A} + 1) C_2}{W \cdot m\_denom} \\[4mm] \dfrac{H \cdot (C_{31} - \rho_{RW} C_3) \cdot \varepsilon_{LW} B(LST_{LW}) + H \cdot \rho_{LW} C_{32} \cdot \varepsilon_{RW} B(LST_{RW}) + W \cdot \rho_{LW} (\rho_{RW} F_{RW \rightleftharpoons LW} + 1) C_4}{H \cdot m\_denom} \\[4mm] \dfrac{H \cdot (C_{31} - \rho_{LW} C_3) \cdot \varepsilon_{RW} B(LST_{RW}) + H \cdot \rho_{RW} C_{32} \cdot \varepsilon_{LW} B(LST_{LW}) + W \cdot \rho_{RW} (\rho_{LW} F_{RW \rightleftharpoons LW} + 1) C_4}{H \cdot m\_denom} \end{bmatrix} \qquad \text{Eq. 3-19}$$

in which

$$C_{11} = 1 - F_{RW \rightleftharpoons LW}^2 \rho_{LW} \rho_{RW} \qquad \text{Eq. 3-20}$$

$$C_1 = F_{LW,RW \to A,Rd} F_{A,Rd \to LW,RW} \left(2F_{RW \rightleftharpoons LW} \rho_{LW} \rho_{RW} + \rho_{LW} + \rho_{RW} \right) \qquad \text{Eq. 3-21}$$

$$C_{12} = F_{Rd \rightleftharpoons A} C_{11} + C_1 \qquad \text{Eq. 3-22}$$

$$C_2 = F_{LW,RW \to A,Rd} \left(\left(F_{RW \rightleftharpoons LW} \rho_{RW} + 1 \right) \varepsilon_{LW} B(LST_{LW}) + \left(F_{RW \rightleftharpoons LW} \rho_{LW} + 1 \right) \varepsilon_{RW} B(LST_{RW}) \right) \qquad \text{Eq. 3-23}$$

$$m\_denom = \left(F_{Rd \rightleftharpoons A}^2 \rho_A \rho_{Rd} - 1 \right) \left(F_{RW \rightleftharpoons LW}^2 \rho_{LW} \rho_{RW} - 1 \right) \qquad \text{Eq. 3-24}$$
$$- \left(\rho_{Rd} + \rho_A \left(2F_{Rd \rightleftharpoons A} \rho_{Rd} + 1 \right) \right) \left(\rho_{RW} + \rho_{LW} \left(2F_{RW \rightleftharpoons LW} \rho_{RW} + 1 \right) \right) F_{A,Rd \to LW,RW} F_{LW,RW \to A,Rd}$$

$$C_{31} = 1 - F_{Rd \rightleftharpoons A}^2 \rho_A \rho_{Rd} \qquad \text{Eq. 3-25}$$

$$C_3 = F_{LW,RW \to A,Rd} F_{A,Rd \to LW,RW} \left(2F_{Rd \rightleftharpoons A} \rho_A \rho_{Rd} + \rho_{Rd} + \rho_A \right) \qquad \text{Eq. 3-26}$$

$$C_{32} = F_{RW \rightleftharpoons LW} C_{31} + C_3 \qquad \text{Eq. 3-27}$$

$$C_4 = F_{A,Rd \to LW,RW} \left(\left(F_{Rd \rightleftharpoons A} \rho_A + 1 \right) \varepsilon_{Rd} B(LST_{Rd}) + \left(F_{Rd \rightleftharpoons A} \rho_{Rd} + 1 \right) L^{\downarrow} \right) \qquad \text{Eq. 3-28}$$

Please note that these solutions contain all the energy exchanges inside the street canyon including the entire multiple reflections. However, they are still complex. Considering that the items regarding to the radiation that having been reflected more than once would add only a negligible contribution to the observed signals, it is reasonable to ignore them to simplify the analytical model.

In addition, if the emissivities of the left and right walls are assumed to be the same, i.e., $\varepsilon_{LW} = \varepsilon_{RW} = \varepsilon_{wall}$, then $L_{Rd}^{Gnd\_3D}$, $L_{A}^{Gnd\_3D}$, $L_{LW}^{Gnd\_3D}$, $L_{RW}^{Gnd\_3D}$ in Eq. 3-19 could be simplified further after complex mathematical derivation as follows:

$$
\begin{bmatrix} L_{Rd}^{Gnd\_3D} \\[2mm] L_{A}^{Gnd\_3D} \\[2mm] L_{LW}^{Gnd\_3D} \\[2mm] L_{RW}^{Gnd\_3D} \end{bmatrix} = \begin{bmatrix} \varepsilon_{Rd}B(LST_{Rd}) + \dfrac{\rho_{Rd}H \cdot F_{LW\rightarrow Rd}\varepsilon_{wall}B(LST_{LW})}{W(1-F_{RW\rightleftharpoons LW}\rho_{wall})} + \dfrac{\rho_{Rd}H \cdot F_{RW\rightarrow Rd}\varepsilon_{wall}B(LST_{RW})}{W(1-F_{RW\rightleftharpoons LW}\rho_{wall})} + \dfrac{\rho_{Rd}F_{A\rightarrow Rd}L^{\downarrow}}{1-F_{RW\rightleftharpoons LW}\rho_{wall}} \\[4mm] L^{\downarrow} + \dfrac{\rho_{A}H \cdot F_{LW\rightarrow A}\varepsilon_{wall}B(LST_{LW})}{W(1-F_{RW\rightleftharpoons LW}\rho_{wall})} + \dfrac{\rho_{A}H \cdot F_{RW\rightarrow A}\varepsilon_{wall}B(LST_{RW})}{W(1-F_{RW\rightleftharpoons LW}\rho_{wall})} + \dfrac{\rho_{A}F_{Rd\rightarrow A}\varepsilon_{Rd}B(LST_{Rd})}{1-F_{RW\rightleftharpoons LW}\rho_{wall}} \\[4mm] \varepsilon_{wall}B(LST_{LW}) + \dfrac{\rho_{wall}W \cdot F_{A\rightarrow LW}L^{\downarrow}}{H(1-F_{RW\rightleftharpoons LW}\rho_{wall})} + \rho_{wall}F_{RW\rightarrow LW}\varepsilon_{wall}B(LST_{RW}) + \dfrac{\rho_{wall}W \cdot F_{Rd\rightarrow LW}\varepsilon_{Rd}B(LST_{Rd})}{H(1-F_{RW\rightleftharpoons LW}\rho_{wall})} \\[4mm] \varepsilon_{wall}B(LST_{RW}) + \dfrac{\rho_{wall}W \cdot F_{A\rightarrow RW}L^{\downarrow}}{H(1-F_{RW\rightleftharpoons LW}\rho_{wall})} + \rho_{wall}F_{LW\rightarrow RW}\varepsilon_{wall}B(LST_{LW}) + \dfrac{\rho_{wall}W \cdot F_{Rd\rightarrow RW}\varepsilon_{Rd}B(LST_{Rd})}{H(1-F_{RW\rightleftharpoons LW}\rho_{wall})} \end{bmatrix} \qquad \text{Eq. 3-29}
$$

where $\rho_{wall} = 1-\varepsilon_{wall}$, represents the reflectance of the wall, and $\rho_{Rd} = 1-\varepsilon_{Rd}$ represents the reflectance of the road.

After simplification, each analytical solution in Eq. 3-29 consists of four parts with specific physical meanings. Taking $L_{Rd}^{Gnd\_3D}$ as an example, the term $\varepsilon_{Rd}B(LST_{Rd})$ on the right side of the equation represents the radiation from the road itself. The second term, $\dfrac{\rho_{Rd}H \cdot F_{LW\rightarrow Rd}\varepsilon_{wall}B(LST_{LW})}{W(1-F_{RW\rightleftharpoons LW}\rho_{wall})}$, represents the radiation that is emitted by the left wall, then

reaches the road surface and is reflected by the road into the sensor. To be specific, two radiative transfer processes are included in this term: (a) the left wall-emitted radiation reaches the road surface directly, then is reflected by the road; (b) the left wall-emitted radiation is firstly reflected between the two walls for multiple times, then reaches the road surface and is reflected by the road. The physical meanings of the third term $\dfrac{\rho_{Rd}H \cdot F_{RW\rightarrow Rd}\varepsilon_{wall}B(LST_{RW})}{W(1-F_{RW\rightleftharpoons LW}\rho_{wall})}$ and the fourth term $\dfrac{\rho_{Rd}F_{A\rightarrow Rd}L^{\downarrow}}{1-F_{RW\rightleftharpoons LW}\rho_{wall}}$ are similar to the

second term but are regarding to the radiation emitted by the right wall and atmosphere, respectively. Besides, the remaining three analytical solutions ($L_{A}^{Gnd\_3D}$, $L_{LW}^{Gnd\_3D}$, and $L_{RW}^{Gnd\_3D}$) can also be interpreted similarly.

Provided that the road width, wall height, temperature and emissivity of road and wall, atmospheric spherical albedo at the bottom of the atmosphere, and the atmospheric downwelling radiance are known in advance, the radiance of each component inside the street canyon with the impact of 3-D structures and their radiation can be obtained using Eq. 3-29 easily. Consequently, the ground observed radiance (L^{Gnd_3D}) and brightness temperature (T^{Gnd_3D}) of the target pixel over a street canyon affected by the 3-D structures and their radiation can be simplified in Eq. 3-30, whereas the satellite observed radiance (L^{TOA_3D}) and brightness temperature (T^{TOA_3D}) of the target pixel over a street canyon influenced by the 3-D structures and their radiation can also be simplified in Eq. 3-31.

$$L^{Gnd\_3D} = B(T^{Gnd\_3D}) = \boldsymbol{M} \cdot \boldsymbol{N}$$

<div align="right">Eq. 3-30</div>

$$L^{TOA\_3D} = B(T^{TOA\_3D}) = \tau(\theta)\left(\boldsymbol{M} \cdot \boldsymbol{N}\right) + L^{\uparrow}(\theta)$$

<div align="right">Eq. 3-31</div>

in which

$$\boldsymbol{M} = \begin{bmatrix} \dfrac{\Omega_{roof}}{\Omega_{IFOV}} & \dfrac{\Omega_{road}}{\Omega_{IFOV}} & \dfrac{\Omega_{wall}}{\Omega_{IFOV}} \end{bmatrix}$$

<div align="right">Eq. 3-32</div>

$$\boldsymbol{N} = \begin{bmatrix} \varepsilon_{roof} B\left(LST_{roof}\right) + \left(1\text{-}\varepsilon_{roof}\right)L^{\downarrow} \\[2ex] \varepsilon_{Rd} B\left(LST_{Rd}\right) + \dfrac{\rho_{Rd} H \cdot F_{LW \to Rd}\varepsilon_{wall} B\left(LST_{LW}\right)}{W\left(1 - F_{RW \rightleftharpoons LW}\rho_{wall}\right)} + \dfrac{\rho_{Rd} H \cdot F_{RW \to Rd}\varepsilon_{wall} B\left(LST_{RW}\right)}{W\left(1 - F_{RW \rightleftharpoons LW}\rho_{wall}\right)} + \dfrac{\rho_{Rd} F_{A \to Rd} L^{\downarrow}}{1 - F_{RW \rightleftharpoons LW}\rho_{wall}} \\[2ex] \varepsilon_{wall} B\left(LST_{wall\_x}\right) + \dfrac{\rho_{wall} W \cdot F_{A \to wall\_x} L^{\downarrow}}{H\left(1 - F_{RW \rightleftharpoons LW}\rho_{wall}\right)} + \rho_{wall} F_{wall\_y \to wall\_x}\varepsilon_{wall} B\left(LST_{wall\_y}\right) + \dfrac{\rho_{wall} W \cdot F_{Rd \to wall\_x}\varepsilon_{Rd} B\left(LST_{Rd}\right)}{H\left(1 - F_{RW \rightleftharpoons LW}\rho_{wall}\right)} \end{bmatrix}$$

<div align="right">Eq. 3-33</div>

The subscripts "*wall_x*" and "*wall_y*" in Eq. 3-33 identify the left wall or right wall, which are dependent on the viewing angles because only one building wall could be observed by the remote sensor given a specific viewing direction as stated in Section 3.2.1. According to Eq. 3-29, the "*wall_x*" should be "*LW*" and "*wall_y*" should be "*RW*" if the left wall is inside the sensor's IFOV; while the "*wall_x*" should be "*RW*" and "*wall_y*" should be "*LW*" if the right wall is inside the sensor's IFOV.

Finally, the ATIMOU can be successfully developed on the basis of the solutions of $L_{Rd}^{Gnd\_3D}$, $L_{A}^{Gnd\_3D}$, $L_{LW}^{Gnd\_3D}$, and $L_{RW}^{Gnd\_3D}$. In fact, three options have been provided to calculate these four parameters. First, on the basis of Eq. 3-11, which is in matrix form, but provides the most accurate solutions and requires the least assumptions. Second, on the basis of Eq. 3-19, which is in analytical form and includes the entire multiple reflections. Third, on the basis of Eq. 3-29, which is simplified from Eq. 3-19 assuming that the two walls have same emissivity, and the items regarding to the radiation that having been reflected more than once are negligible. Considering that the third option gives the simplest solutions with acceptable accuracies for most cases, they have been used in the following sections to study the magnitude of the impact of 3-D structures and their radiation under different conditions. However, if more accurate results are required, particularly for situations in which facets have low emissivity inside a street canyon, more exact solutions given by Eq. 3-19 and Eq. 3-29 with entire multi-reflections should be used in ATIMOU. In addition, since the obstructions of solar irradiance inevitably exist in urban areas during the daytime of a cloudless day, the input *LST_LW*, *LST_RW*, and *LST_Rd* in ATIMOU then should be given as their effective temperature with consideration of the temperature difference in the sunlit and shadowed areas. In this way, the ATIMOU is applicable to both night-time and daytime conditions.

3.2.3. Qualification of the impact of 3-D structures and their radiation on TIR measurements over a street canyon

From the analysis above, the ground and satellite TIR measurements with consideration of the impact of 3-D structures and their radiation could be expressed by Eq. 3-30 and Eq. 3-31, respectively. If the 3-D structures are not considered, then ground and satellite TIR measurements irrespective of the impact of 3-D structures and their radiation could be expressed by Eq. 3-34 and Eq. 3-35, respectively, according to the traditional radiative transfer model.

$$L^{Gnd} = B(T^{Gnd}) = \boldsymbol{M} \cdot \boldsymbol{V}$$
<div align="right">Eq. 3-34</div>

$$L^{TOA} = B(T^{TOA}) = \tau(\theta)\left(\boldsymbol{M} \cdot \boldsymbol{V}\right) + L^{\uparrow}(\theta)$$
<div align="right">Eq. 3-35</div>

$$\boldsymbol{V} = \begin{bmatrix} \varepsilon_{roof} B\left(LST_{roof}\right) + \left(1 - \varepsilon_{roof}\right) L^{\downarrow} \\ \varepsilon_{Rd} B\left(LST_{Rd}\right) + \left(1 - \varepsilon_{Rd}\right) L^{\downarrow} \\ \varepsilon_{wall} B\left(LST_{wall\_x}\right) + \left(1 - \varepsilon_{wall}\right) L^{\downarrow} \end{bmatrix}$$
<div align="right">Eq. 3-36</div>

where L^{Gnd} and T^{Gnd} represent the ground observed radiance and brightness temperature of the target pixel over a street canyon, respectively, with L^{TOA} and T^{TOA} representing the satellite observed radiance and brightness temperature of target pixel over a street canyon, respectively, none of which take into account the impact of 3-D structures and their radiation. In this study, the magnitude of the impact of 3-D structures and their radiation on ground and satellite TIR measurements over a street canyon have been defined as Eq. 3-37 and Eq. 3-38, respectively.

$$\Delta T_{3D-2D}^{Gnd} = T^{Gnd\_3D} - T^{Gnd}$$
<div align="right">Eq. 3-37</div>

$$\Delta T_{3D-2D}^{TOA} = T^{TOA\_3D} - T^{TOA}$$
<div align="right">Eq. 3-38</div>

3.2.4. Qualification of the contribution of atmosphere and wall to ground TIR measurements over a road

If the target has been observed obliquely, the TIR measurement may be a mixed signal of roof, wall, and road. Under such cases, it is difficult to quantitively investigate the contribution of each radiation source to the total TIR measurements. Therefore, it is assumed that the target is to be observed vertically and the footprint of the IFOV is to be filled only with road in this section, suggesting $\frac{\Omega_{roof}}{\Omega_{IFOV}} = \frac{\Omega_{wall}}{\Omega_{IFOV}} = 0$ and $\frac{\Omega_{road}}{\Omega_{IFOV}} = 1$. Then,

Eq. 3-30 could be simplified further as:

$$L^{Gnd\_3D} = \varepsilon_{Rd} B(LST_{Rd}) + \frac{\rho_{Rd} H \cdot F_{LW \to Rd} \varepsilon_{wall} B(LST_{LW})}{W(1 - F_{RW \rightleftharpoons LW} \rho_{wall})}$$
$$+ \frac{\rho_{Rd} H \cdot F_{RW \to Rd} \varepsilon_{wall} B(LST_{RW})}{W(1 - F_{RW \rightleftharpoons LW} \rho_{wall})} + \frac{\rho_{Rd} F_{A \to Rd} L^{\downarrow}}{1 - F_{RW \rightleftharpoons LW} \rho_{wall}}$$

Eq. 3-39

Based on Eq. 3-39, the contribution of each radiation source inside the 3-D structures to the total ground TIR measurements over a road can be obtained. The contribution of atmosphere to the ground TIR measurements (ΔT_A^{OnRoad}) over a road can be expressed by:

$$\Delta T_A^{OnRoad} = B^{-1} \left[\varepsilon_{Rd} B(LST_{Rd}) + \frac{\rho_{Rd} F_{A \to Rd} L^{\downarrow}}{1 - F_{RW \rightleftharpoons LW} \rho_{wall}} \right] - B^{-1} \left[\varepsilon_{Rd} B(LST_{Rd}) \right]$$

Eq. 3-40

where B^{-1} is the inverse Planck function.

Similarly, the contribution of the two walls to the ground TIR measurements (ΔT_{wall}^{OnRoad}) over a road can be expressed by:

$$\Delta T_{wall}^{OnRoad} = B^{-1} \left[\varepsilon_{Rd} B(LST_{Rd}) + \frac{\rho_{Rd} H \cdot F_{LW \to Rd} \varepsilon_{wall} B(LST_{LW})}{W(1 - F_{RW \rightleftharpoons LW} \rho_{wall})} \right.$$
$$\left. + \frac{\rho_{Rd} H \cdot F_{RW \to Rd} \varepsilon_{wall} B(LST_{RW})}{W(1 - F_{RW \rightleftharpoons LW} \rho_{wall})} \right] - B^{-1} \left[\varepsilon_{Rd} B(LST_{Rd}) \right]$$

Eq. 3-41

3.3. Simulation results

3.3.1. Simulation inputs

To investigate the impact of 3-D structures and their radiation on the satellite TIR measurements, the geometric and radiative properties of the scenario are needed. From Eq. 3-30 – Eq. 3-33, it is shown that six parameters could affect the magnitude of satellite TIR measurement: atmospheric type, temperature and emissivity of building walls, temperature and emissivity of a road, and the ratio between wall height and road width (hereafter referred as "H/W"). Please note that the temperatures of left and right wall have been set to be the same during the analyses in the following sections for simplification (i.e. $LST_{LW} = LST_{RW} = LST_{wall}$), although they can be different in the proposed ATIMOU. Besides, since the building walls are assumed to have the same height, the energy exchange inside the street canyon will not be affected by the roof-emitted radiance. Therefore, the dependency of the impact of 3-D structures and their radiation on roof emissivity and temperature will not be discussed in this study. Additionally, simulated results at 10 μm

have been presented as an example because the results are similar in other TIR wavelengths. Aerosol type has been set as Urban with the visibility of 10 km and MODerate resolution atmospheric TRANsmission model (MODTRAN) (Berk et al., 2006; Berk et al., 2004) has been introduced to calculate the atmospheric transmittance, upwelling, downwelling radiance, and the atmospheric spherical albedo at bottom of atmosphere. The IFOV footprint is assumed to be filled only with road at nadir. A series of H/W is set to represent different street canyon structures. Besides, we have obtained the minimum, maximum, and mean emissivities at 10 μm for commonly used construction materials of roof, wall, and road respectively on the basis of the ECOSTRESS emissivity library (https://speclib.jpl.nasa.gov) to represent the emissivity variations in urban areas. When studying the dependency of the magnitude of 3-D structures and their radiation on a specific parameter, the rest arguments have been set as their mean value (tagged as the 'default' value in Table 3-1). Detailed configurations for simulation inputs are listed in Table 3-1.

Table 3-1. Simulation inputs for studying the magnitude of the impact of 3-D structures and their radiation on TIR measurements

Geometric properties		
H/W	0.5, 1.0, 2.0 (Default), 4.0	
Radiative properties		
	Emissivity (Min, Mean, Max)	Temperature (K)
Wall	0.415, 0.906 (Default), 0.967	260, 280, 300 (Default). 320, 340
Road	0.921, 0.950 (Default), 0.973	260, 280, 300 (Default). 320, 340
Roof	0.016, 0.813 (Default), 0.988	260, 280, 300 (Default). 320, 340
Atmospheric parameters		
Atmospheric type (Total water vapor content / bottom layer temperature)	Tropical (4.11 g/cm^2 / 300.15 K), Mid-Latitude Summer (2.92 g/cm^2 / 294.15 K), Mid-Latitude Winter (0.85 g/cm^2 / 272.15 K), 1976 US Standard (1.42 g/cm^2 / 288.15 K, Default)	
Viewing angles		
Zenith angle	0° ~ 50°	Azimuth angle 0° ~ 360°

3.3.2. Analysis of the impact of 3-D structures and their radiation on TIR measurements over a street canyon

According to Eq. 3-31 and Eq. 3-33, atmospheric transmittance, H/W, road reflectance, wall radiation, and viewing direction are the five main factors that exert the strongest

influence on the TIR measurements after considering the 3-D structures and their radiation in the radiative transfer model. Therefore, the influence of these first four parameters in function of view geometric conditions on the magnitude of the impact of 3-D structures and their radiation is further investigated using Eq. 3-30 – Eq. 3-38 in this section.

3.3.2.1. Dependency of the impact of 3-D structures and their radiation on atmospheric type

Four atmospheric types were used to represent different atmospheric conditions in this section. Using Eq. 3-38, the magnitude of the impact of 3-D structures and their radiation on satellite TIR measurement was considered for different atmospheric types (Fig. 3-3). Results are presented utilizing a polar coordinate system with color representing the magnitude of the impact of 3-D structures and their radiation, the length of radius representing the viewing zenith angle, and the radius angle representing the viewing azimuth angle. As the results show, the magnitude of the impact of 3-D structures and their radiation in a hot, humid atmosphere (e.g., Tropical with total water vapor content of 4.11 g/cm^2 and bottom layer temperature of 300.15 K) is about 0.52 K, which is much smaller than that in a cold and dry atmosphere (e.g., Mid-Latitude Winter with total water vapor content of 0.85 g/cm^2 and bottom layer temperature of 272.15 K) with a magnitude of about 1.78 K. In fact, the difference in the magnitude of the impact of 3-D structures and their radiation for different atmospheres is mainly caused by the variation of atmospheric transmittance. As the atmosphere becomes humid and hot, atmospheric transmittance decreases, indicating that the contribution of 3-D structures and their radiation will be suppressed in the satellite observed signals. This effect explains why the magnitude of the impact of 3-D structures and their radiation in cold and dry atmospheres is always larger than those in hot and humid atmospheres.

Additionally, for each atmospheric type, the impact of 3-D structures and their radiation decreases as viewing zenith angle increases, including the north-south direction. This is believed to be caused by the decrease of atmospheric transmittance with increasing view zenith angle. Moreover, around the west-east direction, IFOV may be partly or entirely filled with building roofs as the viewing zenith angle increases to a certain value. Consequently, with increasing zenith angle, the magnitude of the impact of 3-D structures and their radiation decreases faster towards the west-east direction than those around north-south direction, because the building roofs are not affected by the 3-D structures and their radiation.

Fig. 3-3. The magnitude of the impact of 3-D structures and their radiation on satellite TIR measurements over a street canyon for different atmospheric types on the basis of Eq. 3-31, Eq. 3-35, and Eq. 3-38. Additional required parameters have been set as the default values listed in Table 3-1.

3.3.2.2. Dependency of the impact of 3-D structures and their radiation on road emissivity

From Eq. 3-33, it is shown that H/W is a factor that governs the energy exchange inside the street canyon. Besides, road reflectance that directly multiplies the H/W is also an important parameter determining the simulated TIR measurements, especially for nadir observations. Moreover, road reflectance determines not only the amount of reflected environmental radiance, but also the self-emitted radiance of the road ($\varepsilon_{Rd} = 1 - \rho_{Rd}$). In this section, Eq. 3-37 is employed under different combinations of road emissivity and H/W to study the impact of 3-D structures and their radiation on ground TIR measurements (Fig. 3-4).

Results show that the impact of 3-D structures and their radiation increases with increasing H/W around the north-south direction. For example, when road emissivity is 0.921, the magnitude of the impact of 3-D structures and their radiation increases from about 1.44 K to 3.47 K as H/W increases from 0.5 to 4.0 (Fig. 3-4a, b, and c). However, as H/W increases from 0.5 to 2.0, the impact of 3-D structures and their radiation increases by about 1.54 K (from 1.44 K to 2.98 K). When H/W continually increases from 2.0 to 4.0, the impact of 3-D structures and their radiation only increases by about 0.49 K (from 2.98 K to 3.47 K), indicating the increasing rate of impact of 3-D structures and their radiation decreases as H/W continually increases. This is because the view factors from wall to road

first increase quickly with increasing H/W, then tend to become stable as they approach 0.5, suggesting that the possibility of energy leaving the wall and reaching the road tends to be stable with increasing H/W. Moreover, when H/W is large (e.g., H/W ≥ 2.0), for those cases with a viewing azimuth angle away from the north-south direction and viewing zenith angle larger than 20°, there will be no impact of 3-D structures and their radiation on the TIR measurement because the IFOV is only filled with building roofs. But when H/W is small (e.g., H/W = 0.5), the impact of 3-D structures and their radiation exists for all viewing angles.

Results also show that road emissivity significantly affects the magnitude of the impact of 3-D structures and their radiation. When road emissivity decreases from 0.973 to 0.921, the contribution from 3-D structures and their radiation to the TIR measurements increases by 0.96 K (from 0.48 K to 1.44 K) for the cases with H/W = 0.5, while could increase by 2.30 K (from 1.17 K to 3.47 K) for the cases with H/W=4.0. In fact, as the road emissivity decreases, the target reflected environmental radiance increases, leading to the proportion of the target reflected environmental radiance in the total TIR measurement increases directly. Besides, according to the Kirchoff's law, the road self-emitted radiance decreases at the same time, which could also indirectly result in the increase of the proportion of the target reflected environmental radiance in the total TIR measurement. Therefore, the magnitude of the impact of 3-D structures and their radiation is very sensitive to the road emissivity.
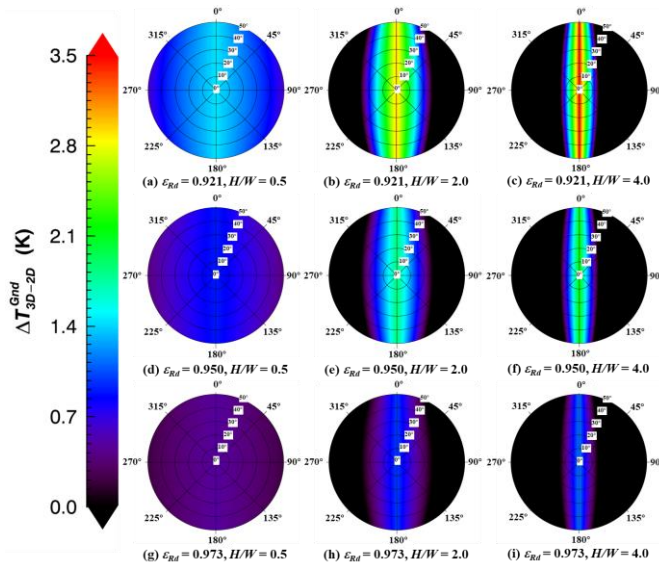
Fig. 3-4. The magnitude of the impact of 3-D structures and their radiation on ground TIR measurements over a street canyon under different combinations of road emissivity and H/W on the basis of Eq. 3-30, Eq. 3-34, and Eq. 3-37. Additional parameters have been set as the default values listed in Table 3-1.

3.3.2.3. Dependency of the impact of 3-D structures and their radiation on wall temperature

For nadir observations, the larger the radiation of the building walls, the larger the impact of 3-D structures and their radiation on the observed TIR measurements, provided that the other parameters remain unchanged. In fact, both wall temperature and wall emissivity determine the radiation emitted by building walls, but the magnitude of the impact of 3-D structures and their radiation is more sensitive to the wall temperature than that to the wall emissivity. As shown in Eq. 3-33, self-radiation of a wall increases with increasing wall emissivity (i.e., the numerator of $\dfrac{\rho_{Rd} H \cdot F_{LW \to Rd} \varepsilon_{wall} B(LST_{LW})}{W(1 - F_{RW \rightleftharpoons LW} \rho_{wall})} + \dfrac{\rho_{Rd} H \cdot F_{RW \to Rd} \varepsilon_{wall} B(LST_{RW})}{W(1 - F_{RW \rightleftharpoons LW} \rho_{wall})}$ increases). But the denominator increases as well, which counteracts the increases in the numerator. In addition, the contribution of the atmosphere (i.e., $\dfrac{\rho_{Rd} F_{A \to Rd} L^{\downarrow}}{1 - F_{RW \rightleftharpoons LW} \rho_{wall}}$) also decreases, counteracting the increases in the wall's self-radiation as well. However, as the wall temperature increases, the denominator and the contribution of the atmosphere both remain unchanged which do not counteract the increases of the wall's self-radiation. Consequently, the magnitude of the impact of 3-D structures and their radiation is more dependent on the wall temperature than the wall emissivity, which is also confirmed by the results presented in Section 3.3.3.1 below. Therefore, only wall temperature has been changed to represent the differing radiation magnitude of building walls in this section. Using Eq. 3-37, the impact of 3-D structures and their radiation on ground TIR measurement is considered under different combinations of wall temperature and H/W (Fig. 3-5).

In Fig. 3-5, it can be seen that the magnitude of the impact of 3-D structures and their radiation on the TIR measurement increases with increasing wall temperature. For cases of nadir observations, as wall temperature increases from 260 K to 340 K, the magnitude of the impact of 3-D structures and their radiation increases from about 0.31 K to about 1.75 K if H/W is 0.5. When H/W increases to 4.0, there will be a more significant impact of 3-D structures and their radiation on the TIR measurement, with the magnitude increasing from 0.77 K to 4.21 K. The magnitude of the impact of 3-D structures and their radiation seems to be more affected by wall temperature than by road emissivity when compared with Fig. 3-4. The possible reason is that the term $\dfrac{\rho_{Rd} H \cdot F_{LW \to Rd} \varepsilon_{wall} B(LST_{LW})}{W(1 - F_{RW \rightleftharpoons LW} \rho_{wall})} + \dfrac{\rho_{Rd} H \cdot F_{RW \to Rd} \varepsilon_{wall} B(LST_{RW})}{W(1 - F_{RW \rightleftharpoons LW} \rho_{wall})}$ from Eq. 3-33 is the main influence on the magnitude of the impact of 3-D structures and their radiation. Provided that the other

parameters remain unchanged except ρ_{Rd} and LST_{wall}, it is shown that ρ_{Rd} in Fig. 3-4 has changed from 0.050 to 0.079 and 0.027, respectively, i.e., representing 58% and 46% of the variation in road reflectance, whereas LST_{wall} has changed from 300 K to 340 K and 260 K, respectively, i.e., 77% and 53% of the variation exhibited by wall radiance, which is larger than the variation of ρ_{Rd} in Fig. 3-4. Thus, the magnitude of the impact of 3-D structures and their radiation is smaller with decreasing road emissivity from 0.973 to 0.921 (Fig. 3-4) than that with increasing wall temperature from 260 K to 340 K (Fig. 3-5).
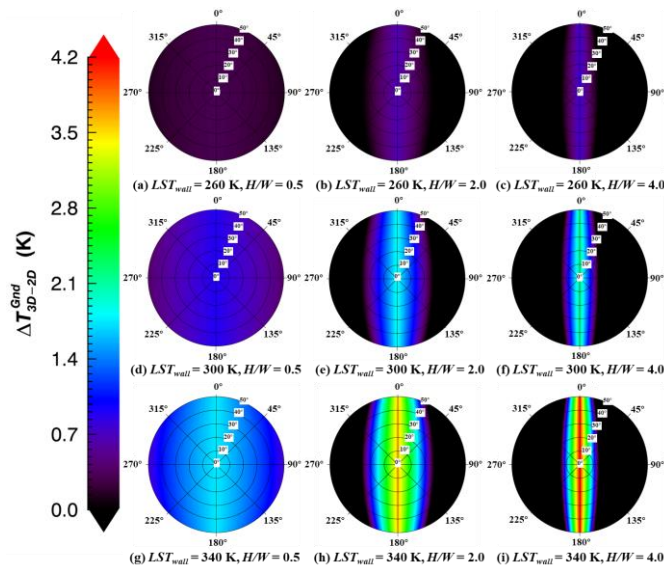
Fig. 3-5. The magnitude of the impact of 3-D structures and their radiation on ground TIR measurements over a street canyon under different combinations of wall temperature and H/W on the basis of Eq. 3-30, Eq. 3-34, and Eq. 3-37. The temperatures of left and right wall have been set to be the same for simplification (i.e. $LST_{LW}=LST_{RW}=LST_{wall}$). Additional parameters have been set as the default values listed in Table 3-1.

3.3.2.4. The impact of 3-D structures and their radiation on TIR measurements for extreme cases

According to the simulated results above, there generally exists non-negligible impact of 3-D structures and their radiation on the ground TIR measurements for typical street canyons. The magnitude of this impact may be even larger for extreme cases, such as the street canyons regarding to a warm road reflected by a low-emissivity wall and a hot wall reflected by a low-emissivity road. In this section, the results of these two scenarios have also been simulated in detail (Fig. 3-6). It should be noticed that the minimum emissivity

of road has been set as 0.415 in Fig. 3-6b (i.e. the same as the minimum emissivity of wall), because the typical minimum emissivity of road according to the ECOSTRESS emissivity library (i.e. 0.921) is too high to represent the extreme condition. The H/W has been set as 1.0 and the width of the IFOV has been set as three times as the road width to allow a better capture of the signals from walls for oblique viewing angles.

As shown in Fig. 3-6a, the magnitude of the impact of 3-D structures and their radiation is only about 0.12 K for nadir observations. This is because the road emissivity is high (0.973), indicating less environmental radiance could be reflected. Moreover, the wall emissivity is low (0.415), leading to less environmental radiance arriving at the road. However, as viewing zenith angle increases, the proportion of the wall inside the IFOV increases. The radiance from a warm road will be reflected by a low-emissivity wall. Therefore, the impact of 3-D structures and their radiation on TIR measurements increases quickly to 9.91 K. As the viewing zenith angle continually increases, the proportion of roof inside the IFOV increases while the proportion of wall decreases. Thus, the impact of 3-D structures and their radiation on TIR measurements decreases as shown in Fig. 3-6a.

For the case regarding to a hot wall reflected by a low-emissivity road as shown in Fig. 3-6b, the impact of 3-D structures and their radiation is maximum for nadir observations with the magnitude of 12.30 K. As the viewing zenith angel increases, the proportion of road decreases while the proportion of wall and roof increases inside the IFOV. But less environmental radiance could be reflected by wall because of the high emissivity of wall and the low emissivity of road, leading to the impact of 3-D structures and their radiation decreases. It is predictable that there will be no impact of 3-D structures and their radiation on the TIR measurements if the viewing zenith angle is large enough to make the IFOV entirely fulfilled by roof.
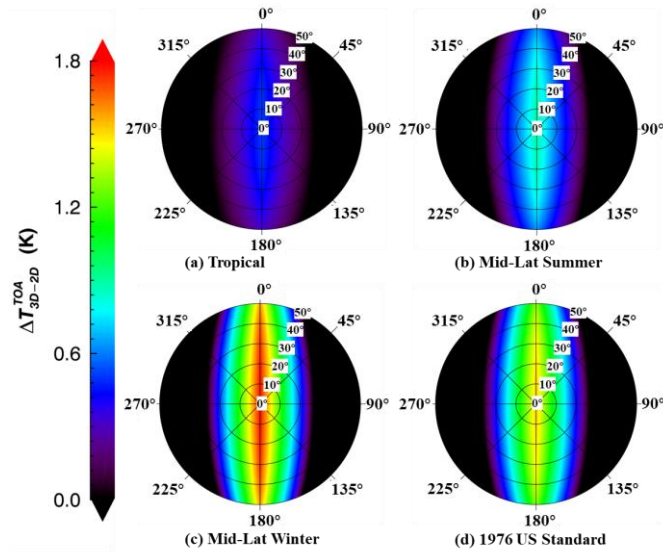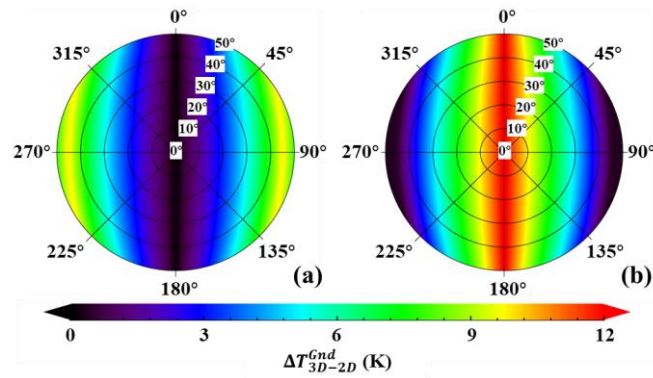
Fig. 3-6. The magnitude of the impact of 3-D structures and their radiation on ground TIR measurements over a street canyon under two extreme scenarios. The temperatures of left and right wall have been set to be the same for simplification (i.e. $LST_{LW} = LST_{RW} = LST_{wall}$). (a) $\varepsilon_{wall} = 0.415$, $LST_{wall} = 300\ K$, $\varepsilon_{Rd} = 0.973$, and $LST_{Rd} = 340\ K$; (b) $\varepsilon_{wall} = 0.967$, $LST_{wall} = 340\ K$, $\varepsilon_{Rd} = 0.415$, and $LST_{Rd} = 300\ K$. The H/W has been set as 1.0 and the width of the IFOV has been set as three times as the road width. Additional parameters have been set as the default values listed in Table 3-1.

3.3.3. Analysis of the contribution of atmosphere and wall to total ground TIR measurements over a road

The separate contribution of atmosphere and wall to the total ground TIR measurements is also worthy of study. Assuming the target has been observed vertically and the IFOV footprint is filled only with road, the contribution of atmosphere and building wall to the total ground TIR measurements over a road can be studied in detail using Eq. 3-40 and Eq. 3-41, respectively.

3.3.3.1. Dependency of the contribution of atmosphere and wall to total ground TIR measurements with variable wall temperature and wall emissivity

When 3-D structures in urban areas are considered, the building walls together with atmospheric downwelling radiance are expected to contribute to the environmental radiance above the road. As the wall temperature and emissivity increase, more energy is emitted from the building walls, provided that the other input parameters remain unchanged (Fig. 3-7). Consequently, the environmental radiance reflected by a road increases as well. But according to Eq. 3-40, the contribution of atmosphere to the TIR measurements would not change with variation of wall temperature (Fig. 3-7). In addition, as shown in Fig. 3-7, the contribution of atmosphere is also not sensitive to the wall emissivity. Furthermore, the magnitude of the contribution of atmosphere to total TIR measurements is small. For example, when H/W is 2.0, the magnitude is only about 0.22 K for all combinations of wall temperature and emissivity.

Moreover, although the self-emitted radiance of a wall decreases as wall emissivity decreases, more environmental radiance will be reflected by the wall simultaneously. Therefore, the contribution from building walls does not change considerably with slight variation of wall emissivity (e.g. from 0.967 to 0.906) as shown in Fig. 3-7. Only if the wall emissivity changes greatly (e.g. from 0.906 to 0.415), the contribution of a building wall would significantly affect the total ground TIR measurements. However, increasing wall temperature could significantly increase the contribution of building walls. For example, as wall temperature rises from 260 K to 340 K, the magnitude of the contribution of the building wall could increase from about 1.14 K to 4.22 K for cases with H/W of 2.0 and wall emissivity of 0.967.
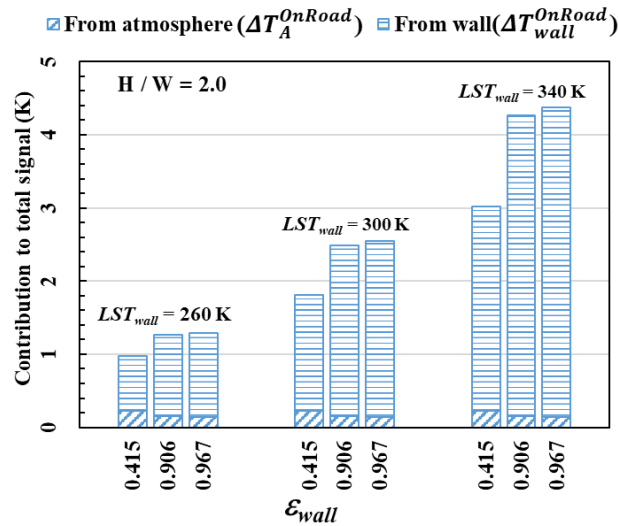
Fig. 3-7. Respective contributions of atmosphere and building wall to total ground TIR measurements with variation of wall temperature and wall emissivity. The temperatures of left and right wall have been set to be the same for simplification (i.e. $LST_{LW}=LST_{RW}=LST_{wall}$). Additional parameters have been set as the default values listed in Table 3-1.

3.3.3.2. Dependency of the contribution of atmosphere and wall to total ground TIR measurement with variable road temperature and road emissivity

The value of road emissivity determines how much environmental radiance could be reflected into the remote sensor. Unlike natural surfaces, the emissivity of manmade materials generally has a large range, implying the reflectivity may be high in urban areas. For example, the emissivity of paving materials such as concrete and asphalt can be < 0.95 at 10 μm according to the ECOSTRESS Spectral Library, Version 1.0 (https://speclib.jpl.nasa.gov/). As a result, large environmental radiance could be reflected making the contribution of building wall to total ground TIR measurement significant. As

shown in Fig. 3-8, the contribution of a building wall is < 2.0 K when road emissivity is 0.973, but quickly increases by about 3 times as road emissivity decreases to 0.921.

Moreover, results show that the contribution of a building wall increases with decreasing road temperature. In fact, the absolute value of road-reflected environmental radiance remains the same with varying road temperature, according to Eq. 3-41. However, the self-emitted radiance of a road decreases as road temperature decreases, making the proportion of road-reflected environmental radiance in the total TIR measurements relatively increase. Consequently, the contribution of a building wall and atmosphere to the total TIR measurements both increase with decreasing road temperature. For example, when H/W is 2.0 and road temperature decreases from 340 K to 260 K, the contribution of a building wall increases from 2.71 K to 5.89 K for cases with road emissivity of 0.921, whereas the contribution of atmosphere increases from 0.18 K to 0.39 K. If road emissivity increases to 0.973, the contribution of a building wall could only increase from 0.90 K to 1.97 K and the contribution of the atmosphere is almost negligible at a magnitude of < 0.13 K. It is shown that the atmosphere does not make significant contribution to the total TIR measurements for the cases above. But if the road emissivity is low, such as 0.415 (the same as the minimum wall emissivity used in this study), the magnitude of the atmospheric contribution increases significantly to 2.92 K with the other parameters setting as the default values listed in Table 3-1.
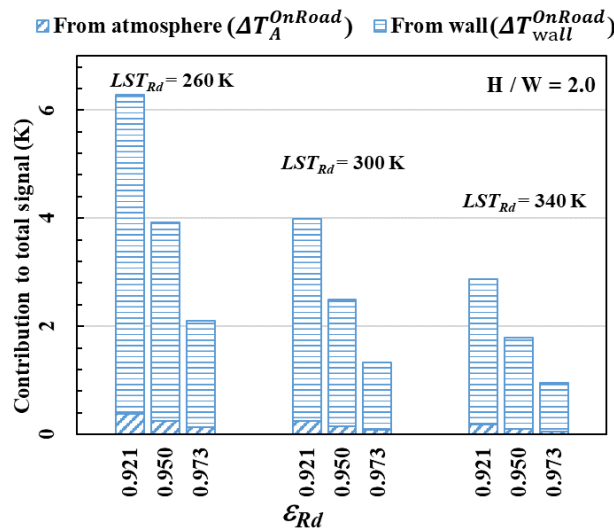
Fig. 3-8. Respective contributions of atmosphere and building wall to total ground TIR measurements with variation of road temperature and road emissivity. Additional parameters have been set as the default values listed in Table 3-1.

3.4. Comparison with other models

As demonstrated in Section 3.2.2, once the energy exchange inside a street canyon has been calculated, the traditional TIR radiative transfer model could be used to obtain the satellite observed radiance of a target pixel in ATIMOU. Hence, the key procedure of the proposed model is the calculation of ground brightness temperature (T_g). Validation of ATIMOU could be achieved by comparing the simulated T_g with referenced values.

An additional 3-D radiative transfer model has been introduced in this study for intercomparison. Considering that the DART model is one of the most commonly used 3-D radiative transfer models in use and has the ability of simulating radiative transfer in the system "Earth-Atmosphere" from visible to thermal infrared wavelengths (Gastellu-Etchegorry et al., 2004; Gastellu-Etchegorry et al., 2015; Guillevic and Gastellu-Etchegorry, 2003), it has been chosen to provide the reference T_g (tagged as DART hereafter). In DART, an Earth scene with the total size of 50 m * 50 m and a cell dimension of 0.5 m * 0.5 m * 0.5 m has been introduced to contain the scenario shown in Fig. 3-1.. The type of roof has been set as plate without thickness. The surfaces of urban element in DART have been set to have no spatial variability in emissivities and temperatures. The road width, wall height, and other parameters have been set according to the preset values listed in Table 3-1. Then, the scenario of the whole urban area could be generated by repeating this basic Earth scene. Considering the IFOV may be covered with hundreds of cells, the TIR measurements of all the cells inside the IFOV will be averaged to obtain the final simulated results.

In addition, the analytical model proposed by Caselles and Sobrino (Caselles and Sobrino, 1989) (tagged as Caselles_1989 hereafter) has also been applied to urban areas to provide the simulated results for inetercomparison. Besides, to study the bias introduced by simplifying Eq. 3-19 to Eq. 3-29, the simulated results of ATIMOU using the exact solutions of Eq. 3-19 have also been provided (tagged as ATIMOU_Exact hereafter). Since road emissivity, H/W, wall temperature, and road temperature are the main factors that affect the contribution of 3-D structures and their radiation to total TIR measurements, the simulated T_g using different models has been compared with each other by varying these factors under nadir (Fig. 3-9a ~ Fig. 3-9e) and non-nadir conditions (Fig. 3-9f). Besides, since the roof and wall are supposed to be the same component in Caselles_1989, the roof emissivity has been set as the same as the wall emissivity during the comparison of the four models in this section.

For all the cases, it is shown in Fig. 3-9 that the simulations from ATIMOU_Exact are the closest to DART while the simulations from Caselles_1989 are the most different from DART. The ATIMOU almost provides the same results as the ATIMOU_Exact with the biases of only about 0.05 K. However, as the road emissivity or wall emissivity decreases, the ATIMOU underestimates the T_g comparing with ATIMOU_Exact because of the simplification made in Section 3.2.2, leading to the simulations from ATIMOU less than DART. For example, when all parameters have been set as default values except that road emissivity decreases from 0.973 to 0.921, the difference between ATIMOU and DART increases from 0.02 K to 0.07 K (Fig. 3-9c), which is still acceptable. But if wall emissivity decreases from 0.967 to 0.415 while the other parameters remain as the default values, the difference between ATIMOU and DART increases quickly from 0.01 K to 0.50 K (Fig. 3-9e). As a contrast, the difference between ATIMOU_Exact and DART never exceeds 0.02 K except the one with the wall emissivity of 0.415 (Fig. 3-9e), for which the difference is still not large with the magnitude of 0.08 K.

When comparing ATIMOU with Caselles_1989, the difference is small only if the emissivities of each component inside the street canyon are not too low and the temperatures of each component are close to each other. For example, as shown in Fig. 3-9b the difference between ATIMOU and Caselles_1989 is only around 0.1 K when the road temperature is 300 K and the other parameters have been set as default values. As the road temperature decreases away from 300 K to 260 K, the difference between ATIMOU and Caselles_1989 soon increases to 0.53 K. Besides, when the road temperature increases away from 300 K to 340 K, this difference also increases to a larger magnitude (0.26 K). When the other parameters have been set as the default values but the wall temperature varies from 300 K to 260 K or 340 K, the difference between ATIMOU and Caselles_1989 also increases quickly to 0.28 K and 0.45 K, respectively (Fig. 3-9d). This is because Caselles_1989 introduces the first-order Taylor expansion to linearize the Planck function, which maybe not accurate when the temperatures of each component inside the street canyon is not close to the effective temperature. It is also shown that the difference between ATIMOU and Caselles_1989 becomes large when road emissivity or wall emissivity decreases. As shown in Fig. 3-9c and Fig. 3-9e, this difference increases from 0.05 K to 0.15 K as road emissivity decreases from 0.973 to 0.921, while increases from 0.03 K to 0.35 K as wall emissivity decreases from 0.967 to 0.415. This phenomenon is because all the multi-reflections have been ignored in Caselles_1989 but some of the multi-reflections has been retained in ATIMOU owing to the "gain factor - $\left(1 - F_{RW \rightleftharpoons LW} \rho_{wall}\right)$" in the

denominator.

The simulated results of these four models under non-nadir conditions have also been compared as shown in Fig. 3-9f. The azimuth angel has been set as 90° which is perpendicular to the street direction and zenith angles of 0°, 10°, 20°, 30°, 40°, and 50° have been used as examples. It is shown that the ATIMOU_Exact is still the closest to DART while the Caselles_1989 is the most different from DART. The simulations from the ATIMOU, ATIMOU_Exact, and Caselles_1989 are generally similar to each other, but the differences between them and DART increase a little as viewing zenith angle increases. This is perhaps because that the street canyon has been discretized in DART, indicating there may exist variations among the small voxels that constitute the wall or road after calculating the multi-reflections inside the street canyon. When the viewing zenith angle increases, the scenario inside the IFOV changes resulting from the obstruction of buildings. The simulations of DART vary not only because the proportion of each component inside the IFOV changes, but also because the voxels regarding to each component inside the IFOV are different. However, the surfaces of the wall and road are all considered as Lambert plates in the rest three models, indicating the simulations of these three models vary only because the proportion of each component inside the IFOV changes. Consequently, the difference between DART and the rest three models increases a little with increase of viewing zenith angle. However, if the viewing zenith angle continually increases, only roof could be observed inside the IFOV, leading to the simulated results of the four models are all the same (Fig. 3-9f).

Moreover, to provide an overall comparison between these four models, a series of scenarios have been made to represent different street canyons with varying the H/W, ε_{wall}, LST_{wall}, ε_{Rd}, and LST_{Rd} according to the preset parameters in Table 3-1. The other parameters have been set as default values and the viewing direction has been set as nadir. Then, the minimum, mean, and maximum absolute differences between any two of the models have been calculated and listed in Table 3-2 on the basis of these scenarios. It is shown that ATIMOU_Exact and DART provide the most similar simulations while Caselles_1989 and DART provide the most different simulations.
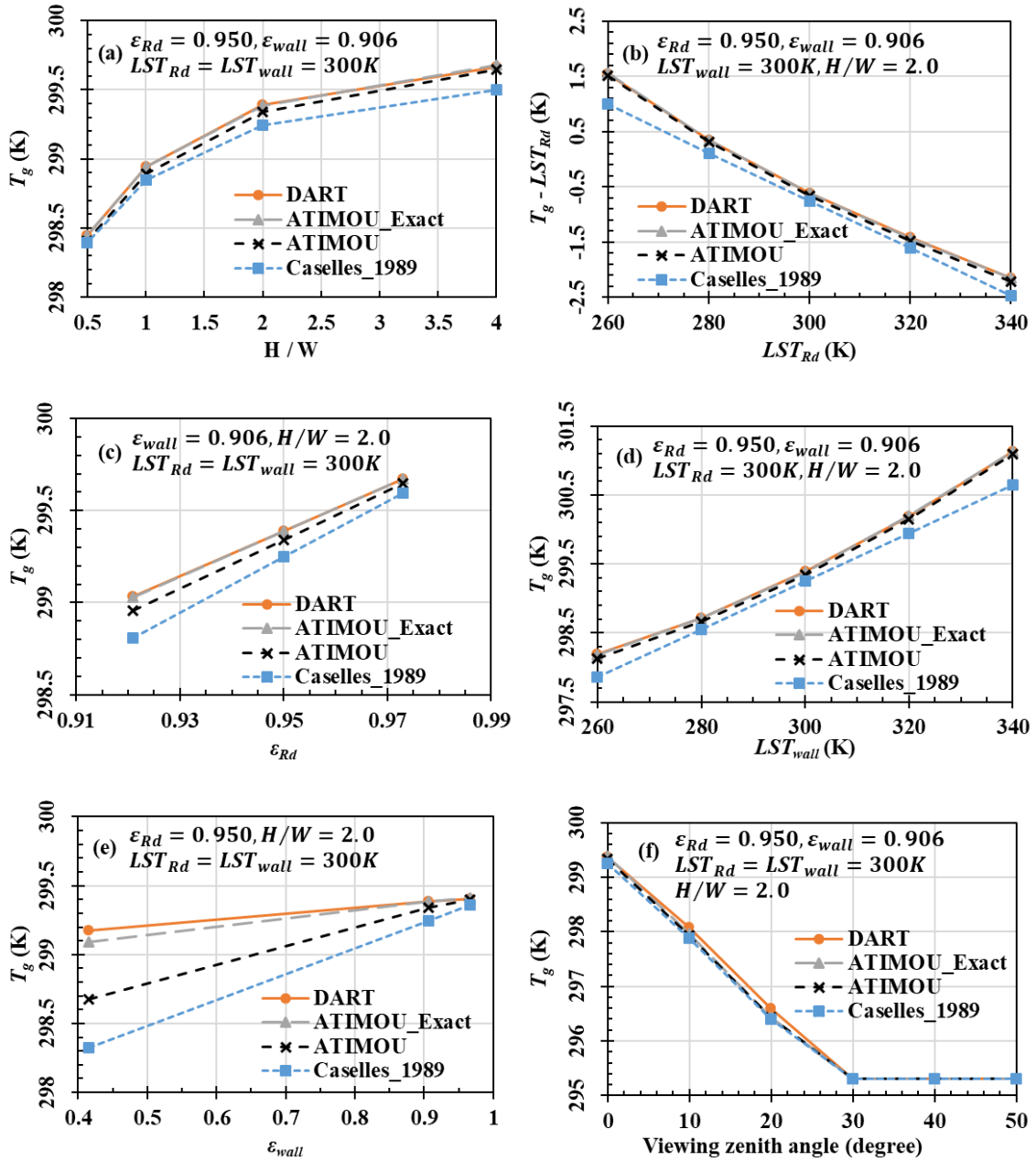
Fig. 3-9. The intercomparison between the simulated ground brightness temperature (T_g) of the DART, ATIMOU_Exact, ATIMOU, and Caselles_1989 models. The temperatures of left and right wall have been set to be the same for simplification (i.e. $LST_{LW} = LST_{RW} = LST_{wall}$). For (a) ~ (e), the IFOV is assumed to only be filled by road, viewing zenith and azimuth angles are fixed at 0°. For (f), the viewing zenith angle varies from 0° to 50° and the azimuth angle is fixed at 90°.

Table 3-2. The Minimum/Mean/Maximum absolute difference of the simulated ground brightness temperature (T_g) between any two of the models.

	DART	ATIMOU_Exact	ATIMOU	Caselles_1989
DART	-	0.00 K/0.02 K/0.17K	0.00 K/0.10 K/0.50 K	0.02 K/0.32 K/1.93 K
ATIMOU_Exact	-	-	0.01 K/0.09 K/0.42 K	0.02 K/0.31 K/1.87 K
ATIMOU	-	-	-	0.00 K/0.22 K/1.55 K
Caselles_1989	-	-	-	-

3.5. Discussion and conclusion

In this study, a new analytical TIR radiative transfer model, ATIMOU, was introduced that considers the impact of 3-D structures and their radiation on TIR measurements. In this model, viewing factors between a road and its surrounding infrastructure were used to calculate the energy exchange inside a street canyon. On the basis of this model, the impact of 3-D structures and their radiation on the TIR measurements over a street canyon was quantitively evaluated under different viewing angles after accounting for obstructions caused by walls of buildings. The respective contributions of the atmosphere and walls to total ground TIR measurements at nadir were also investigated to further characterize the impact of 3-D structures and their radiation. Finally, the fidelity of the proposed model was tested by a comparison with the DART model. Small mean absolute error < 0.10 K was found in the simulated ground brightness temperatures, indicating that the proposed model is in good agreement with DART.

For the simulations over a street canyon, results show that the magnitude of the impact of 3-D structures and their radiation on satellite TIR measurements is different under different atmospheric types. Generally, the magnitude of the impact of 3-D structures and their radiation in a hot, humid atmosphere is smaller than that in a cold, dry atmosphere, and is believed to be caused by the variation of atmospheric transmittance as demonstrated by Eq. 3-31 and Eq. 3-35. Results also show that the impact of 3-D structures and their radiation is always largest at nadir, because the IFOV may be partly, and even entirely, filled with building roofs as the viewing zenith angle increases. However, the building roofs are not affected by the radiation of the 3-D structures. Moreover, increasing H/W, decreasing road emissivity, and increasing wall temperature could all increase the magnitude of the impact of 3-D structures and their radiation on a TIR measurement, according to the simulations. For nadir observations of a scenario with a wavelength of 10

μm, road and wall temperatures of 300 K, road emissivity of 0.950, and wall emissivity of 0.906, as H/W increases from 0.5 to 4.0, the impact of 3-D structures and their radiation on the ground TIR measurement increases by about 1.28 K from 0.90 K to 2.18 K. If H/W is fixed at 2.0, while road emissivity decreases from 0.973 to 0.921, the impact of 3-D structures and their radiation could increase from 1.00 K to 2.98 K. If wall temperature increases from 260 K to 340 K while the other parameters remain at default values, the impact of 3-D structures and their radiation increases rapidly from 0.66 K to 3.62 K. In addition, based on results in Section 3.3.2, the minimum magnitude of the impact of 3-D structures and their radiation on ground TIR measurements is about 0.31 K in cases with road temperature of 300 K, road emissivity of 0.950, H/W of 0.5, wall emissivity of 0.906, and wall temperature of 260 K; whereas a maximum value of about 4.21 K may be obtained in cases with road temperature of 300 K, road emissivity of 0.950, H/W of 4.0, wall emissivity of 0.906, and wall temperature of 340 K.

The respective contributions of atmosphere and building wall to total ground TIR measurements over a road were also considered. According to the simulations, the contribution of a building wall to the total ground TIR measurements can be greatly affected by radiation from 3-D surroundings. For nadir observations of a scenario with wavelength of 10 μm, the contribution of a building wall is more significant in cases with lower road emissivity and higher wall temperature, because more environmental radiance would be reflected into the remote sensor by the target pixel. For example, if H/W is fixed at 2.0, road temperature is fixed at 300 K, wall emissivity is fixed at 0.906, and road emissivity is fixed at 0.950, the contribution of a wall increases from 1.12 K to 4.12 K with increasing wall temperature from 260 K to 340 K. When wall temperature is fixed at 300 K, the contribution of the wall would increase rapidly from 1.69 K to 3.69 K as road emissivity decreased from 0.973 to 0.921. Results also show that even though the absolute value of road-reflected environmental radiance remains the same if only the road temperature varies, the contributions of atmosphere and wall to total ground TIR measurement still change. This is because the self-emitted radiance of the road decreases as road temperature decreases, allowing for the proportion of road-reflected environmental radiance in the total TIR measurements to increase. For example, for the cases with H/W of 2.0, wall temperature of 300 K, wall emissivity of 0.906, and road emissivity of 0.921, the contribution of a wall could increase from 2.71 K to 5.89 K as road temperature decreases from 340 K to 260 K, whereas the contribution of atmosphere also increases from 0.18 K to 0.39 K. In fact, based on the results presented in Section 3.3.3, the radiation from a

building wall is the primary cause of the impact of 3-D structures and their radiation on TIR measurement, because the maximum magnitude of the contribution of atmosphere to the total ground TIR measurements is < 0.40 K. However, if road emissivity is low, both contributions from the building wall and from the atmosphere cannot be ignored.

To summarize, the impact of 3-D structures and their radiation on the TIR measurements generally cannot be neglected except that the emissivities of the components inside that street canyon are low. Otherwise, the proposed ATIMOU provides a convenient tool to calculate the magnitude of this impact quantitatively and accurately. Since the ATIMOU could provide analytical solutions, it has the potential to be combined with the traditional LST retrieval algorithms to develop new LST retrieval methods with consideration of the urban 3-D structures. Consequently, for high spatial resolution TIR images in which the 3-D structures of the street canyon could be recognized, the LST retrieval accuracy should be greatly improved, indicating that the relevant studies which require the urban LST, such as urban heat island, urban energy balance, et. al., could all benefit from the more accurate urban LST retrievals.

4 | Development of a prior-knowledge-free (PKF) method for accurate LST retrieval from satellite data

Land surface temperature (LST) is an important parameter in many research fields. Many algorithms have been developed to retrieve LST from satellite thermal infrared (TIR) measurements; of these, the most widely used are the split window (SW) and temperature–emissivity separation (TES) methods. However, the performance of the SW and TES methods can be limited by the difficulty in obtaining sufficiently accurate prior knowledge—specifically, input land surface emissivity (LSE) for the SW method and atmospheric parameters for the TES method. In this chapter, a procedure was proposed for selecting specific channel pairs in the TIR spectral region to accurately retrieve ground brightness temperatures without prior atmospheric knowledge, using a method similar to the SW method. Subsequently, the TES method is applied to the retrieved ground brightness temperatures to separate the LST and LSE. In numerical simulations, the three ground brightness temperatures corresponding to 8.6 μm, 9.0 μm, and 10.4 μm are acquired with an accuracy of about 0.65 K by using five channels centered at 8.6 μm, 9.0 μm, 10.4 μm, 11.3 μm, and 12.5 μm, each with a width of 0.1 μm. When inputting the three retrieved ground brightness temperatures into TES method, LST could be recovered with an accuracy of 0.87 K. Finally, the proposed method is preliminarily applied to actual satellite data from the Atmospheric InfraRed Sounder (AIRS) and the retrieved results are compared with the pixel-aggregated Moderate Resolution Imaging Spectroradiometer (MODIS) LST product. For the study area of Australia, discrepancies between our result and the MODIS LST product appear to be about 1.6 K during the day and 1.0 K at night, indicating that the new channel configuration can be used to retrieve accurate LST from satellite measurements.

4.1. Introduction

Land surface temperature (LST) is a key physical measurement of surface energy and water balance processes at both regional and global scales (Jackson et al., 1985; Jackson et al., 1977; Running et al., 1994; Sellers et al., 1988; Vining and Blad, 1992); it is used within many research fields, including hydrology, meteorology, and climatology (Anderson et al., 2008; Karnieli et al., 2010; Li et al., 2009; Tomlinson et al., 2011). Satellite remote sensing using measurements in the microwave (MW) and thermal infrared (TIR) spectral regions provides an efficient way to obtain the LST over extended regions (Becker and Li, 1990; Dash et al., 2001; Dash et al., 2002; Duan et al., 2017; McFarland et al., 1990; Schmugge et al., 1998; Yu et al., 2005). Although MW can penetrate through clouds, the resulting measurements have low spatial resolution and yield the "subsurface temperature" instead of the "skin temperature" provided by TIR remote sensing (Choudhury et al., 1982; Duan et al., 2017; Liu et al., 2013; Simmer, 1999). Furthermore, MW measurements are sensitive to soil moisture and surface roughness (Choudhury et al., 1979; Njoku and Entekhabi, 1996). Because of these shortcomings, TIR measurements are more widely used than MW measurements for LST retrieval. However, to determine an accurate LST, the data from satellite TIR measurements must be corrected for the effects of atmosphere and land surface emissivity (LSE) (Becker, 1987; Sobrino et al., 1991). In recent decades, many algorithms have been developed for this purpose (Dash et al., 2002; Li et al., 2013a; Prata et al., 1995; Sattari and Hashim, 2014); they can be roughly classified into four types (Li et al., 2013a; Li et al., 2013b): the single-channel (Jimenez-Munoz and Sobrino, 2003; Ottle and Vidal-Madjar, 1992; Qin et al., 2001b), day/night (Wan, 2008; Wan, 2014; Wan and Li, 1997; Wan and Li, 2008), split window (SW) (Becker and Li, 1990; Coll and Caselles, 1997; McMillin, 1975; Qin et al., 2001a; Wan and Dozier, 1996), and temperature-emissivity separation (TES) (Gillespie et al., 1998) methods. With the use of these methods, LSTs have been successfully retrieved from satellite measurements under specific assumptions.

As documented in previous studies (Li et al., 2013a; Li et al., 2013b; Sattari and Hashim, 2014), these commonly used methods have advantages as well as disadvantages. The single channel method utilizes a simple inversion of the radiative transfer equation and requires accurate LSE and atmospheric profiles in order to provide accurate LST retrievals (Ottle and Vidal-Madjar, 1992). In comparison, the day/night method only needs the shape information of the atmospheric profiles and can retrieve the LST and LSE simultaneously; however, large errors may be introduced into the retrieved results if the temporal images

are geometrically misregistered or the LSE changes significantly from day to night (Wan and Li, 1997). In addition, the complexity of the equation-solving task also limits this method's application. Alternatively, the SW method can accurately eliminate atmospheric effects by combining measurements from two adjacent channels. This method represents the LST as a polynomial function of the two channel brightness temperatures and is easy to apply; however, LSEs of the two channels must be known accurately to provide good LST retrievals (Becker, 1987). The TES method can also separate the LST and LSE simultaneously, although it requires accurate ground brightness temperatures as input, meaning that the performance of the TES method is dependent on the accuracy of atmospheric correction (Gillespie et al., 1998). Each of these existing method has limitations and may be unable to meet the LST retrieval accuracy of ≤1.0 K that is required by many disciplines under certain circumstances (Sobrino et al., 2016). Considering the complementary advantages and disadvantages of the SW and TES methods, a hybrid method was proposed by Ren et al. (Ren et al., 2018) to improve LST retrieval accuracy. That being said, the improvements are questionable because this method still does not address the accurate atmospheric correction required by the TES algorithm. To overcome this problem, this study proposes a procedure to select specific channel pairs in the TIR spectral region for retrieving accurate ground brightness temperatures from satellite observations by using a method that is similar to the SW method. When applying the TES method to these retrieved ground brightness temperatures, the LST can be accurately retrieved without any prior LSE or atmospheric knowledge.

This chapter is organized as follows: Section 4.2 demonstrates the theoretical basis of the proposed method; Section 4.3 describes the method for determining the new channel configuration; Section 4.4 presents a sensitivity analysis of the proposed method; and Section 4.5 covers a preliminary application and validation with real satellite data. Finally, Section 4.6 summarizes our main findings.

4.2. Methodology

Drawing on the SW method, a procedure was deduced for acquiring accurate ground brightness temperatures. The general radiative transfer equation for TIR remote sensing can be formulated as follows (Becker and Li, 1990, Wan and Dozier, 1996, Wan and Li, 1997):

$$B(T_i) = \tau_i B(T_{gi}) + L_i^\uparrow \qquad\qquad \text{Eq. 4-1}$$

with

$$B(T_{gi}) = \varepsilon_i B(T_s) + (1 - \varepsilon_i)L_i^{\downarrow},$$ Eq. 4-2

where subscript i is channel i; T_i and T_{gi} are the brightness temperature and ground brightness temperature of channel i, respectively; B represents the Planck function; ε_i and T_s are the LSE and LST; τ_i denotes the atmospheric transmittance of channel i; and $L_i^{\downarrow}$ and $L_i^{\uparrow}$ are the atmospheric downwelling and upwelling radiance of channel i. When employing the mean value theorem (Coll et al., 1994; McMillin, 1975; Prata, 1993), $L_i^{\uparrow}$ can be expressed by

$$L_i^{\uparrow} = (1 - \tau_i)B(T_{ai}),$$ Eq. 4-3

where T_{ai} is the effective mean atmospheric temperature. Substituting Eq. 4-3 into Eq. 4-1 produces

$$B(T_i) = \tau_i B(T_{gi}) + (1 - \tau_i)B(T_{ai}).$$ Eq. 4-4

Eq. 4-4 can also be applied to another channel, j:

$$B(T_j) = \tau_j B(T_{gj}) + (1 - \tau_j)B(T_{aj}).$$ Eq. 4-5

Assuming that the ground brightness temperature, effective mean atmospheric temperature, and brightness temperature of channels i and j are close to each other, the first-order Taylor series of the Planck function can be applied to Eq. 4-4 and Eq. 4-5 around T_i, as follows:

$$T_i - T_{ai} = \tau_i(T_{gi} - T_{ai})$$ Eq. 4-6

$$T_j - T_{aj} = \tau_j(T_{gj} - T_{aj}).$$ Eq. 4-7

T_{ai} can be expressed as a linear function of T_{aj},

$$T_{ai} = mT_{aj} + n,$$ Eq. 4-8

where m and n are constants related to channels. By combining Eq. 4-6, Eq. 4-7, and Eq. 4-8, and eliminating T_{ai} and T_{aj}, T_{gi} could be written as a function of T_i and T_j, as in

the SW method:

$$T_{gi} = k + pT_i + q(T_i - T_j) + \Delta, \qquad \text{Eq. 4-9}$$

with

$$k = \frac{n(\tau_i - 1)(\tau_j - 1)}{m\tau_j(1 - \tau_i) - \tau_i(1 - \tau_j)} \qquad \text{Eq. 4-10}$$

$$p = \frac{(\tau_j - 1) - m(\tau_i - 1)}{m\tau_j(1 - \tau_i) - \tau_i(1 - \tau_j)} \qquad \text{Eq. 4-11}$$

$$q = \frac{(\tau_i - 1)}{m\tau_j(1 - \tau_i) - \tau_i(1 - \tau_j)} \qquad \text{Eq. 4-12}$$

$$\Delta = \frac{m\tau_j(\tau_i - 1)}{m\tau_j(1 - \tau_i) - \tau_i(1 - \tau_j)}\left(T_{gj} - T_{gi}\right). \qquad \text{Eq. 4-13}$$

When the atmospheres are not too wet, the coefficients of *k*, *p* and *q* can be considered as constants. If the channel combination of *i* and *j* meets at least one of these conditions for different atmospheres and land surfaces—(1) Δ is close to zero, (2) Δ is a linear function of T_i, or (3) Δ is a linear or quadratic function of $(T_i - T_j)$—then T_{gi} can be directly retrieved from satellite measurements, as with the SW method for the sea surface [Eq. 4-14]:

$$T_{gi} = A_0 + A_1 T_i + A_2\left(T_i - T_j\right) + A_3(T_i - T_j)^2, \qquad \text{Eq. 4-14}$$

where A_0, A_1, A_2, and A_3 are constants. The introduction of the quadratic item $A_3(T_i - T_j)^2$ further improves the retrieval accuracy of T_{gi}, as in the SW method (Coll and Caselles, 1997; Coll et al., 1994; Du et al., 2015; Galve et al., 2008; Sobrino et al., 1993; Wan, 2014).

After obtaining accurate T_{gi}, the TES method can be applied to retrieve the LST with high accuracy. Because the TES method requires at least three T_{gi} as inputs (Sobrino and Jiménez-Muñoz, 2014), it is critical to find a minimum of three channel pairs that can be applied to Eq. 4-14 to obtain at least three accurate T_{gi} in the TIR region. Subsequently, the LST can be accurately retrieved using the TES algorithm, provided that the spectral locations of T_{gi} provide a good empirical relationship between the minimum emissivity (ε_{min}) and maximum–minimum emissivity difference (*MMD*) (Gillespie et al., 1998; Hu et al., 2015). An illustration of the proposed method is shown in Fig. 4-1.
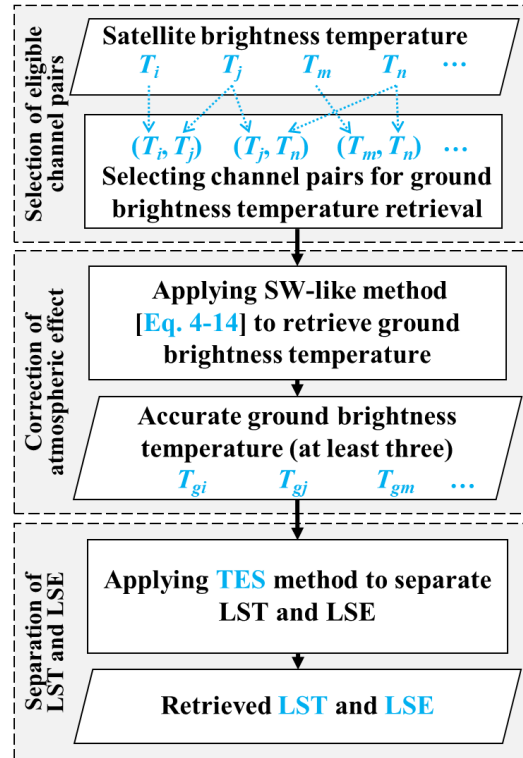
Fig. 4-1. Illustration of the proposed method for accurate LST retrieval.

4.3. Determination of the new channel configuration

Because the commonly used TIR images do not provide the channel pairs required by the method described in Section 4.2, a new channel configuration needs to be determined. First, a simulation dataset was made using the MODerate resolution atmospheric TRANsmission (MODTRAN) code (Berk et al., 2005). Then, channel pairs that were eligible to retrieve accurate T_{gi} using Eq. 4-14 were searched iteratively in the TIR region with the help of the simulation dataset. Finally, the spectral locations of the eligible channels were optimized manually. A detailed flow diagram of this process is shown in Fig. 4-2.
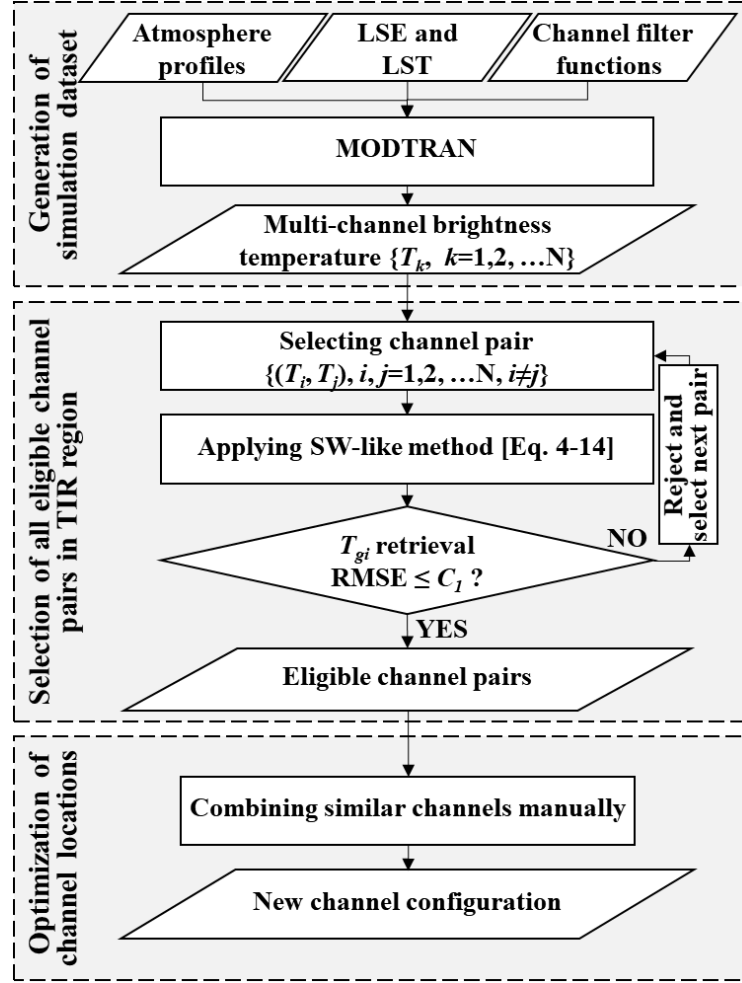
Fig. 4-2. Flow diagram for determining the new channel configuration. T_k, T_i, and T_j are channel brightness temperatures, C_1 is a constant for testing whether a channel pair is eligible to retrieve accurate ground brightness temperature.

4.3.1. Simulation dataset for determining a new channel configuration

By using MODTRAN, the satellite channel brightness temperatures in the TIR region can be simulated given the LSE, LST, atmosphere profiles, and channel filter functions. As in the method suggested by (Sobrino and Jiménez-Muñoz, 2014), the channel filter function was simulated as a composite form of the Gaussian and triangle functions. The equations can be expressed as

$$f(\lambda) = \begin{cases} \frac{\lambda}{FWHM} + \left(1 - \frac{\lambda_0}{FWHM}\right) & \lambda_0 - FWHM < \lambda < \lambda_0 - \frac{FWHM}{2} \\ \exp\left[-\frac{(\lambda - \lambda_0)^2}{2\sigma^2}\right] & \lambda_0 - \frac{FWHM}{2} < \lambda < \lambda_0 + \frac{FWHM}{2} \\ -\frac{\lambda}{FWHM} + \left(1 + \frac{\lambda_0}{FWHM}\right) & \lambda_0 + \frac{FWHM}{2} < \lambda < \lambda_0 + FWHM \end{cases} , \qquad \text{Eq. 4-15}$$

where $f(\lambda)$ is the channel filter function; λ is the wavelength; *FWHM*, the full width at half maximum, is the channel width; λ_0 is the channel center; and σ is the width of the Gaussian function, which is related to the *FWHM* by $\sigma = FWHM/(2\sqrt{2ln2}) \approx 0.42FWHM$. In this study, the spectral region from 8.0 μm to 14.0 μm was considered, with channel center intervals of 0.1 μm. The *FWHM* of each channel was initially set as 0.1 μm. Thus, 59 successive channel filter functions were generated using Eq. 4-15 (Fig. 4-3).
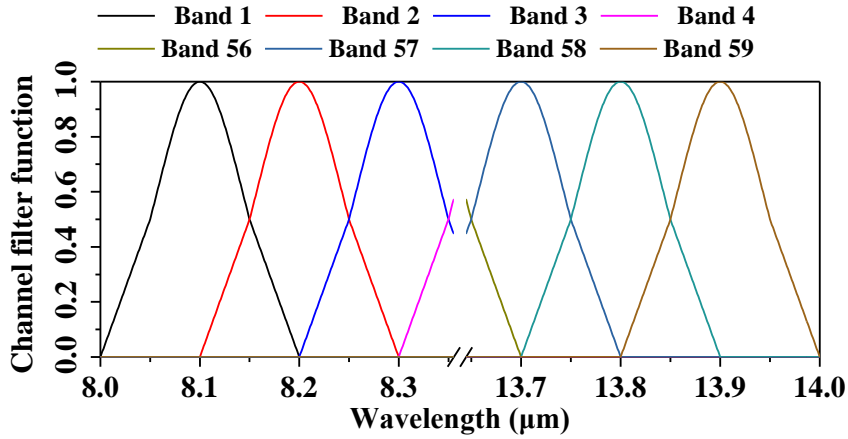
Fig. 4-3. Simulated channel filter functions.

Following the research of Chen et al. (Chen et al., 2017), 65 LSE spectra were selected from the ECOSTRESS Spectral Library, Version 1.0 (https://speclib.jpl.nasa.gov/) to represent different land surface coverages, including 52 soil, 4 vegetation, and 9 water/ice/snow samples (Fig. 4-4a, b, and c). Additionally, 98 atmosphere profiles were selected from the Thermodynamic Initial Guess Retrieval (TIGR, http://ara.abct.lmd.polytechnique.fr/) database, with the water vaper content ranging from 0.09 g/cm² to 6.15 g/cm². The input LST was assigned according to the bottom layer temperature T_0 of each atmosphere profile. If $T_0 \geq 280$ K, then the LST varied from $T_0 - 5$ K to $T_0 + 15$ K with intervals of 5 K. Otherwise, the LST varied from $T_0 - 5$ K to $T_0 + 5$ K with intervals of 5 K (Chen et al., 2017). With the input parameters described above, 29,640 cases were generated in the simulation dataset.
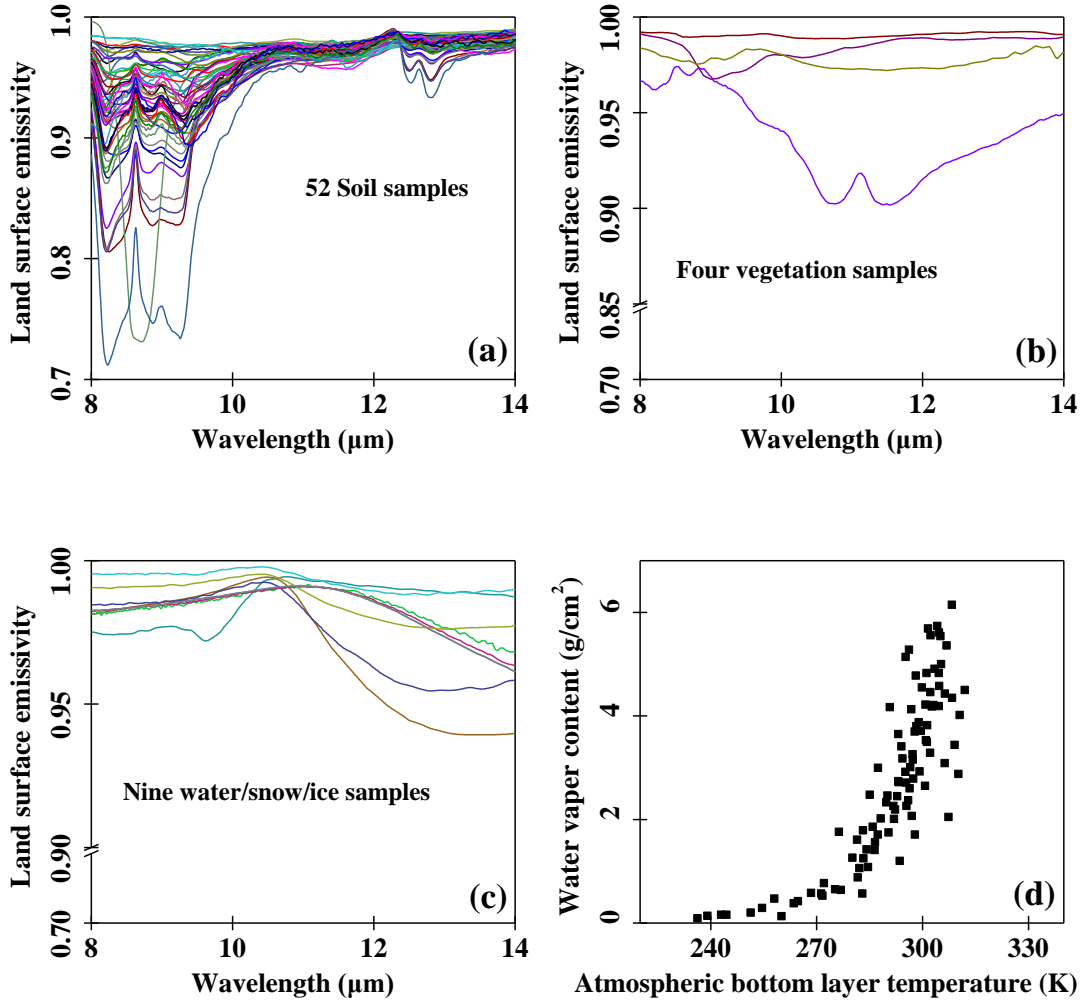
Fig. 4-4. (a) LSE spectra of the 52 soil samples, (b) LSE spectra of the four vegetation samples, (c) LSE spectra of the nine water/snow/ice samples, and (d) scatter plot of the bottom layer temperature and water vaper content of the 98 atmosphere profiles.

4.3.2. Selection of eligible channel pairs for retrieving ground brightness temperature

Theoretically, there are 3,363 possible two-channel combinations using the 59 simulated channels, although some of them do not meet the conditions that eligible channel pairs conform to; that is, the value of Δ in Eq. 4-9 is neither close to zero, nor a linear function of T_i, nor a linear or quadratic function of $(T_i - T_j)$. In this study, the root-mean-square error (RMSE) of the retrieved T_{gi} was chosen as an indicator of whether a channel pair met at least one of these conditions. A threshold (i.e., C_1 in Fig. 4-2) of 0.7 K was used to find all eligible channel pairs. This threshold was determined by trial-and-error to allow the final LST to be retrieved within the expected accuracy of 1.0 K. After filtering by the

threshold and excluding channels inside the ozone absorption band from 9.4 μm to 10.0 μm, 44 eligible channel pairs associated with 28 individual channels remained (Fig. 4-5).
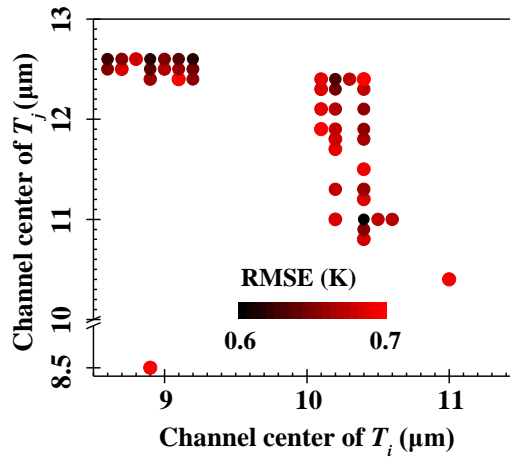
Fig. 4-5. The spectral centers of eligible channel pairs. The retrieval RMSE of the ground brightness temperature of channel i (T_{gi}) is represented by the color scale.

4.3.3. Optimization of eligible channel locations

Some of the 28 channels composing the 44 remaining eligible channel pairs from Section 4.3.2 were very similar, as a result of the channel filter functions being generated with a small channel center interval of 0.1 μm. Thus, it was reasonable to reduce the total number of channels; specifically, some channels were removed so that adjacent channel center intervals were greater than or equal to 0.2 μm. This process was done manually in order to evenly distribute the locations of the remaining channels. After refinement, 16 of the 28 individual channels remained (marked by triangles in Fig. 4-6a), forming 18 eligible channel pairs (Fig. 4-6b).
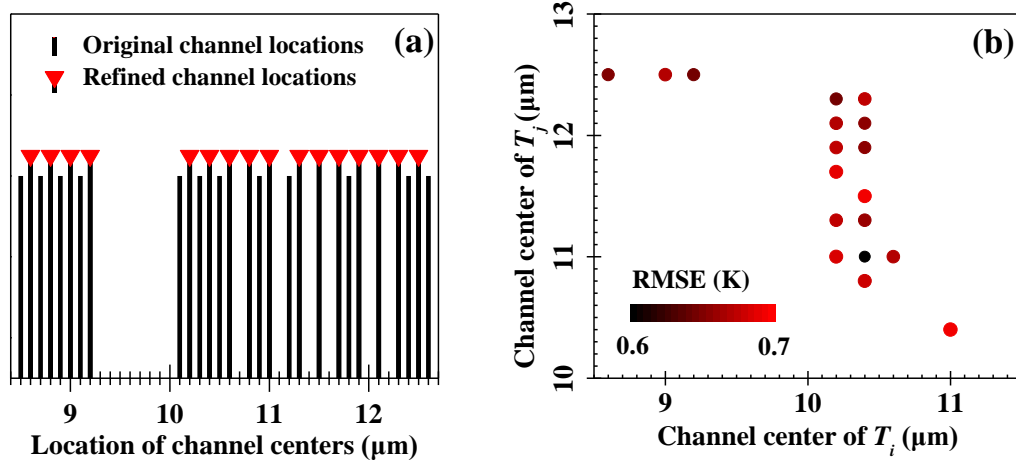
Fig. 4-6. Optimization of the eligible channel locations. (a) Channels remaining after refinement are indicated by triangles; (b) eligible channel pairs remaining after refinement for retrieving the ground brightness temperature of channel i (T_{gi}).

4.3.4. Retrieval of ground brightness temperature and LST

Using the refined eligible channel pairs, seven highly accurate T_{gi} were retrieved. Note that the T_{gi} at 10.2 μm and 10.4 μm could be retrieved repeatedly by combining with different T_j (Fig. 4-6b). Therefore, the retrieved T_{gi} of the channels at 10.2 μm and 10.4 μm were averaged respectively before applying the TES algorithm. Numerical simulations indicated that the spectral locations of T_{gi} provided a good ε_{min} ~ *MMD* relationship (Fig. 4-7a) and LST could be retrieved to within 1.0 K by using the refined eligible channels (Fig. 4-7b).
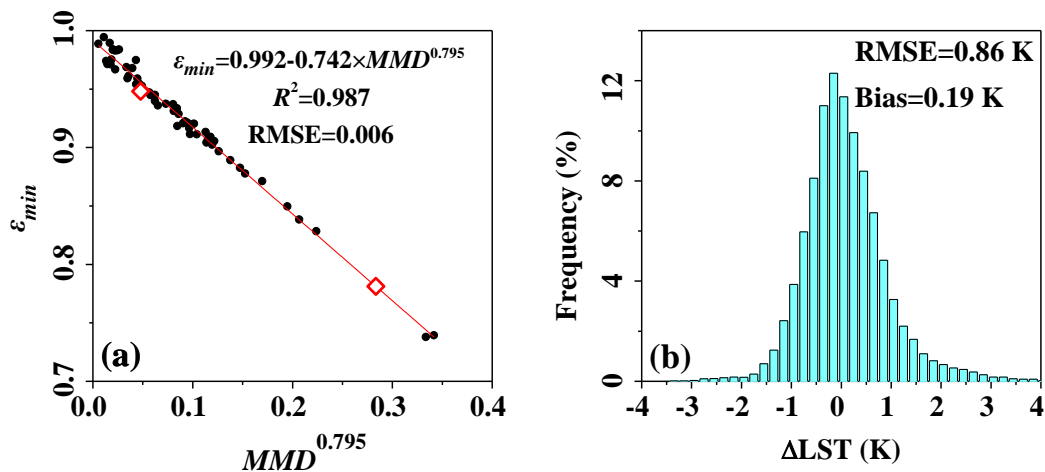
Fig. 4-7. (a) The empirical relationship between ε_{min} and *MMD*, based on the 65 samples described in Section 4.3.1. Diamonds represent two additional rock samples used in Section 4.4.3 for sensitivity analysis. (b) Histogram of the residuals between the retrieved and true LSTs.

Previous studies indicated that three T_{gi} can meet the minimum requirement of the TES algorithm (Gillespie et al., 1998; Sobrino and Jiménez-Muñoz, 2014). Considering 16 individual channels connected with the 18 remaining eligible channel pairs is unreasonable when developing an instrument; therefore, only three eligible channel pairs were selected to study the performance of the proposed method. To accurately retrieve the LST, the spectral locations of the T_{gi} should provide enough emissivity contrast to estimate the ε_{min}. Detailed information about the three channel pairs used in this study is listed in Table 4-1. Retrieval results indicated that the T_{gi} at 8.6 μm, 9.0 μm, and 10.4 μm could be acquired with accuracies of approximately 0.65 K using Eq. 4-14 (Fig. 4-8a), and showed that the LST could be retrieved with an accuracy of ≤1.0 K using these three T_{gi} (Fig. 4-8b). Therefore, in the following sections, a configuration of 8.6 μm, 9.0 μm, 10.4 μm, 11.3 μm, and 12.5 μm for the five channels was used as an example, although other appropriate options may also exist.

Table 4-1. The three recommended channel pairs for retrieving T_{gi} and the fitted coefficients of Eq. 4-14.

Center of channel i (μm)	Center of channel j (μm)	A_0	A_1	A_2	A_3	T_{gi} retrieval RMSE (K)
8.6	12.5	-6.75	1.03	0.39	0.02	0.64
9.0	12.5	-3.79	1.02	0.30	0.02	0.66
10.4	11.3	0.27	1.00	1.04	0.20	0.65
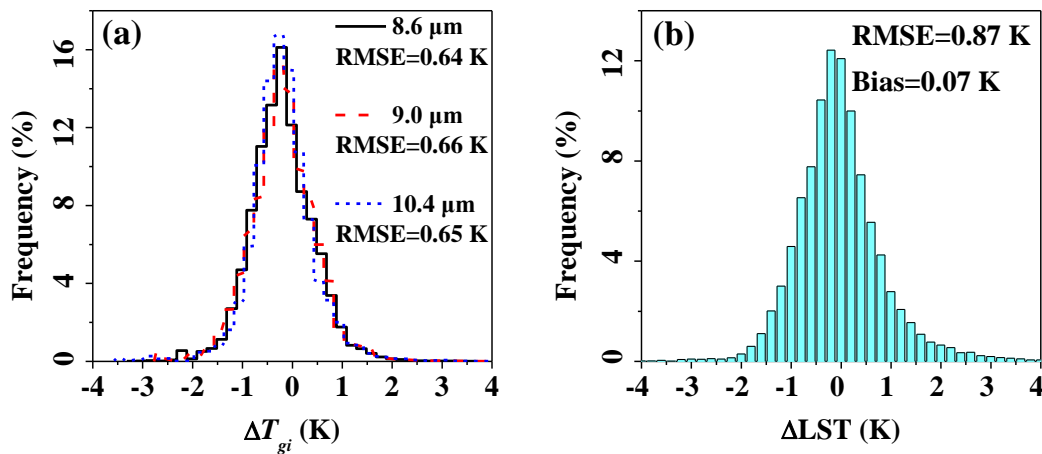
Fig. 4-8. (a) Histograms of the residuals between the retrieved and true ground brightness temperature (T_{gi}) for different channels. (b) Histogram of the residuals between the retrieved and true LST.

4.4. Sensitivity analysis

4.4.1. Sensitivity analysis to channel noise and channel width

4.4.1.1. Sensitivity analysis to channel noise with a channel width of 0.1 μm

Instrumental noise causes actual observed channel brightness temperatures to contain random errors that could affect LST retrieval accuracy. Therefore, a sensitivity analysis was performed by adding a noise-equivalent differential temperature (NEΔT) to the simulated channel brightness temperatures before applying the proposed method. The results showed that the RMSEs of the three retrieved T_{gi} increased with the channel NEΔTs, and the channel at 10.4 μm was more sensitive to channel noise than the other two channels (Fig. 4-9a). The biases of the retrieved LST indicated that the results were overestimated; this is believed to be caused by the introduction of the quadratic item in Eq. 4-14 (Fig. 4-9b). Results also showed that the RMSE of the retrieved LST slightly increased, but was still accurate to within 1.0 K, when the NEΔT was below 0.1 K; however, accuracy was only within 1.2 K and 1.4 K when noise levels of 0.2 K and 0.3 K, respectively, were added to the channel brightness temperatures (Fig. 4-9b). Therefore, channel noise must be well controlled to accurately retrieve LSTs using the proposed method.
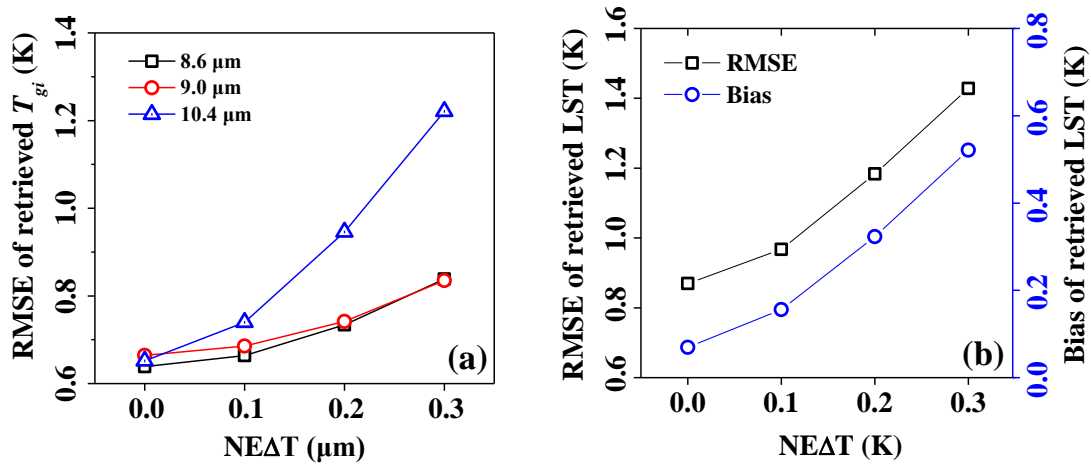
Fig. 4-9. (a) The RMSEs of the retrieved ground brightness temperatures for different channels (T_{gi}) as a function of channel NEΔT. The channel FWHM was fixed at 0.1 μm. (b) The LST retrieval RMSE and bias as a function of channel NEΔT.

4.4.1.2. Sensitivity analysis to channel width without channel noise

The retrieval accuracies of T_{gi} and LST may also affected by the channel witdth. To evaluate the impact of this factor, a sensitivity analysis was performed by varying the channel FWHM before obtaining the simulated channel brightness temperatures. As the channels broadened, the retrieval accuracy of the T_{gi} at 8.6 μm rapidly decreased (Fig. 4-10a). Although the RMSEs of the other two channels also generally increased with the FWHM (Fig. 4-10a), they were less affected when the channel FWHM was in some certain ranges (0.1–0.4 μm for the channel at 9.0 μm and 0.3–0.5 μm for the channel at 10.4 μm). Additionally, LST retrieval accuracy decreased to about 1.0 K as the FWHM increased to 0.3 μm, whereas the RMSE of the retrieved LST only slightly increased as channel width continuously increased (Fig. 4-10b); this variation pattern was similar to that for the retrieval accuracy of T_{gi} at 10.4 μm. This may have occurred because, in the TES algorithm, LST is always calculated from the channel with the highest emissivity. For most land surface coverages, the emissivity of the channel at 10.4 μm is larger than that of the other two channels. Thus, LST retrieval accuracy was more influenced by the T_{gi} retrieval accuracy for the channel at 10.4 μm.
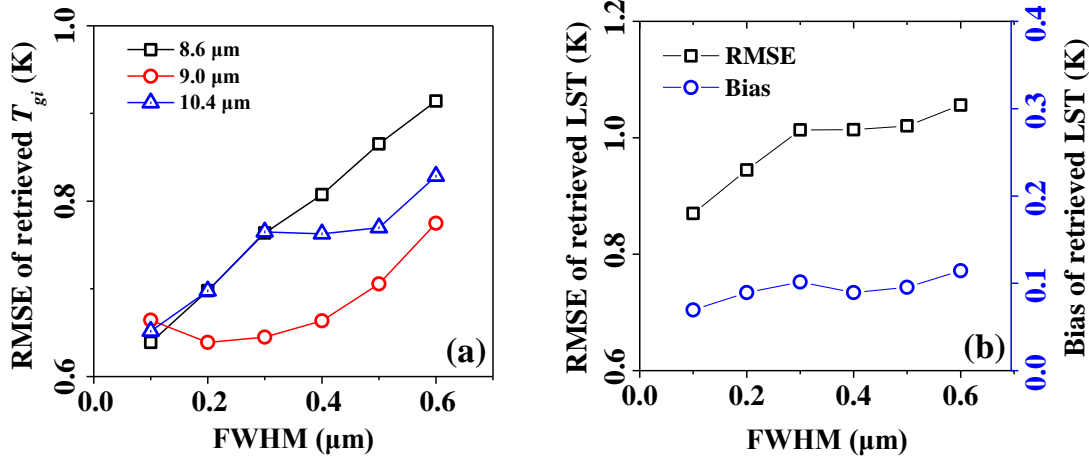
Fig. 4-10. (a) The RMSE of retrieved ground brightness temperature for different channels (T_{gi}) as a function of channel FWHM. The channel NEΔT was fixed at 0.0 K. (b) The LST retrieval RMSE and bias as a function of channel FWHM.

4.4.1.3. Sensitivity analysis to channel width with channel noise

Since channel noise is related to channel width, the accuracy of retrieved LST for different combinations of channel NEΔT and channel FWHM was also analyzed. The results showed that the RMSE of the retrieved LST increased with FWHM up to 0.3 μm

and then stabilized (Fig. 4-11). A maximum error of about 0.3 K was introduced to LST retrievals as the channel width was broadened from 0.1 μm to 0.6 μm. Furthermore, LST retrieval accuracy was more influenced by the channel noise because the NEΔT was magnified twice and transferred to the final LST retrievals (Fig. 4-11). As shown in Fig. 4-11, when both factors are considered, the LST should be retrieved within the accuracy of about 1.2 K and 1.5 K for sensors with a channel NEΔT of 0.1 K and 0.2 K, respectively.
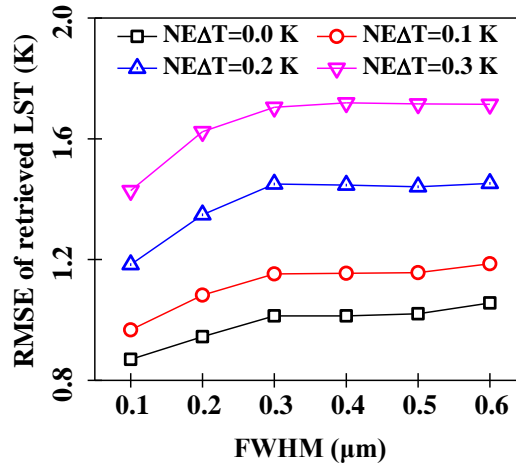
Fig. 4-11. The LST retrieval RMSE as a function of channel FWHM for different levels of channel NEΔTs.

4.4.2. Sensitivity analysis to the channel center

For actual satellite instruments, the channel filter functions are not ideal mathematical functions (in contrast with the Gaussian and triangle functions used in Section 4.3.1), which may lead to the shift of effective channel centers. Therefore, impact of channel-center shifts on LST retrieval accuracy using the proposed method was evaluated. Offsets of -0.2 μm to 0.2 μm, with intervals of 0.1 μm, were added to the spectral centers of the five channel filter functions before simulating the satellite brightness temperatures. For simplicity, the same offset value was used for all five involved channels each time. The results showed that the retrieval accuracies of T_{gi} at 8.6 μm and 10.4 μm decreased along with the shifting of channel centers. Additionally, these two T_{gi} were retrieved less accurately when the channel centers shifted to shorter wavelengths than when they shifted to longer wavelengths (Fig. 4-12a). The retrieval accuracy of T_{gi} at 9.0 μm was unaffected by channel-center shifts, except for those of -0.2 μm (Fig. 4-12a). With the shifting of channel centers, retrieved LSTs were overestimated and retrieval accuracy decreased to greater than 1.0 K (Fig. 4-12b). These results indicate that a shift of channel centers introduces large errors to

the retrieved T_{gi} and LST. Therefore, it is highly recommended to keep the channel centers at their initial locations when possible.
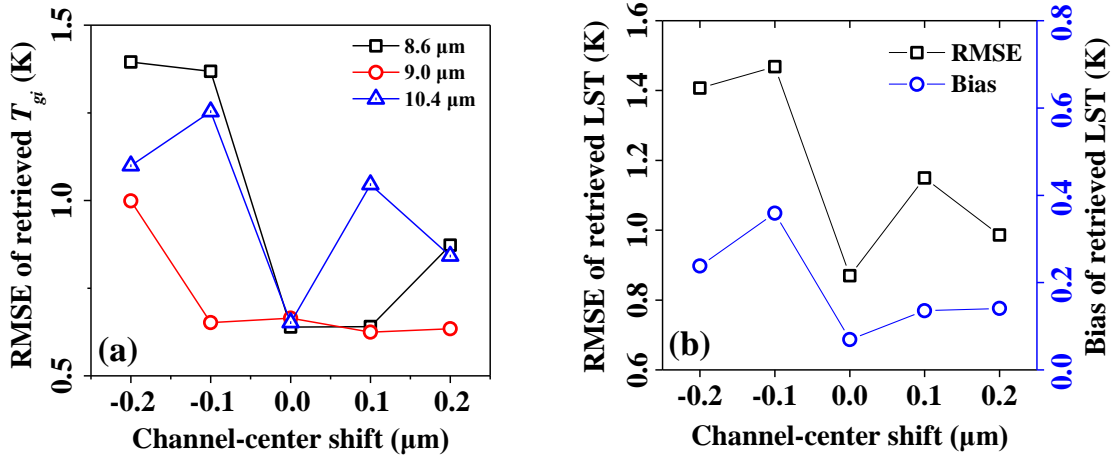
Fig. 4-12. (a) The RMSE of retrieved ground brightness temperature for different channels (T_{gi}) as a function of channel-center shifts. (b) The LST retrieval RMSE and bias as a function of channel-center shifts.

4.4.3. Sensitivity analysis to atmospheric downwelling radiance and LSE characteristics

The original TES algorithm requires the atmospheric downwelling radiance in order to refine the retrieved LST and LSE. The above results are all based on the simulated atmospheric downwelling radiance of the three selected channels ($L^{\downarrow}_{8.6\,\mu m}$, $L^{\downarrow}_{9.0\,\mu m}$, and $L^{\downarrow}_{10.4\,\mu m}$) without uncertainties. Therefore, it is necessary to investigate the influence on LST retrieval accuracy when real atmospheric measurements, or products containing errors, are used. In this study, sensitivity analysis was conducted by adding relative errors to $L^{\downarrow}_{8.6\,\mu m}$, $L^{\downarrow}_{9.0\,\mu m}$, and $L^{\downarrow}_{10.4\,\mu m}$ before applying the TES algorithm. Since $L^{\downarrow}_{8.6\,\mu m}$, $L^{\downarrow}_{9.0\,\mu m}$, and $L^{\downarrow}_{10.4\,\mu m}$ are highly correlated with each other, the empirical relationships between $L^{\downarrow}_{9.0\,\mu m}$ and $L^{\downarrow}_{8.6\,\mu m}$, and between $L^{\downarrow}_{10.4\,\mu m}$ and $L^{\downarrow}_{8.6\,\mu m}$ were first built using quadratic functions with an intercept of zero (Fig. 4-13a). Then, relative errors from -40% to 40%, with intervals of 10%, were added to $L^{\downarrow}_{8.6\,\mu m}$. Using the two empirical relationships shown in Fig. 4-13a, $L^{\downarrow}_{9.0\,\mu m}$ and $L^{\downarrow}_{10.4\,\mu m}$ with relative errors could also be acquired. Subsequently, the LST was retrieved using these inaccurate atmospheric downwelling radiance measurements instead of the simulations without uncertainties.

Results showed that the RMSE of the retrieved LSTs increased as relative errors were

introduced into the atmospheric downwelling radiance (Fig. 4-13b). Overestimation of the atmospheric downwelling radiance had slightly a larger influence on LST retrieval accuracy than underestimation. However, the LST retrieval results were still acceptable, with an RMSE <1.0 K, even when a relative error of 40% was added to the atmospheric downwelling radiance (Fig. 4-13b). One possible reason for this phenomenon is that the final LST is always calculated from the channel with the largest emissivity in the TES algorithm (Gillespie et al., 1998).

Previous studies (Gillespie et al., 1999; Jimenez-Munoz et al., 2014) have also shown that errors in estimating atmospheric downwelling radiance are of minor significance for LST retrieval in most situations when using the TES algorithm. However, for warm atmospheres over cold and highly reflective ground surfaces, such errors may become significant enough to limit the TES algorithm's performance (Gillespie et al., 1998). In fact, the impact of inaccurate atmospheric downwelling radiance to the TES is complicated because the reflected atmospheric downwelling radiance is corrected based on the estimated emissivity, which may already be in error (Gustafson et al., 2006). To investigate the impact of these two coupled error sources on LST retrieval accuracy, biases were added to both the atmospheric downwelling radiance and ε_{min}. Considering that ε_{min} can be obtained with an uncertainty of about 0.006, using its relationship with *MMD* as illustrated in Fig. 4-7a, a value of 0.015 was used as the maximum bias introduced to ε_{min}. The maximum bias used for the atmospheric downwelling radiance was 40%. As shown in Fig. 4-13c, the impact of inaccurate atmospheric downwelling radiance on LST retrieval accuracy depends on the emissivity error. For cases in which these two source errors have opposite signs, their impact on the retrieved LST is reduced; otherwise, it is amplified. We also found that the LST could be retrieved with an accuracy of 1.0 K for most cases in which the uncertainty in the estimated ε_{min} was less than 0.0075. To illustrate the impact of surface emissivity characteristics on the retrieved LST, two additional LSE spectra (Fig. 4-14a) with different shapes from the previous 65 LSE samples (Fig. 4-4) were used. As shown in Fig. 4-7a (the diamond symbols), although the two LSE spectra are different from the 65 LSE spectra used in Section 4.3, provided that the surface spectra follow the ε_{min} ~ *MMD* relationship, the LST for these two rocks can be retrieved using our proposed method with an accuracy better than 0.6 K (Fig. 4-14b).
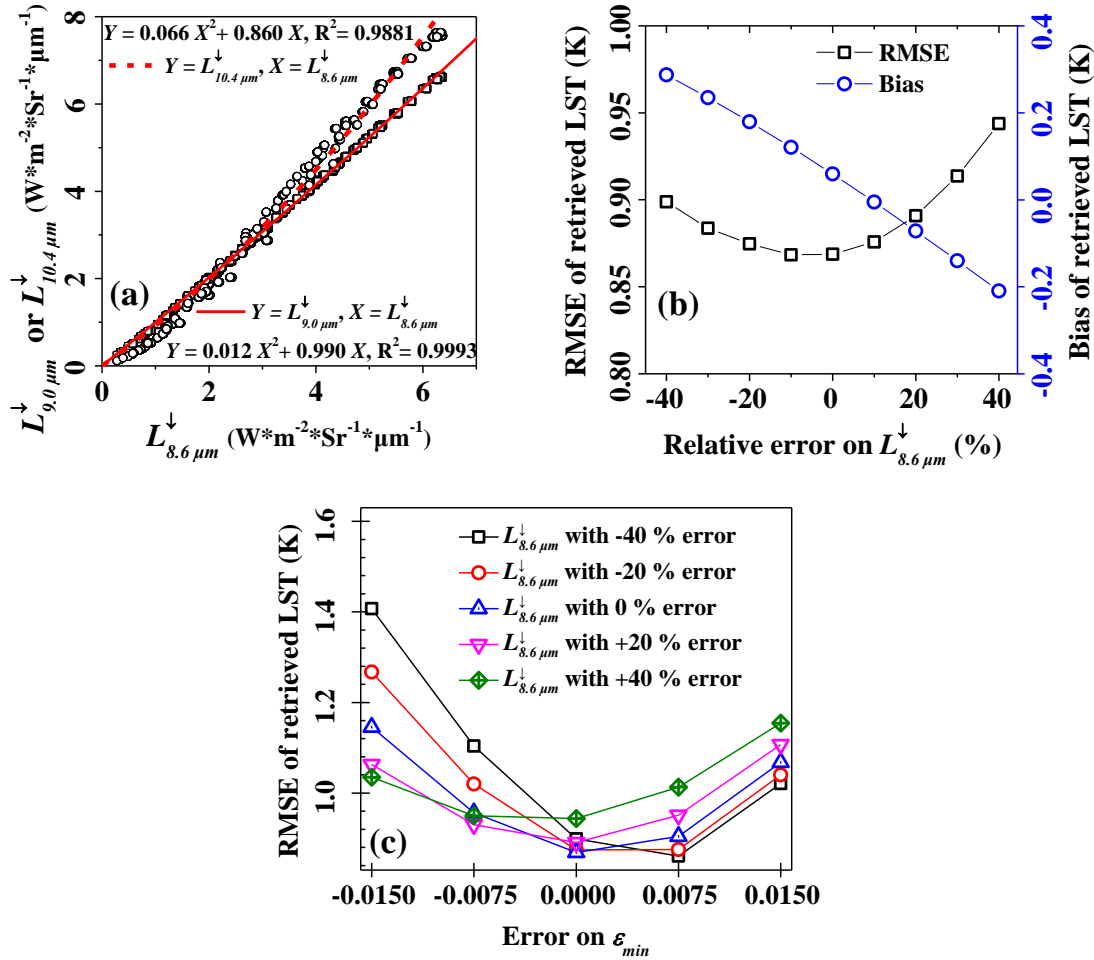
Fig. 4-13. (a) The empirical relationships between $L^{\downarrow}_{9.0\,\mu m}$ and $L^{\downarrow}_{8.6\,\mu m}$, and $L^{\downarrow}_{10.4\,\mu m}$ and $L^{\downarrow}_{8.6\,\mu m}$. (b) The LST retrieval RMSE and bias as a function of relative errors on the atmospheric downwelling radiance. (c) RMSE of retrieved LST using our proposed method with errors in both atmospheric downwelling radiance and minimum emissivity (ε_{min}).
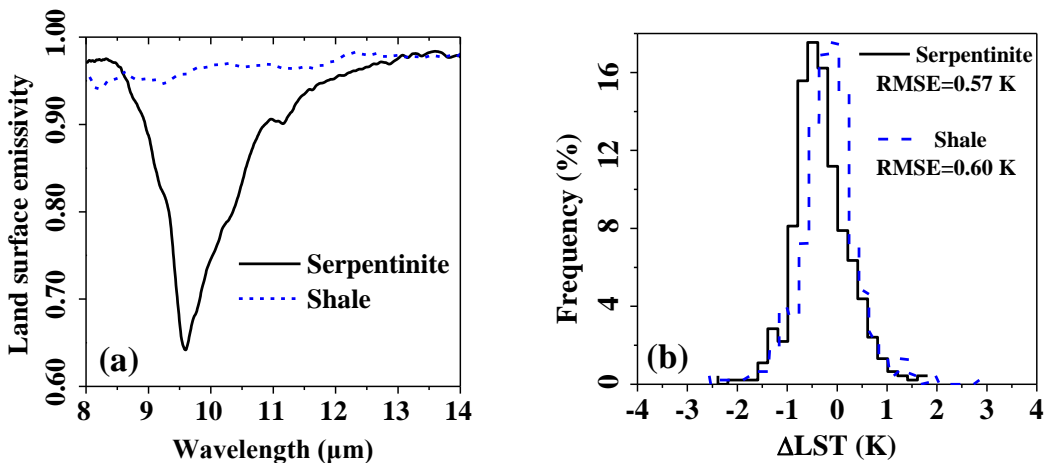
Fig. 4-14. (a) Additional LSE spectra, of two rocks, with different shapes from the previous 65 LSE samples displayed in Fig. 4-4. (b) Histogram of the residuals between the LST retrieved using the proposed method from data simulated with the spectra given in (a) and the true LST.

4.5. Application

The proposed method and suggested channel configuration were also applied to real satellite data to preliminarily verify its accuracy. Because no existing sensors have such a channel configuration, the level 1C hyper-spectral radiance of the Atmospheric InfraRed Sounder (AIRS_L1C) was introduced to calculate the theoretical measurements of the five required broad channels by using simulated channel filter functions (Moustafa, 2015). The pixel size of the AIRS image is 13.5 km × 13.5 km at nadir and is difficult to patch with ground truth measurements. Therefore, retrieval results were validated by comparison with the Land Surface Temperature/Emissivity 5-Min L2 Swath 1 km product (MYD11_L2) acquired by the Moderate Resolution Imaging Spectroradiometer (MODIS) (Wan et al., 2015b). A detailed processing flow diagram is shown in Fig. 4-15.
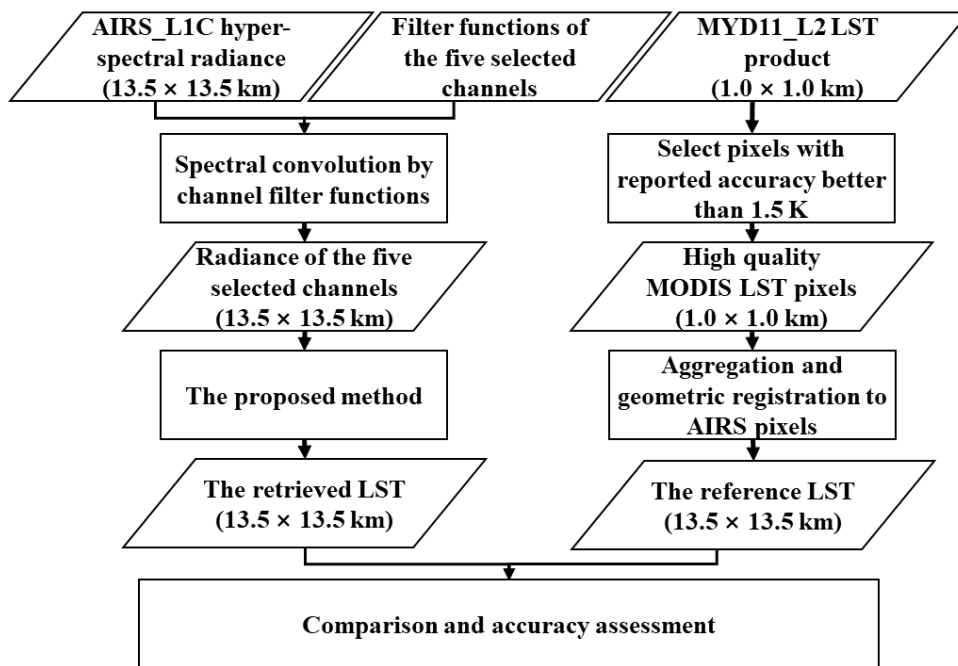
Fig. 4-15. The flow diagram of application based on real satellite data.

In one process, the LST was retrieved by using the proposed method on the theoretical multichannel observations acquired from AIRS hyper-spectral radiance. As demonstrated in Section 4.4.3, the impact of atmospheric downwelling radiance on the retrieved LST is small. Therefore, in this study, the required atmospheric downwelling radiance was estimated using MODTRAN with an atmospheric profile selected from the five standard

profiles (Tropical, Mid-Latitude Summer, Mid-Latitude Winter, Sub-Arctic Summer, Sub-Arctic Winter) using the method proposed by Harris (Harris, 2009) with the data acquisition month and the pixel geolocation (latitude). In another process, the MODIS LST product (MYD11_L2) was aggregated to match the AIRS spatial resolution for comparison using the area-weighted pixel aggregation algorithm (Gao et al., 2012; Qian et al., 2013). Detailed procedures are shown in Fig. 4-16. First, the MODIS LSTs were converted to radiance. Then, the weight of each MODIS pixel was calculated from the relationships between MODIS and AIRS pixel coordinates. Next, the radiance of all MODIS pixels inside or overlapped by the AIRS pixel were weighted to obtain the aggregated MODIS radiance with the spatial size of AIRS pixel. Finally, the aggregated MODIS LST was calculated from the aggregated radiance using the inverted Planck function.
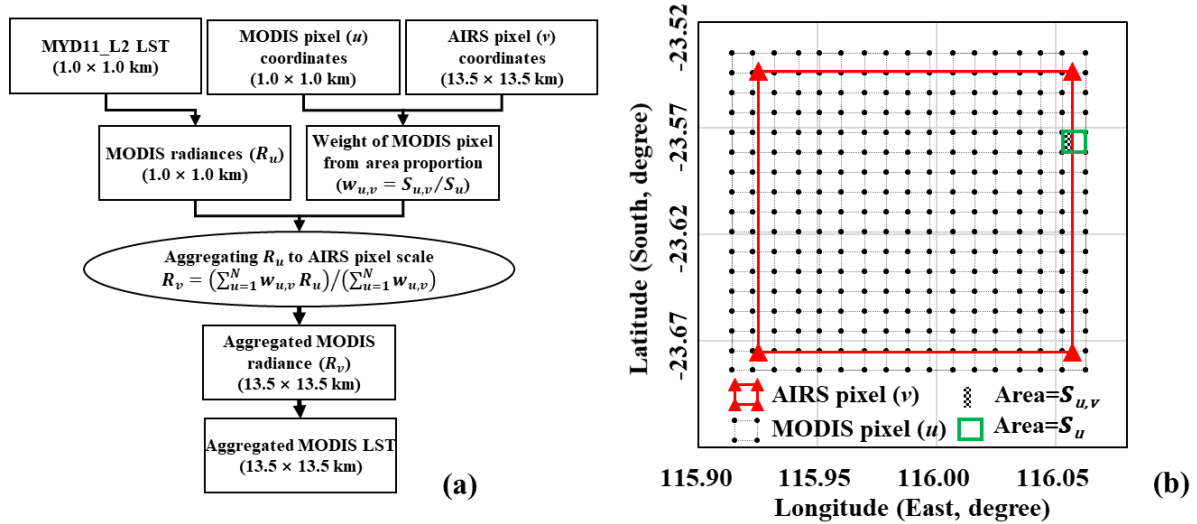
Fig. 4-16. (a) Flow diagram of the MODIS LST aggregating process, where N is the total number of MODIS pixels u inside or overlapped by one AIRS pixel v. (b) Illustration of the relationship between AIRS and MODIS pixel coordinates, where $S_{u,v}$ is the area of overlap between pixels u and v and S_u is the total area of pixel u.

Note that four restrictions were applied to refine the validation pixels. First, the "Error_LST" layer in the MYD11_L2 product was used to select cloud-free MODIS pixels that did not have any quality problems. Second, any MODIS pixels that produced an LST error larger than 1.5 K were eliminated according to the "QC" layer. Since uncertainties may be reduced by the aggregation process, the accuracy of the aggregated MODIS LST should be better than the accuracy of the original 1.0-km MODIS LST (i.e., better than 1.5 K). Third, when aggregating the MODIS pixels into the AIRS pixel scale, there should be

no invalid MODIS pixels inside the AIRS footprint and the standard error of the MODIS pixels should be less than 2.0 K (to retain the homogeneity of the validation pixels). Fourth, only pixels with an observation angle of less than 20° from nadir were selected because the coefficients acquired in Table 4-1 are only applicable for nadir observations. Note that the thresholds used in the third and fourth restrictions were chosen to balance the quantity and quality of the intercomparison pixel pairs. In this study, considering the fact that intercomparison was only performed if all MODIS pixels within one AIRS pixel have the uncertainty of LST about 1.5 K, consequently, a standard error of 2.0 K for all MODIS-derived LSTs within one AIRS pixel was chosen to guarantee the relatively homogeneous pixels in LST, and also to minimize the impact of spatial overlap error between aggregated MODIS pixels and AIRS pixels in the LST comparison. Moreover, both MODIS and AIRS have large viewing angles—up to about 50°. However, the coefficients listed in Table 4-1 were obtained from simulated data at the nadir. As there are very limited MODIS and AIRS pixel pairs available at the nadir, according to previous studies (Becker and Li, 1990; Sobrino et al., 1994; Wan and Dozier, 1996), the coefficients in the SW-like equation [Eq. 4-14] derived for nadir views can still be used without introducing significant error to viewing angles less than 20°; a viewing angle threshold of 20° was chosen to not only increase the total number of intercomparison pixel pairs, but also minimize the error introduced by a larger viewing angle.

In this study, Australia was chosen as a study area because it has a variety of land surface coverages and many cloudless days. Moreover, it has a relatively flat terrain, which can help to further suppress LST mismatches caused by instrumental observation angles. Because AIRS and MODIS are on board the same satellite platform (AQUA) and observe the same land surface patch within about five minutes, it was possible to preclude the possibility of LST mismatches associated with observation time. At last, 20 appropriate images were obtained from May 2018—10 during the day and 10 at night (Fig. 4-17a); additionally, 21 appropriate images were obtained from September 2018—nine during the day and 12 at night (Fig. 4-17b).
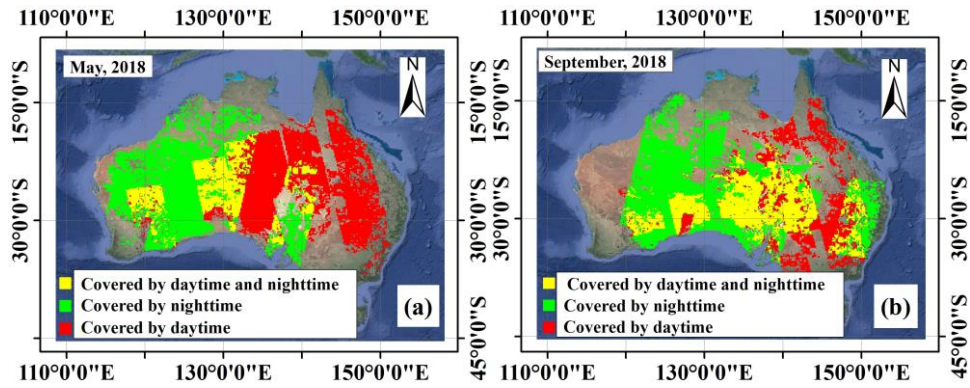
Fig. 4-17. The validation pixels collected in Australia and acquired in (a) May 2018, and (b) September 2018. Yellow indicates that the pixels are covered by both daytime and nighttime observations, green indicates the pixels are only covered by nighttime observations, and red indicates the pixels are only covered by daytime observations.

Since individual validation image pairs have fewer pixels because of the four restrictions placed on them, the observations acquired in the same month were merged as one image for each of these two months. The daytime and nighttime observations were processed separately from the statistics of the retrieval residuals. Compared with the MODIS LST product, the LST could be retrieved with an accuracy of <1.3 K for May (Fig. 4-18a and b) and <1.7 K for September (Fig. 4-18c and d). The biases indicated that our results overestimated the LST compared with the MODIS LST product. The LST retrievals at night had an accuracy of about 1.0 K compared with MODIS LST product and were always better than those from during the day. One reason for this result is that the LST was closer to the effective mean atmospheric temperature for nighttime, indicating that the errors resulting from the linearization of the Planck function in Eq. 4-14 were smaller than those for the daytime. Alternatively, this result could be attributed to the fact that larger errors, due to the replacement of Δ in Eq. 4-9, were introduced to the retrieved T_{gi} for daytime observations because the LST during the day is usually higher than that at night. Another possible reason is that the TIR radiance of the land surface is more homogenous at night. In this case, errors owing to the process of aggregating MODIS pixels to AIRS pixel scales should be smaller than those of the more heterogenous land surfaces found in daytime observations. Additionally, scatter plots showing the MODIS LST and the LST retrieval errors demonstrate that LST was overestimated to a greater extent for daytime than for nighttime observations (Fig. 4-19). More pixels were retrieved with discrepancies larger than 2.0 K from MODIS LST product as the LST approached 320 K.
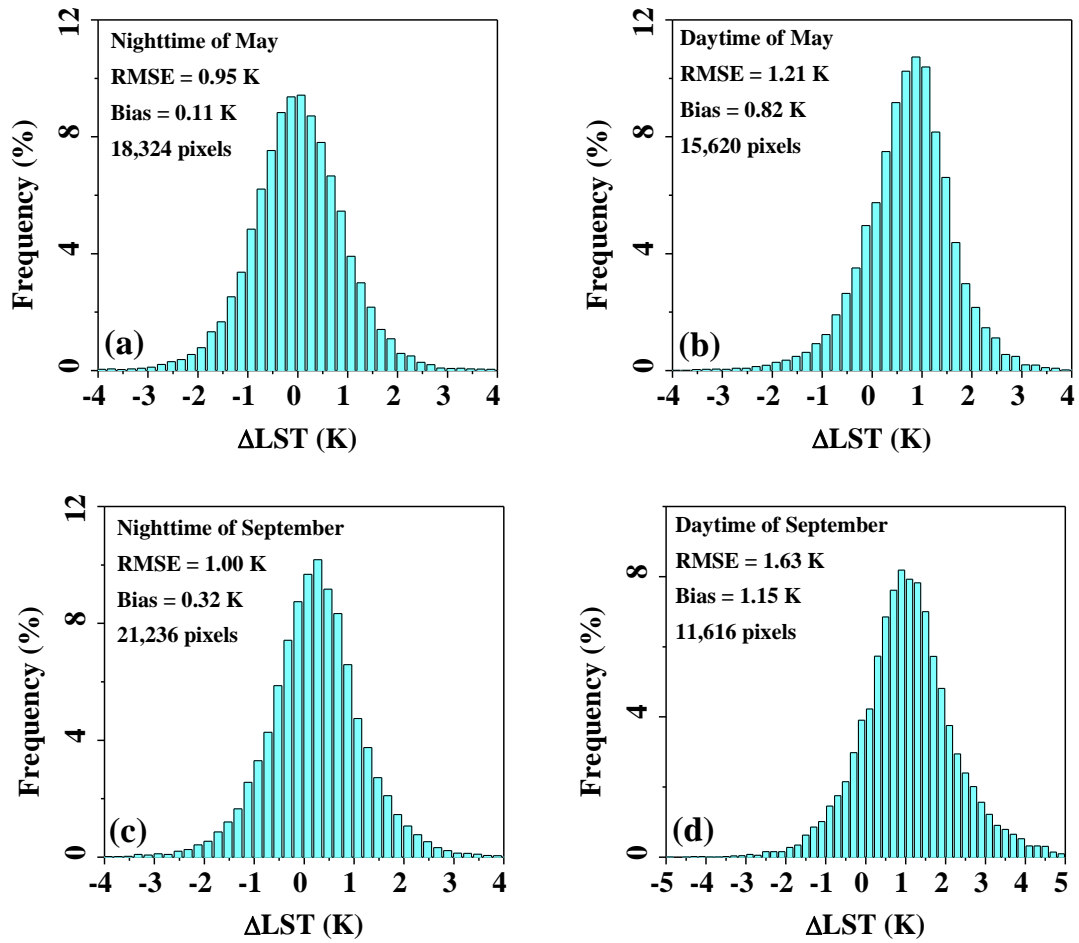
Fig. 4-18. Residual histograms of retrieved LST for observations of Australia acquired (a) at night in May 2018; (b) during the day in May 2018; (c) at night in September 2018; and (d) during the day in September 2018.
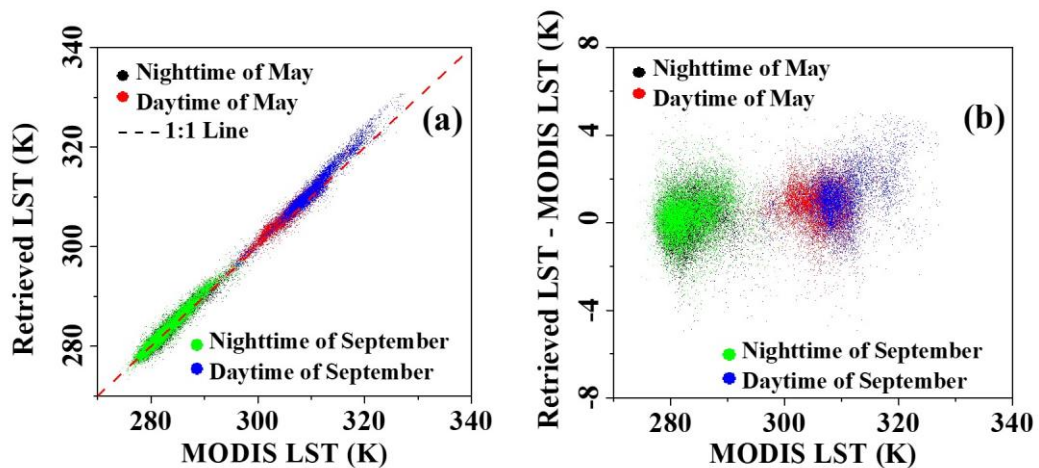
Fig. 4-19. (a) Scatter plot comparing the LSTs retrieved from AIRS using our proposed method and aggregated from the MODIS LST product. (b) Scatter plot of the LST difference (LST retrieved from AIRS - LST aggregated from MODIS LST product) versus the LST aggregated from the MODIS LST product.

4.6. Conclusions

Prior works have documented that the SW and TES algorithms are the two most widely used LST retrieval methods. However, the SW method requires accurate LSE information and the TES method requires accurate atmospheric correction. In this study, a procedure was proposed to find a new channel configuration in the TIR region, based on which ground brightness temperatures could be retrieved accurately by using a method similar to the SW method [Eq. 4-14]. Subsequently, the TES algorithm could be used to retrieve the LST without using additional atmosphere and LSE information. Finally, the proposed method and the suggested channel configuration were applied to the AIRS hyper-spectral radiance and validated by comparison with the MODIS LST product.

Results showed that the three ground brightness temperatures corresponding to 8.6 μm, 9.0 μm, and 10.4 μm could be acquired at an accuracy of about 0.65 K using the channel pairs of 8.6 μm and 12.5 μm, 9.0 μm and 12.5 μm, and 10.4 μm and 11.3 μm (width of 0.1 μm), respectively. The LST could be retrieved at an accuracy of within about 0.9 K using this TIR channel configuration. Sensitivity analyses indicated that the proposed method was not sensitive to channel FWHM and atmospheric downwelling radiance, but was sensitive to channel-center shifts and channel noise. When the channel centers shifted by -0.1 μm and -0.2 μm, the LST retrieval accuracy dropped to 1.5 K and 1.4 K, respectively. As the channel centers shifted to longer wavelengths, the LST retrieval accuracy dropped as well—to 1.1 K and 1.0 K with channel-center shifts of 0.1 μm and 0.2 μm, respectively. Moreover, when random noise was added to the channel brightness temperatures, LST retrieval accuracy decreased from 0.97 K to 1.43 K, along with an increase in channel noise from 0.1 K to 0.3 K. All these results indicate that the location of the channel center and channel noise must both be well controlled for good LST retrieval results.

In addition to analysis using a simulation dataset, the proposed method was also applied to real AIRS images. The retrieved LST was compared with the aggregated MODIS LST product, showing that the discrepancies between the retrieved result and the MODIS product were better for nighttime observations than for daytime observations, with LST retrieval RMSE of about 1.0 K and 1.6 K, respectively. Note that these discrepancies not only included the mismatch in retrieval methods, but also included the mismatch in observation time and angles. Additionally, when considering that the MODIS LST product itself contains an uncertainty of approximately 1.5 K, it is reasonable to conclude that the proposed method can be used to achieve LST retrievals that coincide with the MODIS

products.

Our findings indicate that the proposed method could be used to retrieve LST with high accuracy, based on the suggested TIR channel configuration. In comparison with the traditional SW and TES algorithms, the proposed method requires neither accurate LSE information nor precise atmospheric correction.

5 | Primary exploration on developing an improved LST retrieval method for high spatial resolution TIR measurements of urban areas

The temperature of urban areas is one of the most important parameters to study the urban environment. But according to chapter 2 and chapter 3, the adjacency effect and the impact of 3-D structures and their radiation both could make nonnegligible influences on the satellite TIR measurements which may deteriorate the performance of the current LST retrieval algorithms. Although efforts have already been made to assess or improve the urban LST retrieval accuracies, rare study considers both the adjacency effect and the impact of 3-D structures and their radiation in the urban LST retrievals. This chapter attempts to develop an improved method for accurate LST retrieval in urban areas from high spatial resolution satellite TIR measurements with consideration of these effect and impact. The above proposed FAERTM and ATIMOU are introduced as adequate tools to address the adjacency effect and the impact of 3-D structures and their radiation in the satellite TIR measurements, respectively. After combining with the PKF LST retrieval method proposed in chapter 4, an improved LST retrieval method for urban areas have been developed eventually. On the basis of simulated data, this improved LST retrieval method has been applied and evaluated preliminarily. Results show that an improvement of about 2.27 K could be achieved regarding to the RMSE of the retrieved LST, indicating the good performance of the proposed urban LST retrieval method.

5.1. Introduction

Urbanization is a crucial process of human civilization (Gu et al., 2012; Guo et al., 2019). Since cities always act as the center of a certain region in many spheres such as the population, administration, transportation, economy, education, culture, et. al, the stability of which is therefore very important for each country and even for the entire world (Gong et al., 2012). In urban areas, the environment has been transformed from natural surfaces to artificial ones, leading to the radiative behavior, hydrologic and aerodynamic characteristics of such areas all changed greatly, not only because of the different thermal properties of manmade materials, but also because of the 3-D structures of street canyons (Oke, 1987). Consequently, the natural balance regarding to energy, hydrology and other aspects in the urban areas may have been distorted (Oke, 1987; Qu, 2011). Thus, many environmental issues (e.g. urban heat island, air quality, water shortage and pollution, et. al.) arise along with the rapid urbanization process (Guo et al., 2019; Qu, 2011). These issues should be studied in detail and well addressed because more than half of the populations in the world live in the urban areas according to the Population Reference Bureau in 2019 (Bureau, 2019). As documented in previous researches, the temperature of urban areas is one of the most important parameters to study the urban environment (Jiang et al., 2018; Lau et al., 2016; Oltra-Carrio et al., 2014; Voogt and Oke, 1997). Comparing with the traditional ground-based method, thermal infrared remote sensing provides a better approach to acquire the urban LST (Jiang et al., 2018; Wang et al., 2018; Yang et al., 2020).

With the development of the thermal infrared remote sensing, the LST of the Earth surface nowadays could be obtained efficiently at regional and even global scales. Aiming at the specific features of different TIR measurements, enormous LST retrieval algorithms have been developed (Li et al., 2013a) and great successes have been achieved for natural flat surfaces using moderate/low spatial resolution TIR images. However, when trying to retrieve the LST of urban areas from high spatial resolution TIR measurements, there are still some limitations in the existing LST retrieval methods. First, the neglect of the adjacency effect (Duan et al., 2020; Zheng et al., 2019b); Second, the regardless of impact of 3-D structures and their radiation (Fontanilles et al., 2008; Oltra-Carrió et al., 2012; Oltra-Carrio et al., 2013; Zheng et al., 2020). Third, the dependence on the accurate atmospheric parameters and/or LSE information (Ren et al., 2020; Zheng et al., 2019a); Although efforts have already been made to assess or improve the urban LST retrieval accuracies (Jiang et al., 2018; Oltra-Carrió et al., 2012; Oltra-Carrio et al., 2013; Yang et al., 2020), studies that simultaneously consider the three mentioned factors influencing the

urban LST retrieval accuracy are rarely reported so far.

In this chapter, primary attempts have been made to explore an improved LST retrieval method for high spatial resolution TIR measurements of urban areas. Firstly, the PKF LST retrieval method (in chapter 4) has been applied to the urban TIR measurements directly to get the initial LST retrievals. Then, the FAERTM (in chapter 2) and ATIMOU (in chapter 3) have been combined with the PKF LST retrieval method to address the adjacency effect and the 3-D impacts, respectively. Lastly, with the help of an iteration process, the improved urban LST could finally be retrieved. This chapter is organized as follows: Section 5.2 demonstrates the methodology; Section 5.3 describes the simulated dataset; Section 5.4 presents and compares the LST retrieval results of the traditional TES algorithm and the proposed method; Section 5.5 summarizes the main findings.

5.2. Methodology

For those moderate or low spatial resolution TIR images of natural flat surfaces, there is no impact of 3-D structures and their radiation and the adjacency effect is also negligible based on the studies in previous chapters. However, in urban areas, especially for high spatial resolution TIR observations, the adjacency effect and the impact of 3-D structures and their radiation both could influence the satellite TIR measurements (Zheng et al., 2020; Zheng et al., 2019b). On the basis of the traditional TIR radiative transfer theory, FAERTM (Eq. 2-2 in chapter 2), and the ATIMOU (Eq. 3-14 in chapter 3), the satellite observed TIR radiance in urban areas could be expressed by:

$$L^{TOA\_Ubn} = B\left(T^{TOA\_Ubn}\right) = \tau L^{BOA\_Ubn} + L_\uparrow + L_1 + RAD \qquad \text{Eq. 5-1}$$

in which

$$RAD = \tau\left(1-\varepsilon\right)\frac{L_2}{1-\rho S} \qquad \text{Eq. 5-2}$$

where L^{TOA_Ubn} and T^{TOA_Ubn} are respectively the satellite observed radiance and effective brightness temperature of the target pixel in urban areas at top of atmosphere (TOA) level; τ is the direct atmospheric transmittance; L^{BOA_Ubn} is the ground observed radiance of the target pixel in urban areas at bottom of atmosphere (BOA) level which can be obtained according to Eq. 3-30 in chapter 3; $L_\uparrow$ is the atmospheric upwelling radiance; L_1 is the single scattered adjacent pixel radiance at TOA level which can be obtained according to Eq. 2-10 in chapter 2; RAD is the target-reflected ground radiance at TOA

level which can be obtained according to Eq. 2-17 in chapter 2; ε is the emissivity of the target pixel in urban areas; L_2 is the radiance emitted from the ground and reflected by the atmosphere; ρ is the reflectance of the ground; and S is the atmospheric spherical albedo at the BOA level.

To retrieve the accurate LST of urban areas from high spatial resolution TIR measurements, the adjacency effect ($L_1 + RAD$) and the impact of 3-D structures and their radiation in the item of L^{BOA_Ubn} both should be corrected during the LST retrieval. Fortunately, the FAERTM and ATIMOU provide two very useful tools, on the basis of which and together with the PKF LST retrieval method proposed in chapter 4, an improved LST retrieval method designed for high spatial resolution TIR measurements of urban areas is proposed. The overall scheme design is shown in Fig. 5-1 as below:
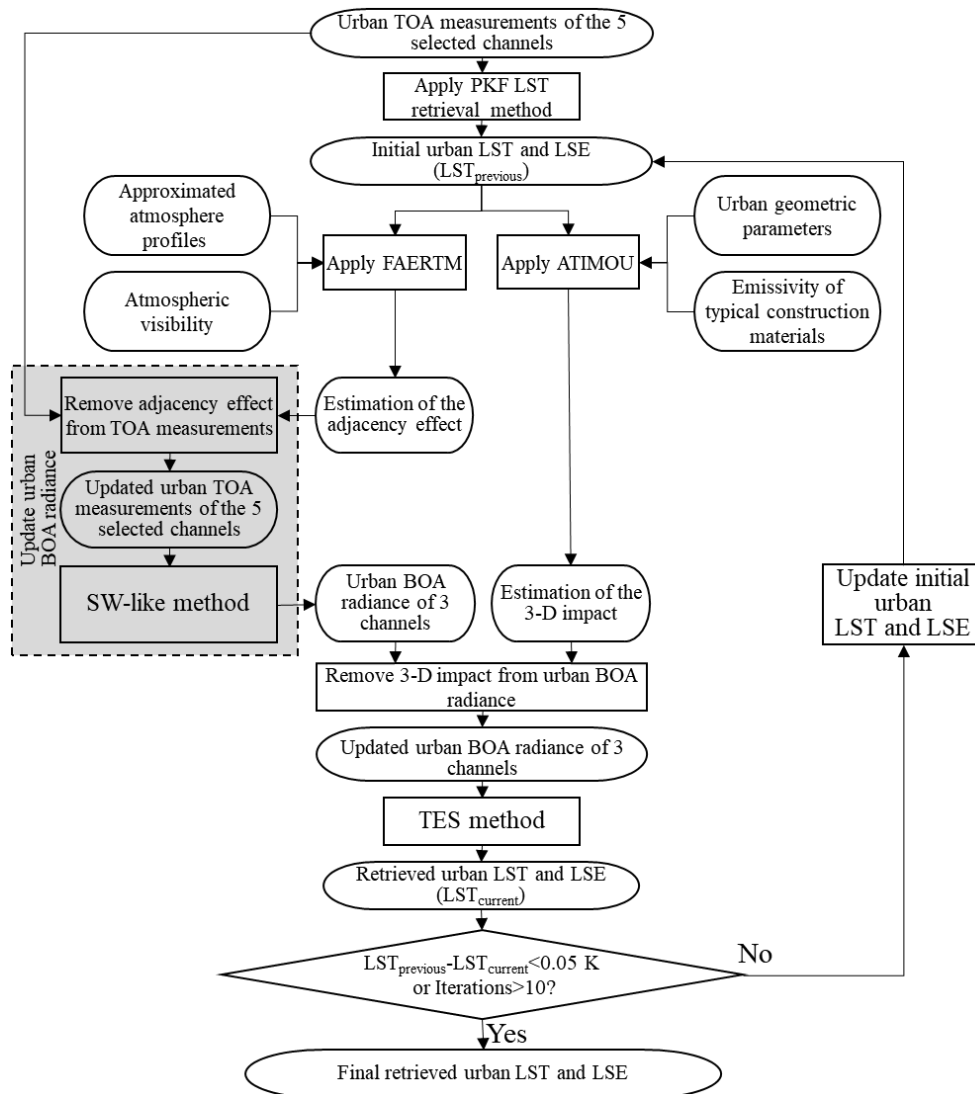
Fig. 5-1. Overall scheme design of the improved LST retrieval method for high spatial resolution TIR measurements of urban areas

In fact, correction of the adjacency effect and the 3-D impact requires the urban LST and LSE that are to be retrieved. Thus, an iterative strategy has been used to remove the adjacency effect and the 3-D impact from the measurements and to refine the final Urban LST and LSE retrievals. The detailed implementation of this method is described as below:

Step 1: Obtain the initial urban LST ($LST_{previous}$) and LSE by applying the PKF LST retrieval method to the urban TOA measurements directly without any corrections.

Step 2: Estimate the adjacent effect using the FAERTM and the initial urban LST and LSE obtained in Step 1. Additionally, the atmospheric visibility and profile are also necessary inputs in the FAERTM. The former can be obtained from existing measurements or products. The latter can be obtained from some approximated information, such as the MODIS retrievals and the 6 standard atmospheres embedded in the MODTRAN model, which should be sufficient for the estimation of the adjacency effect.

Step 3: Remove the adjacency effect from the urban TOA measurements and retrieve the urban BOA radiance using the SW-like method (Eq. 4-14).

Step 4: Estimate the 3-D impact using the ATIMOU and the initial urban LST and LSE obtained in Step 1. The required geometric parameters and optical properties of the building walls are assumed to be known in advance according to ground surveys.

Step 5: Remove the 3-D impact from the urban BOA radiance obtained in Step 3 and obtain the updated urban BOA radiance.

Step 6: Retrieve the urban LST ($LST_{current}$) and LSE using the traditional TES method.

Step 7: Compare $LST_{previous}$ and $LST_{current}$. If the difference is >0.05 K, then update the initial urban LST and LSE as the current retrievals and go to Step 1 for next iteration. Otherwise, if the difference is <0.05 K or the iterations >10, then stop iteration and output the current retrievals as the final retrieved urban LST and LSE.

5.3. Simulation description

To preliminarily investigate the performance of the proposed LST retrieval method for urban areas, simulated high spatial resolution TIR measurements of urban areas have been made firstly on the basis of Eq. 5-1.

The street canyon shown in Fig. 3-1 in chapter 3 has been duplicated horizontally and vertically to generate the simulated urban scenario. For simplicity, the wall height and road

width have been set as fixed values of 20 m and 10 m, respectively. It is also assumed that the ground has been observed vertically and the center of the sensor's IFOV is located at the center of the road with the width of 10 m, implying the target pixel has been filled only with the road.

Previous studies show that the empirical relationship between minimum emissivity (ε_{min}) and the maximum-minimum emissivity difference (MMD) is an important factor influencing the performance of the TES algorithm. This relationship has been proven to be stable for natural land surfaces but is not applicable to metal surfaces (Gillespie et al., 1998; Payan and Royer, 2004). Therefore, all the metals and the samples with metals (such as some spray, paint, et. al.) should be excluded when building the $\varepsilon_{min} \sim MMD$ empirical relationship. In this chapter, the LSE spectra of six roofing material samples (Fig. 5-2a), eight paving material samples (Fig. 5-2b), and 18 construction material samples (Fig. 5-2c) from the ECOSTRESS Spectral Library, Version 1.0 (https://speclib.jpl.nasa.gov/) have been introduced to respectively represent different kinds of roof, road, and wall in the street canyon finally. Additionally, the six standard atmosphere profiles in the MODTRAN model with the water vaper content ranging from 0.42 g/cm^2 to 4.11 g/cm^2 have been used to represent different atmospheric conditions (Fig. 5-2d). The LST of roof, road, and wall have been assigned varying from T_0-10 K to T_0+20 K with the interval of 10 K, in which T_0 is the bottom layer temperature of each atmosphere profile. With the input parameters described above, 331,776 cases have been generated using Eq. 5-1 in the simulation dataset.
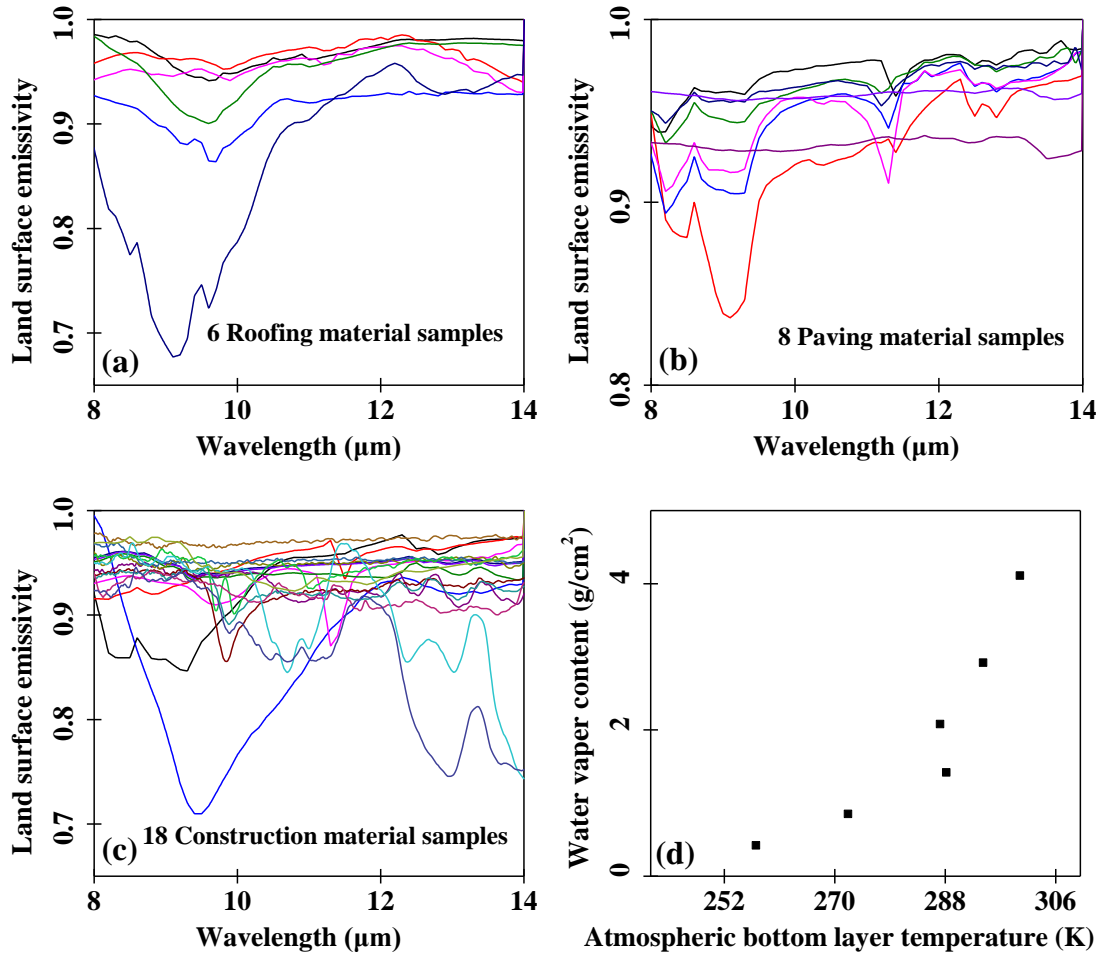
Fig. 5-2. (a) LSE spectra of the six roofing material samples, (b) LSE spectra of the eight paving material samples, (c) LSE spectra of the 18 construction material samples, and (d) scatter plot of the bottom layer temperature and water vaper content of the 6 standard atmosphere profiles in MODTRAN model.

5.4. Results

5.4.1. LST retrieval results using traditional TES algorithm

Before implementing the proposed LST retrieval method, the traditional TES algorithm has been applied to provide referenced results. The empirical relationship of $\varepsilon_{min} \sim MMD$ has been obtained on the basis of the mentioned 32 manmade samples (Fig. 5-3a). It is shown that the error introduced in the reproduced LSE using this empirical relationship becomes larger for manmade samples with an RMSE of 0.017, comparing with an RMSE of 0.006 for the 65 natural surface samples illustrated in Fig. 4-7a. After inputting the simulated BOA radiance of target pixel ($L^{BOA-Ubn}$) and the accurate atmospheric downwelling radiance, the LST of target pixel could be retrieved with an RMSE of 1.74 K (Fig. 5-3b). Nevertheless, it should be noticed that the error in the retrieved LST is not only

because of the $\varepsilon_{min} \sim MMD$ relationship, but also because of the impact of 3-D structures and their radiation on the measured BOA radiance of target pixel ($L^{BOA-Ubn}$). Additionally, the radiance from 3-D surroundings is generally larger than the atmospheric downwelling radiance. Thus, the BOA radiance of target pixel has been overestimated, leading to the overestimation of the retrieved LST as confirmed by the positive bias 1.62 K (Fig. 5-3b). However, if the impact of 3-D structures and their radiation on the BOA radiance of the target pixel has been well addressed before applying the TES algorithm, the LST retrieval accuracy could be improved significantly with an RMSE of 0.86 K and a bias of 0.22 K representing the intrinsic error of the TES algorithm itself in urban areas (Fig. 5-3c).
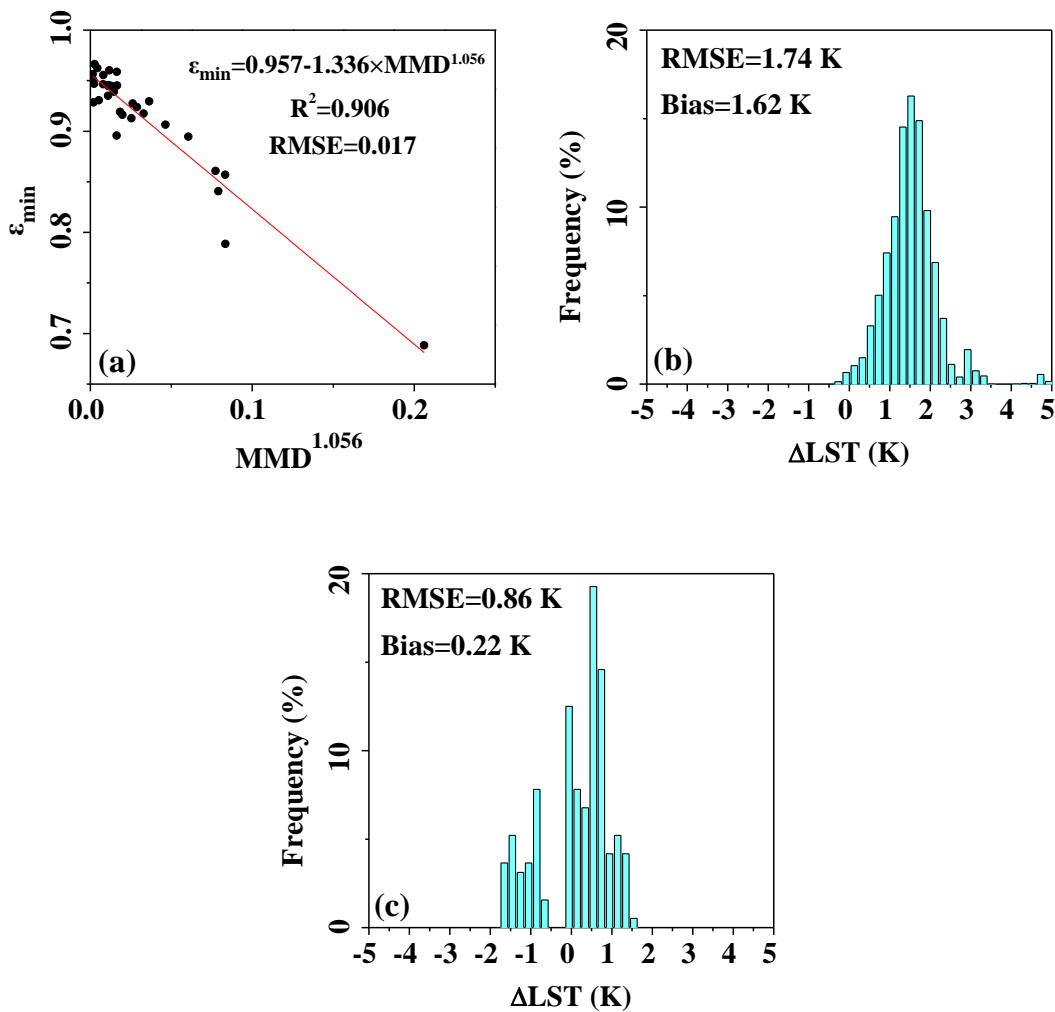
Fig. 5-3. (a) The empirical relationship between ε_{min} and MMD, based on the 32 samples described in Section 5.3. (b) Histogram of the residuals between the retrieved and true LSTs, in which the retrieved LSTs have been obtained based on the BOA radiance of the target pixel without correcting the impact of 3-D structures and their radiation. (c) Same as (b) except that the impact of 3-D structures and their radiation on the BOA radiance of the target pixel has been well addressed before retrieving the LSTs.

5.4.2. LST retrieval results using the proposed method

When applying the PKF LST retrieval method directly to the urban TOA measurements, the initial urban LST ($LST_{previous}$) could be obtained. Since both adjacency effect and 3-D impacts have not been corrected at this stage, a large positive bias of 3.15 K has been introduced to the retrieved LST leading to the bad LST retrieval accuracy with a RMSE of 3.33 K (Fig. 5-4a). However, if following the method proposed in Section 5.2, the adjacency effect and the impact of 3-D structures and their radiation could both be well addressed after several iterations. Results show that the overestimations in the final LST retrievals has been greatly suppressed. The RMSE of the retrieved LST also decreases significantly to 1.06 K, which is comparable to the intrinsic accuracy of the TES algorithm in urban areas (Fig. 5-3c).
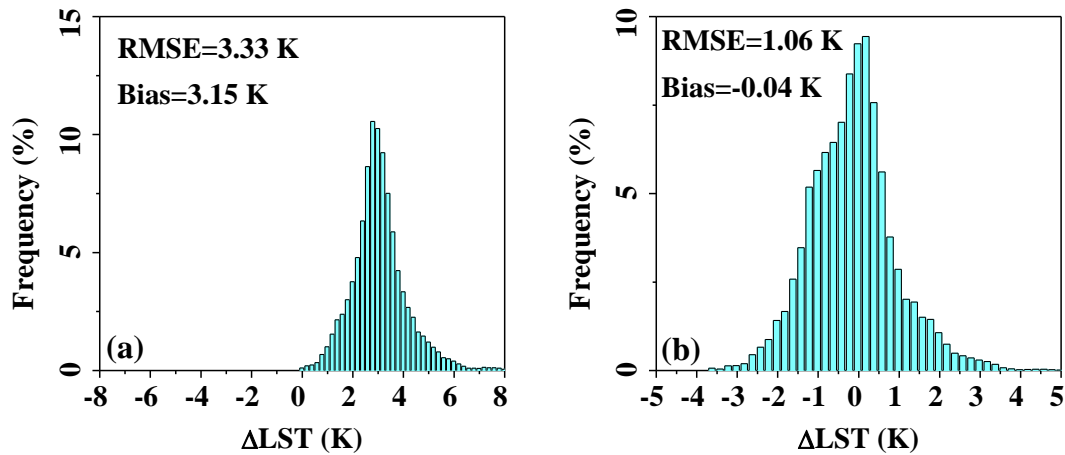
Fig. 5-4. Histogram of the residuals regarding to (a) the initial urban LST retrievals obtained by applying the PKF LST retrieval method directly to the urban TOA measurements, and (b) the final urban LST retrievals obtained by implementing the method proposed in Section 5.2.

To investigate how much uncertainties have been introduced to the final LST retrievals by the adjacency effect and the 3-D impacts separately. The proposed LST retrieval method has been applied to the urban TOA measurements again, but instead of correcting both adjacency effect and 3-D impacts during the iterations, only one of them has been taken into consideration each time. It is shown that a RMSE of 2.10 K regarding to the final LST retrievals could be obtained if the adjacency effect has been considered in the proposed LST retrieval method but neglecting the correction of the 3-D impacts (Fig. 5-5a). On the contrary, consideration of the 3-D impacts while ignoring the correction of adjacency effect in the proposed LST retrieval method has led to a RMSE of 1.69 K regarding to the final

LST retrievals (Fig. 5-5b). The results also indicate that both adjacency effect and 3-D impacts could introduce nonnegligible errors to the final LST retrievals. Moreover, the bias introduced to the final LST retrievals resulting from the 3-D impacts is slightly larger than that resulting from the adjacency effect.
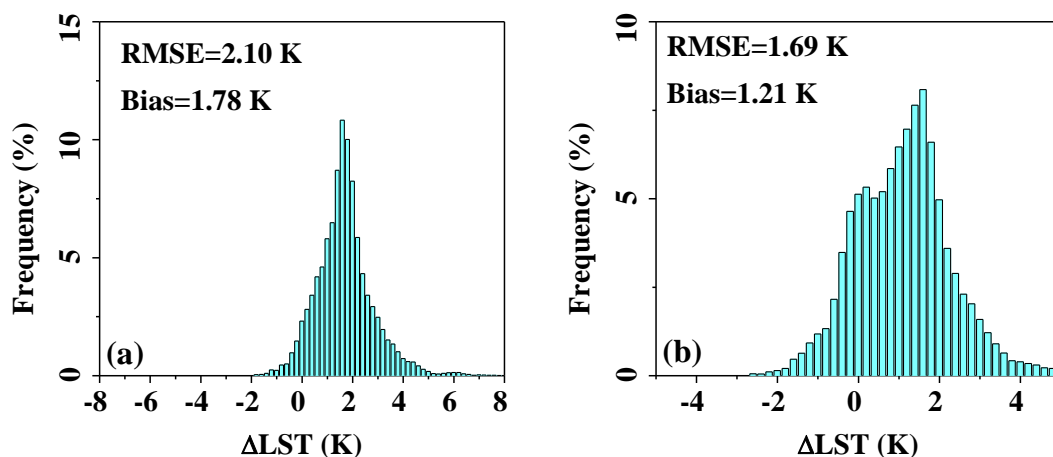
Fig. 5-5. Histogram of the residuals regarding to (a) the final urban LST retrievals obtained by implementing the proposed method with correction of the adjacency effect but without correction of the 3-D impacts, and (b) the final urban LST retrievals obtained by implementing the proposed method without correction of the adjacency effect but with correction of the 3-D impacts.

5.5. Conclusions

To our knowledge, neither adjacency effect nor 3-D impacts have been considered in the currently most commonly used LST retrieval algorithms (e.g. SW and TES algorithm). For moderate/low spatial resolution TIR images or regarding to the natural flat surfaces, regardless of the adjacency effect and 3-D impacts perhaps would have no significant influence on the final LST retrieval accuracy. However, if the spatial resolution of TIR images improves or regarding to the ragged terrain such as urban areas, the influences resulting from the adjacency effect and the 3-D impacts would become larger. Thus, the performance of the currently existing LST retrieval algorithms may be deteriorated under such circumstances. In this chapter, a primary exploration has been provided on developing an improved LST retrieval method for high spatial resolution TIR measurements of urban areas in which both adjacency effect and 3-D impacts have been considered.

Simulated results show that the performance of the PKF LST retrieval method could be significantly influenced by the adjacency effect and the 3-D impacts for the high spatial

resolution TIR measurements of urban areas with the LST retrieval RMSE of 3.33 K. The proposed LST retrieval method for urban areas, in which an iterative process has been used to address the adjacency effect and the 3-D impacts, has the ability of improving the final LST retrieval accuracy. Simulations show that the RMSE of the retrieved LST decreased to 1.06 K after implementing the proposed method, which is comparable to the intrinsic accuracy of the TES algorithm in urban areas with the LST retrieval RMSE of 0.86 K. Moreover, the uncertainties introduced to the final LST retrievals regarding to the adjacency effect or the 3-D impacts have also been separately investigated. Results show that regardless of the adjacency effect in the proposed LST retrieval method could result in the LST retrieval RMSE increasing from 1.06 K to 1.69 K, while the LST retrieval RMSE increases from 1.06 K to 2.10 K if the 3-D impacts has been neglected. This indicates that both adjacency effect and 3-D impacts should be considered when retrieving the urban LST from high spatial resolution TIR measurements.

Nevertheless, this chapter only provides a primary exploration on developing an improved LST retrieval method for high spatial resolution TIR measurements of urban areas. More scenarios are planned to be introduced to study the performance of the proposed method further. Besides, field experiments in urban areas are also desired to validate the absolute accuracy of the retrieved LSTs in detail.

6 | Conclusions and perspectives

6.1. Conclusions

Although many LST retrieval algorithms have already been developed over the last decades and achieved great success in generating global LST products (Becker and Li, 1990; Wan, 2014; Wan and Dozier, 1996), there still exist limitations in these algorithms especially for the cases regarding to accurate LST retrieval from high spatial resolution satellite TIR measurements of urban areas. To my knowledge, existing LST retrieval algorithms have been developed regardless of the adjacency effect which may introduce additional biases to the retrieved LST from high spatial resolution satellite TIR measurements. The impact of 3-D structures and their radiation existed in urban areas has also not been considered in these existing LST retrieval algorithms. Moreover, the accurate atmospheric parameters and/or LSE are demanded by these existing LST retrieval algorithms, leading to the LST retrieval accuracy dependent on the uncertainties of the prior knowledge. Therefore, this thesis concentrates on the development of an improved LST retrieval method aiming at improving the LST retrieval accuracy in urban areas from high spatial resolution satellite TIR measurements. Compared with existing LST retrieval algorithms, the main progresses made in the proposed method could be generalized as three points: (1) the correction of the adjacency effect, (2) the correction of the impact of 3-D structures and their radiation on the TIR measurements, and (3) the less dependence on the accurate prior knowledge of atmospheric and surface parameters during LST retrieval. The corresponding researches involved in each point have been well investigated in three respective chapters, on the basis of which, the final explorations have been made on developing the improved LST retrieval method for high spatial resolution TIR measurements of urban areas.

In chapter 2, aiming at the first specific objective, a physical adjacency effect simulation model, FAERTM, has been developed and used to quantify the adjacency effect on TIR measurements for different atmospheric and imaging conditions. It is show that the adjacency effect mainly originates from pixels within 3 km of the target and is not sensitive to aerosol type and LSE. Additionally, in contrast to scenarios with clear atmospheres,

coarse image spatial resolution, and cold adjacent pixels, adjacency effect magnitude increases with a decrease in atmospheric visibility, an improvement in image spatial resolution, or an increase in adjacent pixel radiation. In extreme conditions, the adjacency effect magnitude may even exceed 3.0 K. It is also shown that, as wavelength increased, the adjacency effect generally decreases, except at 8 μm; at this wavelength, atmospheric transmittance and aerosol scattering optical depth are both quite small, leading to most adjacency effect radiance being absorbed and thus not being observed by the sensor. These findings clearly show that the adjacency effect should be considered in the TIR region, at least for some specific cases, such as the atmospheric visibility is smaller than 23 km or the image spatial resolution is higher than 1.0 km. Otherwise, significant underestimations would be introduced to the satellite TIR measurements. For the purpose of further improving LST retrieval accuracy, the adjacency effect should either be independently addressed from TIR signals before applying commonly used LST retrieval algorithms or should be integrated into existing LST retrieval algorithms to develop new ones. The proposed FAERTM could serve as a very useful tool for both approaches.

In chapter 3, aiming at the second specific objective, a new analytical TIR radiative transfer model (ATIMOU), that considers the impact of 3-D structures and their radiation on TIR measurements, has been developed. On the basis of this model, the impact of 3-D structures and their radiation on the TIR measurements over a street canyon has been quantitatively evaluated under different viewing angles after accounting for obstructions caused by walls of buildings. It is shown that the magnitude of the impact of 3-D structures and their radiation on satellite TIR measurements is different under different atmospheric types. Generally, the magnitude of the impact of 3-D structures and their radiation in a hot, humid atmosphere is smaller than that in a cold, dry atmosphere, and is believed to be caused by the variation of atmospheric transmittance. It is also shown that the impact of 3-D structures and their radiation is always largest at nadir, because the IFOV may be partly, and even entirely, filled with building roofs as the viewing zenith angle increases. However, the building roofs are not affected by the radiation of the 3-D structures. Moreover, increasing H/W, decreasing road emissivity, and increasing wall temperature could all increase the magnitude of the impact of 3-D structures and their radiation on a TIR measurement, according to the simulations. Besides, the radiation from a building wall is the primary cause of the impact of 3-D structures and their radiation on TIR measurement compared with that from the atmosphere. However, if road emissivity is low, both contributions from the building wall and from the atmosphere cannot be ignored. Under

both circumstances, the proposed ATIMOU provides a convenient tool to address the impact of 3-D structures and their radiation during the urban LST retrieval.

In chapter 4, aiming at the third specific objective, a procedure has been proposed firstly to find a new channel configuration in the TIR region. On the basis of this TIR channel configuration and the two most widely used LST retrieval methods (SW and TES), a prior-knowledge-free (PKF) method has been developed which could be used to retrieve LST accurately without using additional atmosphere and LSE information. According to simulations, the three ground brightness temperatures corresponding to 8.6 μm, 9.0 μm, and 10.4 μm could be acquired at an accuracy of about 0.65 K using the channel pairs of 8.6 μm and 12.5 μm, 9.0 μm and 12.5 μm, and 10.4 μm and 11.3 μm (width of 0.1 μm), respectively. The LST could be retrieved at an accuracy of within about 0.9 K using this TIR channel configuration. When applying the proposed method to the real AIRS images and comparing to the MODIS LST product, it is shown that the discrepancies between the retrieved result and the MODIS product are better for nighttime observations than for daytime observations, with the LST retrieval RMSE of about 1.0 K and 1.6 K, respectively. These findings indicate that the proposed PKF LST retrieval method could be used to retrieve LST with high accuracy, based on the suggested TIR channel configuration. In comparison with the traditional SW and TES algorithms, the proposed PKF LST retrieval method requires neither accurate LSE information nor precise atmospheric correction.

In chapter 5, aiming at the fourth specific objective, a primary exploration has been provided on developing an improved LST retrieval method for high spatial resolution TIR measurements of urban areas. Specifically, both adjacency effect and the impact of 3-D structures and their radiation have been considered into the PKF LST retrieval method proposed in chapter 4 to improve the urban LST retrieval accuracy from high spatial resolution satellite TIR measurements. Simulated results show that the improved LST retrieval method proposed in this chapter, in which an iterative process has been used to address the adjacency effect and the impact of 3-D structures and their radiation, has the ability of improving the urban LST retrieval accuracy from high spatial resolution satellite TIR measurements. It is shown that the urban LST could be retrieved with an RMSE of about 3.33 K when applying the PKF LST retrieval method directly to the satellite TIR measurements. After implementing the proposed method, the RMSE of the retrieved LST decreased to 1.06 K, which is comparable to the intrinsic accuracy of the TES algorithm in urban areas with the LST retrieval RMSE of 0.86 K. It is also shown that the regardless of the adjacency effect in the proposed LST retrieval method could result in the LST retrieval

RMSE decreasing from 1.06 K to 1.69 K, while the LST retrieval RMSE decreases from 1.06 K to 2.10 K if the impact of 3-D structures and their radiation has been neglected. This indicates that both adjacency effect and the impact of 3-D structures and their radiation should be considered and well addressed when retrieving the urban LST from high spatial resolution satellite TIR measurements. Furthermore, it can be concluded that the researches conducted in this thesis provide a very practical approach for accurate urban LST retrieval.

6.2. Perspectives

This thesis has investigated the factors influencing the satellite TIR measurements and the LST retrieval accuracy, based on which, a primary exploration has been provided on developing an improved urban LST retrieval method for high spatial resolution satellite TIR measurements. Nevertheless, the study still poses limitations and requires some additional researches in the future.

(1) In FAERTM, the nadir observations have been assumed for simplification. Besides, the atmosphere has also been assumed to be horizontally uniform. Then, for the adjacent pixels that have identical distance from the target pixel, their optical paths of the radiative transfer process are all the same, leading to the same contribution of adjacency effect on the satellite measurements. But if the satellite observations have been taken obliquely, the situations will be different. Under such cases, the radiation emitted from the adjacent pixels on the near side of the sensor will have shorter optical paths but larger scattering angles than those adjacent pixels with same distance from target pixel but on the far side of the sensor. Therefore, the contribution of each adjacent pixel on the satellite measurements needs to be studied further.

(2) In ATIMOU, a symmetric scenario with two equal-height buildings has been used for simplification. However, the two buildings may have different heights in actual canopies. For such cases, there exists energy exchange between the lower building roof and the opposite building wall, leading to the irradiance above the lower building roof dependent on the urban 3-D geometry. Consequently, the current equation system describing the energy conservation inside the street canyon (Eq. 3-7 ~ Eq. 3-10) would be affected by the building roof provided that the heights of the two buildings are different. If this asymmetric street canyon has been considered as the combination of one symmetric street canyon similar to Fig. 3-1. and an extra building on top of one building roof, the energy exchange inside the asymmetric street canyon then could be modelled. Besides, the temperature

differences between the sunlit and shadowed areas during daytime currently has been modeled by using the concept of "effective brightness temperature". More equations are planned to be introduced to take the influence caused by the solar loadings into consideration. The corresponding derivations will be managed in our future work to improve the proposed ATIMOU.

(3) In reference to the PKF LST retrieval method, there are presently no TIR sensors with such a channel configuration. Therefore, the method has only been verified based on simulated channel filter functions. It is planned to collect and combine actual channel filter functions from several operational TIR sensors in the future in order to generate a more practical simulation dataset, based on which the proposed method will be further evaluated. Additionally, the coefficients in the SW-like equation are only applicable to vertical observations. The viewing angles have not been considered yet. Besides, similar to the improvement made to the SW method, the retrieval accuracy for ground brightness temperatures may improve if they are considered as a function of atmospheric water vaper content or using multi-channel observations. Therefore, efforts are needed to improve the performance of the PKF LST retrieval method further in the future and an intercomparison experiment with the MODIS LST product in the global scale is under planning.

(4) As to the improved LST retrieval method for high spatial resolution satellite TIR measurements of urban areas, only a primary exploration has been provided. The atmospheric profiles and street canyon scenarios used to make the simulation dataset are very limited. More simulated experiments are needed to study the performance of the improved LST retrieval method further. Besides, the cases regarding to oblique observations should also be considered and investigated, in which the building walls will also contribute to the sensor's IFOV directly. Moreover, efforts should be made to develop new LST retrieval methods with considering the adjacency effect and 3-D impacts in theory. In addition, instead of staying at the simulation stage, actual satellite measurements and field experiments in urban areas are desired to validate the absolute accuracy of the final urban LST retrievals in detail.

Related publications

Journal papers:

X. Zheng, Z.-L. Li, F. Nerry, and X. Zhang, "A new thermal infrared channel configuration for accurate land surface temperature retrieval from satellite data," Remote Sensing of Environment, vol. 231, no. (2019) 111216, pp. 1-12, May 2019.

X. Zheng, Z.-L. Li, X. Zhang, and G. Shang, "Quantification of the adjacency effect on measurements in the thermal infrared region," IEEE Transactions on Geoscience and Remote Sensing, vol. 57, no. 12, pp. 9674-9687, Jul. 2019.

X. Zheng, M. Gao, Z.-L. Li, K.-S. Chen, X. Zhang, and G. Shang, "Impact of 3-d structures and their radiation on thermal infrared measurements in urban areas," IEEE Transactions on Geoscience and Remote Sensing, vol. Early Access, no. Early Access, pp. 1-15, May 2020.

Conference proceedings:

X. Zheng, Z.-L. Li, K.-S. Chen, X. Zhang, and G. Shang (2019). Assessment of the urban three-dimensional structural influence on the satellite thermal infrared measurement. In, *IEEE PhotonIcs & Electromagnetics Research Symposium – Spring* (pp. 377-386), Rome, Italy: IEEE.

Related publications

References

Adler-Golden, S.M., Conforti, P., Gagnon, M., Tremblay, P., & Chamberland, M. (2014). Long-wave infrared surface reflectance spectra retrieved from Telops Hyper-Cam imagery. In, *Proc. SPIE 9088, Algorithms and Technologies for Multispectral, Hyperspectral, and Ultraspectral Imagery XX* (pp. 1-8). Baltimore, Maryland, United States: SPIE.

Anderson, M.C., Norman, J.M., Kustas, W.P., Houborg, R., Starks, P.J., & Agam, N. (2008). A thermal-based remote sensing technique for routine mapping of land-surface carbon, water and energy fluxes from field to regional scales. *Remote Sensing of Environment, 112*, 4227-4241.

Ångström, A. (1929). On the atmospheric transmission of sun radiation and on dust in the air. *Geografiska Annaler, 11*, 156-166.

Baghdadi, N., & Zribi, M. (2016). *Land surface remote sensing in urban and coastal areas*. Elsevier.

Becker, F. (1987). The impact of spectral emissivity on the measurement of land surface-temperature from a satellite. *International Journal of Remote Sensing, 8*, 1509-1522.

Becker, F., & Li, Z.-L. (1990). Towards a local split window method over land surfaces. *International Journal of Remote Sensing, 11*, 369-393.

Becker, F., & Li, Z.-L. (1995). Surface temperature and emissivity at various scales: Definition, measurement and related problems. *Remote Sensing Reviews, 12*, 225-253.

Berk, A., Anderson, G., Acharya, P., & Shettle, E. (2008). MODTRAN 5 user's manual. In Hanscom AFB, MA, USA: Air Force Research Laboratory Space Vehicles Directorate.

Berk, A., Anderson, G.P., Acharya, P.K., Bernstein, L.S., Muratov, L., Lee, J., Fox, M., Adler-Golden, S.M., Chetwynd, J.H., Hoke, M.L., Lockwood, R.B., Cooley, T.W., & Gardner, J.A. (2005). MODTRAN5: A reformulated atmospheric band model with auxiliary species and practical multiple scattering options. In, *Proc. SPIE 5655, Multispectral and Hyperspectral Remote Sensing Instruments and Applications II* (pp. 88-95). Honolulu, Hawai'i, United States: SPIE.

Berk, A., Anderson, G.P., Acharya, P.K., Bernstein, L.S., Muratov, L., Lee, J., Fox, M., Adler-Golden, S.M., Chetwynd, J.H., Hoke, M.L., Lockwood, R.B., Gardner, J.A., Cooley, T.W., Borel, C.C., Lewis, P.E., & Shettle, E.P. (2006). MODTRAN5: 2006 update. In, *SPIE 6233, Algorithms and Technologies for Multispectral, Hyperspectral, and Ultraspectral Imagery XII* (pp. 1-8). Orlando (Kissimmee), Florida, United States: SPIE.

Berk, A., Cooley, T.W., Anderson, G.P., Acharya, P.K., Bernstein, L.S., Muratov, L., Lee, J., Fox, M., Adler-Golden, S.M., Chetwynd, J.H., Hoke, M.L., Lockwood, R.B., Gardner, J.A., & Lewis, P.E. (2004). MODTRAN5: A reformulated atmospheric band model with auxiliary species and practical multiple scattering options. In, *Proc. SPIE 5571, Remote Sensing of Clouds and the Atmosphere IX* (pp. 78-85). Maspalomas, Canary Islands, Spain: SPIE.

References

Burazerovic, D., Heylen, R., Geens, B., Sterckx, S., & Scheunders, P. (2013). Detecting the adjacency effect in hyperspectral imagery with spectral unmixing techniques. *IEEE Journal of Selected Topics in Applied Earth Observations and Remote Sensing, 6*, 1070-1078.

Bureau, P.R. (2019). 2019 world population data sheet

Caselles, V., & Sobrino, J.A. (1989). Determination of frosts in orange groves from NOAA-9 AVHRR data. *Remote Sensing of Environment, 29*, 135-146.

Chedin, A., Scott, N.A., & Berroir, A. (1982). A single-channel, double-viewing angle method for sea-surface temperature determination from coincident meteosat and Tiros-N radiometric measurements. *Journal of Applied Meteorology, 21*, 613-618.

Chen, Y., Duan, S.-B., Ren, H., Labed, J., & Li, Z.-L. (2017). Algorithm development for land surface temperature retrieval: Application to chinese gaofen-5 data. *Remote Sensing, 9*, 1-19.

Choudhury, B.J., Schmugge, T.J., Chang, A., & Newton, R.W. (1979). Effect of surface roughness on the microwave emission from soils. *Journal of Geophysical Research, 84*, 5699-5706.

Choudhury, B.J., Schmugge, T.J., & Mo, T. (1982). A parameterization of effective soil temperature for microwave emission. *Journal of Geophysical Research, 87*, 1301-1304.

Cimini, D., Frank, S., & Visconti, G. (2010). Principles of radiometric remote sensing of the troposphere. *Integrated ground-based observing systems* (pp. 3-32). Berlin, German: Springer-Verlag Berlin Heidelberg.

Clough, S.A., Iacono, M.J., & Moncet, J.L. (1992). Line-by-line calculations of atmospheric fluxes and cooling rates - application to water-vapor. *Journal of Geophysical Research-Atmospheres, 97*, 15761-15785.

Coll, C., & Caselles, V. (1997). A split-window algorithm for land surface temperature from advanced very high resolution radiometer data: Validation and algorithm comparison. *Journal of Geophysical Research-Atmospheres, 102*, 16697-16713.

Coll, C., Caselles, V., Sobrino, J.A., & Valor, E. (1994). On the atmospheric dependence of the split-window equation for land surface temperature. *International Journal of Remote Sensing, 15*, 105-122.

Cook, M., Schott, J., Mandel, J., & Raqueno, N. (2014). Development of an operational calibration methodology for the Landsat thermal data archive and initial testing of the atmospheric compensation component of a land surface temperature (lst) product from the archive. *Remote Sensing, 6*, 11244-11266.

Dash, P., Göttsche, F.-M., Olesen, F.-S., & Fischer, H. (2001). Retrieval of land surface temperature and emissivity from satellite data: Physics, theoretical limitations and current methods. *Journal of the Indian Society of Remote Sensing, 29*, 23-30.

Dash, P., Göttsche, F.-M., Olesen, F.S., & Fischer, H. (2002). Land surface temperature and emissivity estimation from passive sensor data: Theory and practice-current trends. *International Journal of Remote Sensing, 23*, 2563-2594.

References

Du, C., Ren, H., Qin, Q., Meng, J., & Zhao, S. (2015). A practical split-window algorithm for estimating land surface temperature from Landsat 8 data. *Remote Sensing, 7*, 647-665.

Duan, S.-B., Li, Z.-L., Gao, C., Zhao, W., Wu, H., Qian, Y., Leng, P., & Gao, M. (2020). Influence of adjacency effect on high-spatial-resolution thermal infrared imagery: Implication for radiative transfer simulation and land surface temperature retrieval. *Remote Sensing of Environment, 245*, 111852.

Duan, S.-B., Li, Z.-L., & Leng, P. (2017). A framework for the retrieval of all-weather land surface temperature at a high spatial resolution from polar-orbiting thermal infrared and passive microwave data. *Remote Sensing of Environment, 195*, 107-117.

Duan, S.-B., Li, Z.-L., Tang, B.-H., Wu, H., Tang, R., & Bi, Y. (2015). Atmospheric correction of high-spatial-resolution satellite images with adjacency effects: Application to EO-1 ALI data. *International Journal of Remote Sensing, 36*, 5061-5074.

Eck, T.F., Holben, B.N., Reid, J.S., Dubovik, O., Smirnov, A., O'Neill, N.T., Slutsker, I., & Kinne, S. (1999). Wavelength dependence of the optical depth of biomass burning, urban, and desert dust aerosols. *Journal of Geophysical Research-Atmospheres, 104*, 31333-31349.

Fontanilles, G., Briottet, X., Fabre, S., Lefebvre, S., & Vandenhaute, P.F. (2010). Aggregation process of optical properties and temperature over heterogeneous surfaces in infrared domain. *Applied Optics, 49*, 4655-4669.

Fontanilles, G., Briottet, X., Fabre, S., & Trémas, T. (2008). Thermal infrared radiance simulation with aggregation modeling (TITAN): An infrared radiative transfer model for heterogeneous three-dimensional surface-application over urban areas. *Applied Optics, 47*, 5799-5810.

Freitas, S.C., Trigo, I.F., Macedo, J., Barroso, C., Silva, R., & Perdigão, R. (2013). Land surface temperature from multiple geostationary satellites. *International Journal of Remote Sensing, 34*, 3051-3068.

Galve, J.M., Coll, C., Caselles, V., & Valor, E. (2008). An atmospheric radiosounding database for generating land surface temperature algorithms. *IEEE Transactions on Geoscience and Remote Sensing, 46*, 1547-1557.

Gao, C., Jiang, X., Wu, H., Tang, B., Li, Z., & Li, Z.-L. (2012). Comparison of land surface temperatures from msg-2/seviri and terra/MODIS. *Journal of Applied Remote Sensing, 6*, 1-16.

Gastellu-Etchegorry, J.-P., Martin, E., & Gascon, F. (2004). DART: A 3D model for simulating satellite images and studying surface radiation budget. *International Journal of Remote Sensing, 25*, 73-96.

Gastellu-Etchegorry, J.-P., Yin, T., Lauret, N., Cajgfinger, T., Gregoire, T., Grau, E., Feret, J.-B., Lopes, M., Guilleux, J., Dedieu, G., Malenovský, Z., Cook, B., Morton, D., Rubio, J., Durrieu, S., Cazanave, G., Martin, E., & Ristorcelli, T. (2015). Discrete anisotropic radiative transfer (DART 5) for modeling airborne and satellite spectroradiometer and lidar acquisitions of natural and urban landscapes. *Remote Sensing, 7*, 1667-1701.

Gillespie, A., Rokugawa, S., Hook, S., Matsunaga, T., & Kahle, A.B. (1999). Temperature/emissivity

separation algorithm theoretical basis document, version 2.4. In (pp. 1-64). Maryland, USA: NASA/GSFC.

Gillespie, A., Rokugawa, S., Matsunaga, T., Cothern, J.S., Hook, S., & Kahle, A.B. (1998). A temperature and emissivity separation algorithm for advanced spaceborne thermal emission and reflection radiometer (ASTER) images. *IEEE Transactions on Geoscience and Remote Sensing, 36*, 1113-1126.

Gong, P., Liang, S., Carlton, E.J., Jiang, Q., Wu, J., Wang, L., & Remais, J.V. (2012). Urbanisation and health in china. *The Lancet, 379*, 843-852.

Gu, C., Wu, L., & Cook, I. (2012). Progress in research on chinese urbanization. *Frontiers of Architectural Research, 1*, 101-149.

Guillevic, P., & Gastellu-Etchegorry, J.-P. (2003). Thermal infrared radiative transfer within three-dimensional vegetation covers. *Journal of Geophysical Research-Atmospheres, 108*, 1-13.

Guo, H., Fu, W., & Liu, G. (2019). *Scientific satellite and moon-based earth observation for global change*. (First ed.). Springer Nature Singapore Pte Ltd.

Gustafson, W.T., Gillespie, A.R., & Yamada, G.J. (2006). Revisions to the ASTER temperature/emissivity separation algorithm. *2nd international symposium on Recent Advances in Quantitative Remote Sensing*, Torrent (Valencia), Spain (pp. 1-7)

Harris (2009). Atmospheric correction module: Quac and flaash user's guide, version 4.7. In (pp. 1-44). Burlington, USA: Harris Geospatial Solutions/Spectral Sciences Inc.

Howell, J.R., Siegel, R., & Menguc, M.P. (2010). Factors from finite areas to finite areas. *A catalog of radiation heat transfer configuration factors* (pp. 168-171). Austin, TEXAS, USA: Taylor and Francis/CRC.

Hu, T., Liu, Q., Du, Y., Li, H., Wang, H., & Cao, B. (2015). Analysis of the land surface temperature scaling problem: A case study of airborne and satellite data over the heihe basin. *Remote Sensing, 7*, 6489-6509.

Hulley, G.C., Ghent, D., Göttsche, F.M., Guillevic, P.C., Mildrexler, D.J., & Coll, C. (2019). Land surface temperature. *Taking the temperature of the earth* (pp. 57-127): Elsevier.

Isaacs, R.G., Wang, W.C., Worsham, R.D., & Goldenberg, S. (1987). Multiple scattering LOWTRAN and FASCODE models. *Applied Optics, 26*, 1272-1281.

Jackson, R., Pinterjr, P., & Reginato, R. (1985). Net radiation calculated from remote multispectral and ground station meteorological data. *Agricultural and Forest Meteorology, 35*, 153-164.

Jackson, R.D., Reginato, R.J., & Idso, S.B. (1977). Wheat canopy temperature: A practical tool for evaluating water requirements. *Water Resources Research, 13*, 651-656.

Jarosz, W. (2008). Efficient Monte Carlo methods for light transport in scattering media. In. California, United States: Department of Computer Science and Engineering, UC San Diego.

References

Jiang, L., Zhan, W., Voogt, J., Zhao, L., Gao, L., Huang, F., Cai, Z., & Ju, W. (2018). Remote estimation of complete urban surface temperature using only directional radiometric temperatures. *Building and Environment, 135*, 224-236.

Jimenez-Munoz, J.C., & Sobrino, J.A. (2003). A generalized single-channel method for retrieving land surface temperature from remote sensing data. *Journal of Geophysical Research-Atmospheres, 108*, 1-9.

Jimenez-Munoz, J.C., Sobrino, J.A., Mattar, C., Hulley, G., & Gottsche, F.-M. (2014). Temperature and emissivity separation from msg/seviri data. *IEEE Transactions on Geoscience and Remote Sensing, 52*, 5937-5951.

Johnson, G.T., Oke, T.R., Lyons, T.J., Steyn, D.G., Watson, I.D., & Voogt, J.A. (1991). Simulation of surface urban heat islands under 'ideal' conditions at night part 1: Theory and tests against field data. *Boundary-Layer Meteorology, 56*, 275-294.

Karnieli, A., Agam, N., Pinker, R.T., Anderson, M., Imhoff, M.L., Gutman, G.G., Panov, N., & Goldberg, A. (2010). Use of NDVI and land surface temperature for drought assessment: Merits and limitations. *Journal of Climate, 23*, 618-633.

Kaskaoutis, D.G., & Kambezidis, H.D. (2006). Investigation into the wavelength dependence of the aerosol optical depth in the Athens area. *Quarterly Journal of the Royal Meteorological Society, 132*, 2217-2234.

Kaufman, Y.J. (1982). Solution of the equation of radiative-transfer for remote-sensing over nonuniform surface reflectivity. *Journal of Geophysical Research-Oceans, 87*, 4137-4147.

Kaufman, Y.J. (1984). Atmospheric effect on spatial resolution of surface imagery: Errata. *Applied Optics, 23*, 4164-4172.

Kaufman, Y.J., Gitelson, A., Karnieli, A., Ganor, E., Fraser, R.S., Nakajima, T., Mattoo, S., & Holben, B.N. (1994). Size distribution and scattering phase function of aerosol-particles retrieved from sky brightness measurements. *Journal of Geophysical Research-Atmospheres, 99*, 10341-10356.

King, M.D. (1999). *EOS science plan: The state of science in the EOS program*. National Aeronautics and Space Administration.

Kneisys, F.X., Robertson, D.C., Abreu, L.W., Acharya, P., Anderson, G.P., Rothman, L.S., Chetwynd, J.H., Selby, J.E.A., Shettle, E.P., Gallery, W.O., Berk, A., Clough, S.A., & Bernsterin, L.S. (1996). The MODTRAN 2/3 report and LOWTRAN 7 model. In Hanscom AFB, MA, USA: G.D. Phillips Laboratory.

Kneizys, F.X., Shettle, E., Gallery, W., Chetwynd Jr, J., & Abreu, L. (1983). Atmospheric transmittance/radiance: Computer code LOWTRAN 6. In Hanscom AFB, MA, USA: Air Force Geophysics Laboratory.

Krayenhoff, E.S., & Voogt, J.A. (2007). A microscale three-dimensional urban energy balance model for studying surface temperatures. *Boundary-Layer Meteorology, 123*, 433-461.

References

Kustas, W., & Anderson, M. (2009). Advances in thermal infrared remote sensing for land surface modeling. *Agricultural and Forest Meteorology, 149*, 2071-2081.

Lau, K.K.-L., Ren, C., Ho, J., & Ng, E. (2016). Numerical modelling of mean radiant temperature in high-density sub-tropical urban environment. *Energy and Buildings, 114*, 80-86.

Li, Z.-L., & Becker, F. (1993). Feasibility of land surface-temperature and emissivity determination from AVHRR data. *Remote Sensing of Environment, 43*, 67-85.

Li, Z.-L., Tang, B.-H., Wu, H., Ren, H., Yan, G., Wan, Z., Trigo, I.F., & Sobrino, J.A. (2013a). Satellite-derived land surface temperature: Current status and perspectives. *Remote Sensing of Environment, 131*, 14-37.

Li, Z.-L., Tang, R., Wan, Z., Bi, Y., Zhou, C., Tang, B., Yan, G., & Zhang, X. (2009). A review of current methodologies for regional evapotranspiration estimation from remotely sensed data. *Sensors (Basel), 9*, 3801-3853.

Li, Z.-L., Wu, H., Wang, N., Qiu, S., Sobrino, J.A., Wan, Z., Tang, B.-H., & Yan, G. (2013b). Land surface emissivity retrieval from satellite data. *International Journal of Remote Sensing, 34*, 3084-3127.

Liou, K.-N. (2002). Light scattering by atmospheric particulates. *An introduction to atmospheric radiation* (pp. 169-257). San Diego, CA, USA: Academic press.

Liu, Z.-L., Wu, H., Tang, B.-H., Qiu, S., & Li, Z.-L. (2013). Atmospheric corrections of passive microwave data for estimating land surface temperature. *Optics Express, 21*, 15654-15663.

Malakar, N.K., Hulley, G.C., Hook, S.J., Laraby, K., Cook, M., & Schott, J.R. (2018). An operational land surface temperature product for Landsat thermal data: Methodology and validation. *IEEE Transactions on Geoscience and Remote Sensing, 56*, 5717-5735.

Martins, J.P.A., Trigo, I.F., Ghilain, N., Jimenez, C., Göttsche, F.-M., Ermida, S.L., Olesen, F.-S., Gellens-Meulenberghs, F., & Arboleda, A. (2019). An all-weather land surface temperature product based on msg/seviri observations. *Remote Sensing, 11*, 3044.

Masson, V. (2000). A physically-based scheme for the urban energy budget in atmospheric models. *Boundary-Layer Meteorology, 94*, 357-397.

McFarland, M.J., Miller, R.L., & Neale, C.M.U. (1990). Land surface temperature derived from the ssm/i passive microwave brightness temperatures. *IEEE Transactions on Geoscience and Remote Sensing, 28*, 839-845.

McMillin, L.M. (1975). Estimation of sea surface temperatures from two infrared window measurements with different absorption. *Journal of Geophysical Research, 80*, 5113-5117.

Merchant, C.J., Matthiesen, S., Rayner, N.A., Remedios, J.J., Jones, P.D., Olesen, F., Trewin, B., Thorne, P.W., Auchmann, R., Corlett, G.K., Guillevic, P.C., & Hulley, G.C. (2013). The surface temperatures of earth: Steps towards integrated understanding of variability and change. *Geoscientific Instrumentation, Methods and Data Systems, 2*, 305-321.

References

[dataset] Moustafa, C. (2015), Airs/aqua l1c infrared (ir) resampled and corrected radiances v006. Greenbelt, MD, USA, Goddard Earth Sciences Data and Information Services Center (GES DISC), Accessed: [Oct. 2018], https://doi.org/10.5067/Aqua/AIRS/DATA101.

Njoku, E.G., & Entekhabi, D. (1996). Passive microwave remote sensing of soil moisture. *Journal of Hydrology, 184*, 101-129.

Oke, T. (1987). *Boundary layer climates*. (2nd ed.). Psychology Press.

Oltra-Carrió, R., Sobrino, J.A., Franch, B., & Nerry, F. (2012). Land surface emissivity retrieval from airborne sensor over urban areas. *Remote Sensing of Environment, 123*, 298-305.

Oltra-Carrio, R., Cubero-Castan, M., Briottet, X., & Sobrino, J.A. (2014). Analysis of the performance of the tes algorithm over urban areas. *IEEE Transactions on Geoscience and Remote Sensing, 52*, 6989-6998.

Oltra-Carrio, R., Sobrino, J.A., Cubero-Castan, M., & Briottet, X. (2013). Performance of tes method over urban areas at a high spatial resolution scale. *2013 5th Workshop on Hyperspectral Image and Signal Processing: Evolution in Remote Sensing (Whispers)*, 1-4.

Otterman, J., & Fraser, R.S. (1979). Adjacency effects on imaging by surface reflection and atmospheric scattering: Cross radiance to zenith. *Applied Optics, 18*, 2852-2860.

Ottle, C., & Vidal-Madjar, D. (1992). Estimation of land surface-temperature with NOAA9 data. *Remote Sensing of Environment, 40*, 27-41.

Ouaidrari, H., & Vermote, E.F. (1999). Operational atmospheric correction of Landsat TM data. *Remote Sensing of Environment, 70*, 4-15.

Pallotta, S., Briottet, X., Miesch, C., & Kerr, Y. (2006). Sensor radiance physical model for rugged heterogeneous surfaces in the 3-14 mum region. *Optics Express, 14*, 2130-2150.

Payan, V., & Royer, A. (2004). Analysis of temperature emissivity separation (tes) algorithm applicability and sensitivity. *International Journal of Remote Sensing, 25*, 15-37.

Pearce, W.A. (1986). Monte Carlo study of the atmospheric spread function. *Applied Optics, 25*, 438-447.

Prata, A.J. (1993). Land surface temperatures derived from the advanced very high resolution radiometer and the along-track scanning radiometer: 1. Theory. *Journal of Geophysical Research, 98*, 16689-16702.

Prata, A.J., Caselles, V., Coll, C., Sobrino, J.A., & Ottlé, C. (1995). Thermal remote sensing of land surface temperature from satellites: Current status and future prospects. *Remote Sensing Reviews, 12*, 175-224.

Qian, Y.-G., Li, Z.-L., & Nerry, F. (2013). Evaluation of land surface temperature and emissivities retrieved from msg/seviri data with MODIS land surface temperature and emissivity products. *International Journal of Remote Sensing, 34*, 3140-3152.

Qin, Z., Dall'Olmo, G., Karnieli, A., & Berliner, P. (2001a). Derivation of split window algorithm and

its sensitivity analysis for retrieving land surface temperature from NOAA-advanced very high resolution radiometer data. *Journal of Geophysical Research-Atmospheres, 106*, 22655-22670.

Qin, Z., Karnieli, A., & Berliner, P. (2001b). A mono-window algorithm for retrieving land surface temperature from Landsat TM data and its application to the Israel-Egypt border region. *International Journal of Remote Sensing, 22*, 3719-3746.

Qiu, J., Zong, X., & Zhang, X. (2005). A study of the scaling height of the tropospheric aerosol and its extinction coefficient profile. *Journal of Aerosol Science, 36*, 361-371.

Qu, Y. (2011). Three-dimensional modeling of radiative and convective exchanges in the urban atmosphere. In. Paris, France: École des Ponts ParisTech, University of Paris-Est.

Reck, R.A. (1976). Thermal and radiative effects of atmospheric aerosols in the northern hemisphere calculated using a radiative-convective model. *Atmospheric Environment, 10*, 611-617.

Reinersman, P.N., & Carder, K.L. (1995). Monte Carlo simulation of the atmospheric point-spread function with an application to correction for the adjacency effect. *Applied Optics, 34*, 4453-4471.

Ren, H., Dong, J., Liu, R., Zheng, Y., Guo, J., Chen, S., Nie, J., & Zhao, Y. (2020). New hybrid algorithm for land surface temperature retrieval from multiple-band thermal infrared image without atmospheric and emissivity data inputs. *International Journal of Digital Earth*, 1-24.

Ren, H., Ye, X., Liu, R., Dong, J., & Qin, Q. (2018). Improving land surface temperature and emissivity retrieval from the chinese gaofen-5 satellite using a hybrid algorithm. *IEEE Transactions on Geoscience and Remote Sensing, 56*, 1080-1090.

Richter, R. (1990). A fast atmospheric correction algorithm applied to Landsat TM images. *International Journal of Remote Sensing, 11*, 159-166.

Richter, R. (1998). Correction of satellite imagery over mountainous terrain. *Applied Optics, 37*, 4004-4015.

Richter, R., Bachmann, M., Dorigo, W., & Muller, A. (2006). Influence of the adjacency effect on ground reflectance measurements. *IEEE Geoscience and Remote Sensing Letters, 3*, 565-569.

Running, S.W., Justice, C.O., Salomonson, V., Hall, D., Barker, J., Kaufmann, Y.J., Strahler, A.H., Huete, A.R., Muller, J.P., Vanderbilt, V., Wan, Z., Teillet, P., & Carneggie, D. (1994). Terrestrial remote sensing science and algorithms planned for EOS/MODIS. *International Journal of Remote Sensing, 15*, 3587-3620.

Sanders, L.C., Schott, J.R., & Raqueno, R. (2001). A VNIR/SWIR atmospheric correction algorithm for hyperspectral imagery with adjacency effect. *Remote Sensing of Environment, 78*, 252-263.

Sattari, F., & Hashim, M. (2014). A breife review of land surface temperature retrieval methods from thermal satellite sensors. *Middle East Journal of Scientific Research, 22*, 757-768.

Schmugge, T., Hook, S.J., & Coll, C. (1998). Recovering surface temperature and emissivity from thermal infrared multispectral data. *Remote Sensing of Environment, 65*, 121-131.

References

Sellers, P., Hall, F., Asrar, G., Strebel, D., & Murphy, R. (1988). The first islscp field experiment (fife). *Bulletin of the American Meteorological Society, 69*, 22-27.

Semenov, A.A., Moshkov, A.V., Pozhidayev, V.N., Barducci, A., Marcoionni, P., & Pippi, I. (2011). Estimation of normalized atmospheric point spread function and restoration of remotely sensed images. *IEEE Transactions on Geoscience and Remote Sensing, 49*, 2623-2634.

Simmer, C. (1999). Contribution of microwave remote sensing from satellites to studies on the earth energy budget and the hydrological cycle. *Advances in Space Research, 24*, 897-905.

Sobrino, J.A., Caselles, V., & Coll, C. (1993). Theoretical split-window algorithms for determining the actual surface temperature. *Il Nuovo Cimento C, 16*, 219-236.

Sobrino, J.A., Coll, C., & Caselles, V. (1991). Atmospheric correction for land surface temperature using NOAA-11 AVHRR channels 4 and 5. *Remote Sensing of Environment, 38*, 19-34.

Sobrino, J.A., Del Frate, F., Drusch, M., Jimenez-Munoz, J.C., Manunta, P., & Regan, A. (2016). Review of thermal infrared applications and requirements for future high-resolution sensors. *IEEE Transactions on Geoscience and Remote Sensing, 54*, 2963-2972.

Sobrino, J.A., & Jiménez-Muñoz, J.C. (2014). Minimum configuration of thermal infrared bands for land surface temperature and emissivity estimation in the context of potential future missions. *Remote Sensing of Environment, 148*, 158-167.

Sobrino, J.A., Li, Z.-L., Stoll, M.P., & Becker, F. (1994). Improvements in the split-window technique for land surface temperature determination. *IEEE Transactions on Geoscience and Remote Sensing, 32*, 243-253.

Sobrino, J.A., Li, Z.-L., Stoll, M.P., & Becker, F. (1996). Multi-channel and multi-angle algorithms for estimating sea and land surface temperature with ATSR data. *International Journal of Remote Sensing, 17*, 2089-2114.

[dataset] Spacesystems, A.M.A.J., & Team, U.S.J.A.S. (2001a), ASTER level 2 surface temperature product. U.S.A, Accessed: [Feb. 5, 2019], 10.5067/ASTER/AST_08.003.

[dataset] Spacesystems, N.M.A.J., & Team, U.S.J.A.S. (2001b), ASTER level 2 emissivity product. U.S.A, Accessed: [Feb. 5, 2019], 10.5067/ASTER/AST_05.003.

Tanre, D., Deschamps, P.Y., Duhaut, P., & Herman, M. (1987). Adjacency effect produced by the atmospheric scattering in thematic mapper data. *Journal of Geophysical Research-Atmospheres, 92*, 12000-12006.

Tanre, D., Herman, M., & Deschamps, P. (1981). Influence of the background contribution upon space measurements of ground reflectance. *Applied Optics, 20*, 3676-3684.

Thome, K., Palluconi, F., Takashima, T., & Masuda, K. (1998). Atmospheric correction of ASTER. *IEEE Transactions on Geoscience and Remote Sensing, 36*, 1199-1211.

Tomlinson, C.J., Chapman, L., Thornes, J.E., & Baker, C. (2011). Remote sensing land surface

temperature for meteorology and climatology: A review. *Meteorological Applications, 18*, 296-306.

Vermote, E.F., Tanré, D., Deuze, J.L., Herman, M., & Morcette, J.-J. (1997). Second simulation of the satellite signal in the solar spectrum, 6S: An overview. *IEEE Transactions on Geoscience and Remote Sensing, 35*, 675-686.

Vining, R.C., & Blad, B.L. (1992). Estimation of sensible heat flux from remotely sensed canopy temperatures. *Journal of Geophysical Research, 97*, 18951-18954.

Voogt, J.A. (1995). Thermal remote sensing of urban surface temperatures. In. Vancouver, British Columbia, Canada: Department of Geography, University of British Columbia.

Voogt, J.A., & Oke, T.R. (1997). Complete urban surface temperatures. *Journal of Applied Meteorology, 36*, 1117-1132.

Wan, Z. (2008). New refinements and validation of the MODIS land-surface temperature/emissivity products. *Remote Sensing of Environment, 112*, 59-74.

Wan, Z. (2014). New refinements and validation of the collection-6 MODIS land-surface temperature/emissivity product. *Remote Sensing of Environment, 140*, 36-45.

Wan, Z., & Dozier, J. (1996). A generalized split-window algorithm for retrieving land-surface temperature from space. *IEEE Transactions on Geoscience and Remote Sensing, 34*, 892-905.

[dataset] Wan, Z., Hook, S., & Hulley, G. (2015a), Mod11_l2 MODIS/terra land surface temperature/emissivity 5-min l2 swath 1km v006. U.S.A, Accessed: [Feb. 5, 2019], 10.5067/MODIS/MOD11_L2.006.

[dataset] Wan, Z., Hook, S., & Hulley, G. (2015b), Myd11_l2 MODIS/aqua land surface temperature/emissivity 5-min l2 swath 1km v006. NASA EOSDIS LP DAAC, Accessed: [Oct. 2018], https://doi.org/10.5067/MODIS/MYD11_L2.006.

Wan, Z., & Li, Z.-L. (1997). A physics-based algorithm for retrieving land-surface emissivity and temperature from EOS/MODIS data. *IEEE Transactions on Geoscience and Remote Sensing, 35*, 980-996.

Wan, Z., & Li, Z.-L. (2008). Radiance-based validation of the v5 MODIS land-surface temperature product. *International Journal of Remote Sensing, 29*, 5373-5395.

Wang, D., Chen, Y., & Zhan, W. (2018). A geometric model to simulate thermal anisotropy over a sparse urban surface (guta-sparse). *Remote Sensing of Environment, 209*, 263-274.

Wang, W.-C., & Ryan, P.B. (1983). Overlapping effect of atmospheric H_2O, CO_2 and O_3 on the CO_2 radiative effect. *Tellus B: Chemical and Physical Meteorology, 35*, 81-91.

Watson, K. (1992). Two-temperature method for measuring emissivity. *Remote Sensing of Environment, 42*, 117-121.

Wen, J., Su, Z.B., & Ma, Y.M. (2003). Determination of land surface temperature and soil moisture from tropical rainfall measuring mission/microwave imager remote sensing data. *Journal of Geophysical*

References

Research-Atmospheres, 108, 1-10.

Wiscombe, W.J., & Grams, G.W. (1976). The backscattered fraction in two-stream approximations. *Journal of the Atmospheric Sciences, 33*, 2440-2451.

Yang, G., Liu, Q., Liu, Q., Huang, W., & Wang, J. (2009). Simulation of high-resolution mid-infrared (3–5 μm) images using an atmosphere radiative transfer analytic model. *International Journal of Remote Sensing, 30*, 6003-6022.

Yang, J., Wong, M.S., Ho, H.C., Krayenhoff, E.S., Chan, P.W., Abbas, S., & Menenti, M. (2020). A semi-empirical method for estimating complete surface temperature from radiometric surface temperature, a study in hong kong city. *Remote Sensing of Environment, 237*, 111540.

Yu, Y., Privette, J.L., & Pinheiro, A.C. (2005). Analysis of the npoess viirs land surface temperature algorithm using MODIS data. *IEEE Transactions on Geoscience and Remote Sensing, 43*, 2340-2350.

Zhang, R., Tian, J., Su, H., Sun, X., Chen, S., & Xia, J. (2008). Two improvements of an operational two-layer model for terrestrial surface heat flux retrieval. *Sensors, 8*, 6165-6187.

Zhang, X., Zhou, J., Gottsche, F.-M., Zhan, W., Liu, S., & Cao, R. (2019). A method based on temporal component decomposition for estimating 1-km all-weather land surface temperature by merging satellite thermal infrared and passive microwave observations. *IEEE Transactions on Geoscience and Remote Sensing, 57*, 4670-4691.

Zheng, X., Gao, M., Li, Z.-L., Chen, K.-S., Zhang, X., & Shang, G. (2020). Impact of 3-d structures and their radiation on thermal infrared measurements in urban areas. *IEEE Transactions on Geoscience and Remote Sensing, Early Access*, 1-15.

Zheng, X., Li, Z.-L., Nerry, F., & Zhang, X. (2019a). A new thermal infrared channel configuration for accurate land surface temperature retrieval from satellite data. *Remote Sensing of Environment, 231*, 1-12.

Zheng, X., Li, Z.-L., Zhang, X., & Shang, G. (2019b). Quantification of the adjacency effect on measurements in the thermal infrared region. *IEEE Transactions on Geoscience and Remote Sensing, 57*, 9674-9687.

References

Résumé des travaux en français

Détermination de la température de surface urbaine à partir des données à haute résolution spatiale

Doctorant : Xiaopo ZHENG

Directeur de Thèse : Zhao-Liang LI

Laboratoire : Laboratoire des sciences de l'ingénieur, de l'informatique et de l'imagerie (ICube), UMR 7357, CNRS-Université de Strasbourg, 300 bd Sébastien Brant, CS 10413, F-67412 Illkirch Cedex, France

Détermination de la température de surface urbaine à partir des données à haute résolution spatiale

1. Introduction

1.1. Contexte

La température de la surface terrestre (LST) est l'une des plus importantes données du système terrestre, qui pourrait influencer les écosystèmes à l'échelle régionale et mondiale. Tous les processus de surface de la Terre liés au bilan énergétique et hydrologique pourraient être paramétrés directement ou indirectement par la LST (Hulley et al., 2019). Ainsi, il est requis dans une variété de recherches, y compris la surveillance de l'environnement urbain (Anderson et al., 2008). Comme nous le savons tous, les villes agissent toujours comme le centre d'une certaine région dans de nombreux domaines tels que la population, l'administration, les transports, l'économie, l'éducation, la culture, etc., qui sont cruciaux pour les civilisations humaines. Selon le Population Reference Bureau en 2019, plus de la moitié de la population mondiale vit dans les zones urbaines et le nombre continue d'augmenter (Bureau, 2019). Par conséquent, il est très important d'étudier l'environnement urbain en détail, ce qui nécessite la LST urbain précise comme l'un des paramètres d'entrée les plus essentiels.

Par rapport aux mesures au sol, la télédétection infrarouge thermique offre un moyen plus efficace d'obtenir les LST régionaux et mondiaux de la Terre. Après des décennies de développement, une grande variété d'algorithmes de détermination du LST ont été développés pour différents types de capteurs TIR et ont connu un grand succès (Li et al., 2013). On peut conclure que, pour la plupart des circonstances concernant les surfaces planes naturelles et les images TIR à résolution spatiale moyenne/basse, la LST pourrait être récupéré avec une précision de 1,0 K en utilisant les algorithmes de détermination du LST existants. Cependant, ces algorithmes ont encore leurs limites, notamment en ce qui concerne la détermination précise du LST urbain à partir de mesures TIR par satellite à haute résolution spatiale.

En 1ᵉʳ lieu la non prise en compte de l'effet d'adjacence dans la région spectrale TIR.

Selon des études précédentes, la force de l'effet d'adjacence diminue généralement avec l'augmentation de la longueur d'onde et la diminution de la résolution spatiale de l'image.

Ainsi, l'effet d'adjacence a toujours été négligé avec les images TIR couramment utilisées car elles ont des longueurs d'onde d'observation relativement longues et des résolutions spatiales basses. Cependant, avec le développement continu de la technologie de la télédétection, les images TIR à haute résolution spatiale sont réalisables de nos jours et l'effet d'adjacence pourrait augmenter de manière significative (Zheng et al., 2019b). Par conséquent, la précision de la détermination LST peut diminuer si l'effet d'adjacence reste ignoré.

Deuxièmement, l'impact des structures tridimensionnelles (3-D) et de leur rayonnement sur les mesures TIR.

Les structures tridimensionnelles dans les zones urbaines rendent évidemment les processus de transfert radiatif TIR plus complexes par rapport aux surfaces planes (Zheng et al., 2020): Premièrement, les réflexions multiples à l'intérieur des structures tridimensionnelles pourraient introduire des radiations supplémentaires dans les mesures TIR par satellite. Deuxièmement, la différence de température entre les zones ensoleillées et ombragées aggrave l'hétérogénéité thermique des zones urbaines pendant la journée. Troisièmement, les compositions à l'intérieur de l'IFOV du capteur changent avec l'angle de vue, conduisant à des signaux anisotropes observés par satellite Tous ces éléments pourraient avoir un impact non négligeable sur la radiance observée par satellite mais n'ont pas encore été pris en compte dans les algorithmes existants de détermination de la LST.

Troisièmement, la dépendance des algorithmes de détermination de LST existants de la connaissance préalable précise de l'atmosphère et/ou de la surface de la Terre.

Les algorithmes de détermination du LST existants nécessitent des connaissances préalables précisse (paramètres atmosphériques et/ou émissivité de la surface de la Terre) pour récupérer la LST à partir des mesures TIR par satellite (Zheng et al., 2019a). Cependant, une telle connaissance préalable n'est pas toujours disponible dans des applications réelles à l'échelle des pixels. Par conséquent, la précision de détermination du LST peut ne pas être en mesure de répondre à l'exigence de mieux que 1,0 K, comme l'exigent de nombreuses autres disciplines dans certaines circonstances.

1.2. Objectifs de la thèse

Cette thèse est consacrée à l'étude des facteurs influençant les mesures TIR par satellite et la précision de la détermination LST, dont le but est d'améliorer la précision de la détermination LST dans les zones urbaines à partir de mesures TIR par satellite à haute

résolution spatiale.

Plus précisément, quatre objectifs de recherche ont été impliqués dans cette thèse comme suit:

(1) Etudier quantitativement l'effet d'adjacence dans la région spectrale TIR dans différentes conditions atmosphériques et d'imagerie.

(2) Etudier quantitativement l'impact des structures 3-D et de leur rayonnement sur les mesures TIR.

(3) Explorer de nouvelles méthodes qui pourraient être utilisées pour obtenirr directement la LST précise à partir de mesures TIR par satellite sans dépendre de connaissances préalables.

(4) Explorer le développement d'une méthode améliorée de détermination de laLST pour les mesures TIR par satellite à haute résolution spatiale des zones urbaines sur la base des recherches impliquées dans les trois premiers objectifs.

2. Quantification de l'effet d'adjacence sur les mesures dans la région TIR

Pour étudier quantitativement l'effet d'adjacence pour diverses atmosphères et résolutions spatiales d'images, un modèle de transfert radiatif à effet d'adjacence (FAERTM) a été développé. À des fins de simplification, les trois hypothèses suivantes ont été adoptées. Tout d'abord, la surface du terrain est plane, sans terrain accidentés ni bâtiments. Deuxièmement, les observations sont acquises verticalement, ce qui est généralement vrai pour les images à haute résolution spatiale. Troisièmement, la proportion d'énergie qui a été diffusée plus de deux fois est insignifiante. Avec ces hypothèses, l'équation de transfert radiatif de FAERTM peut ainsi s'exprimer comme suit:

$$L = B(T_b) = \tau \varepsilon B(T_s) + \tau(1-\varepsilon)(L_\downarrow + \frac{L_2}{1-\rho S}) + L_\uparrow + L_1 \qquad \text{Eq. 1}$$

dans lequelle, B est la fonction de Planck. T_b est la température de rayonnement du canal équivalente compte tenu de l'effet d'adjacence, τ est la transmittance atmosphérique directe, ε and T_s sont LSE et LST, $L_\downarrow$ and $L_\uparrow$ sont respectivement les radiances ascendantes et ascendantes de l'atmosphère, ρ est la réflectance de la surface terrestre, et S est l'albédo sphérique atmosphérique au fond de l'atmosphère. L_1 est la radiance de

pixel adjacent dispersé en première incidende et L_2 est la radiance de pixel adjacent qui a été réfléchi par l'atmosphère, avec $(1 - \rho S)$ représentant l'illumination due au mécanisme de piégeage.

L'effet d'adjacence est alors défini comme la différence de température de rayonnement cible observée entre un cas avec un rayonnement de pixels adjacents et un cas sans rayonnement de pixels adjacents:

$$\Delta T_b = T_b - T_b^0$$ Eq. 2

dans lequel,

$$L = B\left(T_b^0\right) = \tau \varepsilon B\left(T_s\right) + \tau\left(1 - \varepsilon\right)L_\downarrow + L_\uparrow$$ Eq. 3

Différentes combinaisons d'entrées de simulation ont été sélectionnées pour fournir une variété de scénarios atmosphériques et d'imagerie pour étudier quantitativement l'effet d'adjacence (Table 1).

Table 1. Paramètres de simulation d'entrée de scénario

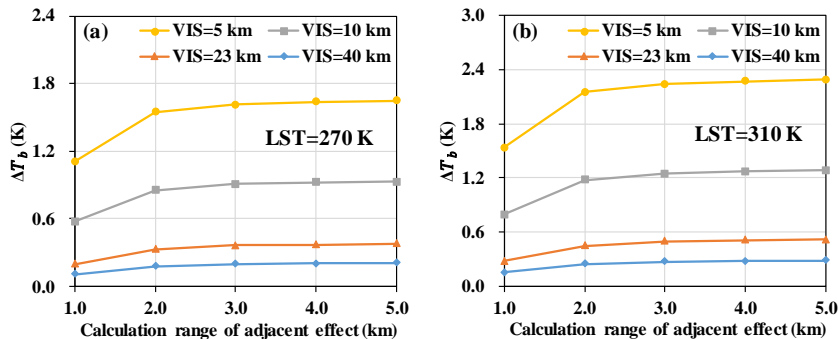| Conditions atmosphériques	
Modèle d'atmosphère	1976 U.S. Standard
Modèle aérosol	RURAL, URBAN
Visibilité atmosphérique	5, 10, 23, 40 km
Conditions d'imagerie	
Longueur d'onde	8, 9, 10, 11, 12 μm
Résolution spatiale de l'image	0.005, 0.01, 0.03, 0.06, 0.1, 0.25, 0.5, 1.0 km
Température du pixel cible (TAT_LST)	270, 290, 310 K
Température des pixels adjacents	De TAT_LST – 30 K à TAT_LST + 30 K avec un pas de 10 K
Emissivité du pixel cible	0.90, 0.98
Emissivité des pixels adjacents	0.90, 0.98
Rayon de calcul de l'effet d'adjacence	1.0, 2.0, 3.0, 4.0, 5.0 km
Altitude du capteur	705 km

Fig. 1. Effet d'adjacence en fonction du rayon de calcul pour différentes visibilités atmosphériques (VIS). La longueur d'onde, la résolution spatiale de l'image, le type d'aérosol et le LSE étaient 10 μm, 30 m, RURAL et 0,90, respectivement. La température cible et la température du sol étaient les mêmes. LST varie de (a) 270 K et (b) 310 K.
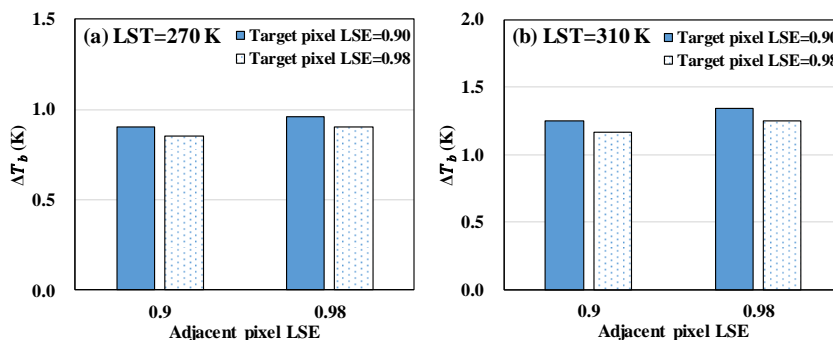
Fig. 2. Effet d'adjacence pour différentes combinaisons d'émissivité cible et pixels adjacents. La longueur d'onde, la résolution spatiale de l'image, le type d'aérosol et la visibilité atmosphérique étaient respectivement de 10 μm, 30 m, RURAL et 10 km. La température cible et la température du sol étaient les mêmes, avec des LST de (a) 270 K ou (b) 310 K.
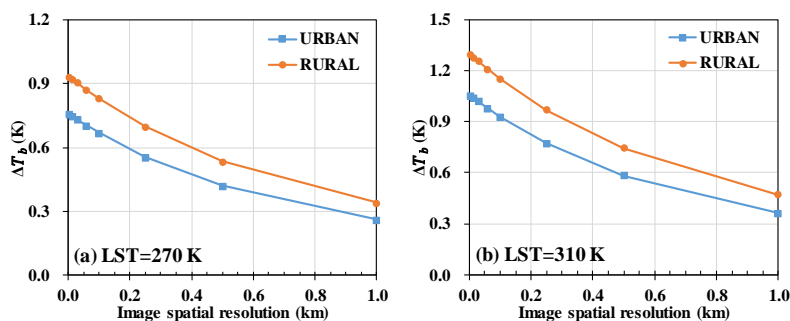

Fig. 3. Effet d'adjacence en fonction de la résolution spatiale de l'image pour deux types d'aérosols. La longueur d'onde, la visibilité atmosphérique et la LSE étaient respectivement de 10 μm, 10 km et 0,98. La température cible et la température de sol étaient les mêmes, avec des LST de (a) 270 K et (b) 310 K.

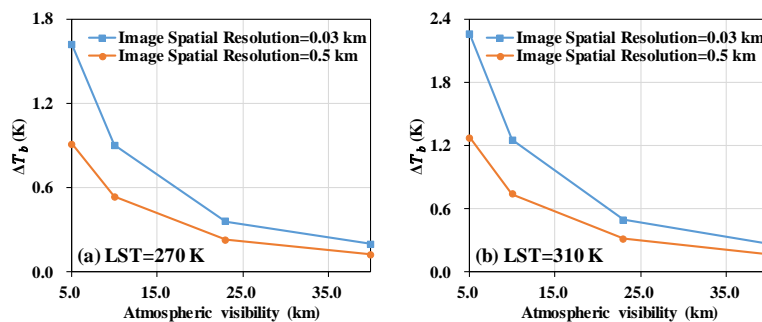Fig. 4. Effet d'adjacence en fonction de la visibilité atmosphérique. Le type d'aérosol, la longueur d'onde et le LSE étaient respectivement RURAL, 10,0 μm et 0,98. La température cible et la température de sol étaient les mêmes avec des LST de (a) 270 K et (b) 310 K.
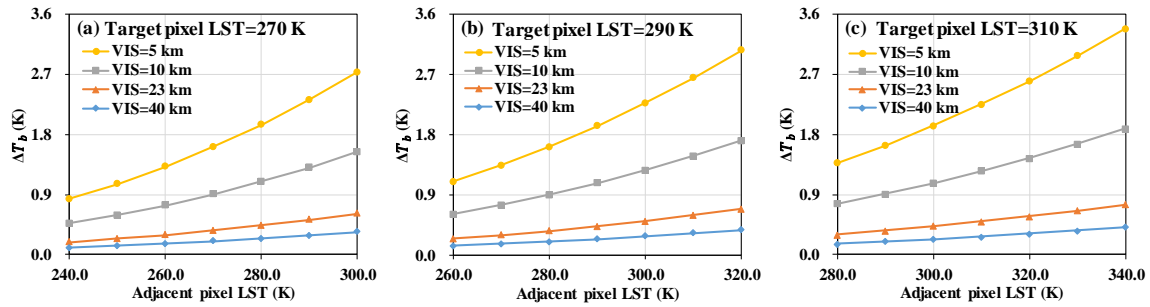
Fig. 5. Effet d'adjacence en fonction de la température des pixels adjacents. Le type d'aérosol, la longueur d'onde, la résolution spatiale de l'image et le LSE étaient respectivement RURAL, 10 µm, 30 m et 0,98.
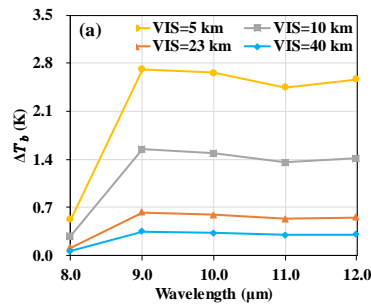

Fig. 6. L'effet d'adjacence en fonction de la longueur d'onde pour différentes visibilités atmosphériques (VIS). Le type d'aérosol, la résolution spatiale de l'image et le LSE étaient respectivement RURAL, 30 m et 0,98. Les températures des pixels cibles et adjacents étaient 290 K et 310 K, respectivement.

Les Fig. 1 à Fig. 6 présentent l' amplitude de l'effet d'adjacence en fonction de la rayon de calcul, du LSE, de la résolution spatiale de l'image, de type d'aérosol, de la visibilité atmosphérique, du LST et de la longueur d'onde, respectivement. Il est démontré que l'effet d'adjacence provient principalement de pixels à moins de 3 km de la cible et n'est pas sensible au type d'aérosol et au LSE. Contrairement aux scénarios avec des atmosphères claires, une résolution spatiale d'image basse et des pixels adjacents froids, l'amplitude de l'effet d'adjacence a augmenté avec la diminution de la visibilité atmosphérique, une amélioration de la résolution spatiale de l'image ou une augmentation du rayonnement des pixels adjacents. Dans des conditions extrêmes, la magnitude de l'effet d'adjacence peut même dépasser 3,0 K. Il est également montré que, à mesure que la longueur d'onde augmente, l'effet d'adjacence diminue généralement, sauf à 8 µm; à cette longueur d'onde, la transmittance atmosphérique et la profondeur optique de diffusion des aérosols sont toutes deux assez faibles, ce qui entraîne l'absorption de la plupart des radiations à effet d'adjacence et qui ne donc pas observé par le capteur.

3. Modélisation de l'impact des structures 3-D et de leur rayonnement sur les mesures TIR en zones urbaines

Le processus de transfert radiatif sera beaucoup plus complexe dans les zones urbaines avec des structures 3-D par rapport à celui des surfaces planes. Pour étudier l'impact des structures 3-D et leur rayonnement sur les mesures TIR, le modèle analytique de transfert radiatif infrarouge thermique sur les zones urbaines (ATIMOU) a été développé:

Tout d'abord, un canyon de rue dans une zone urbaine est défini comme deux bâtiments parallèles situés de chaque côté d'une rue et orientés dans une direction nord-sud (Fig. 7).
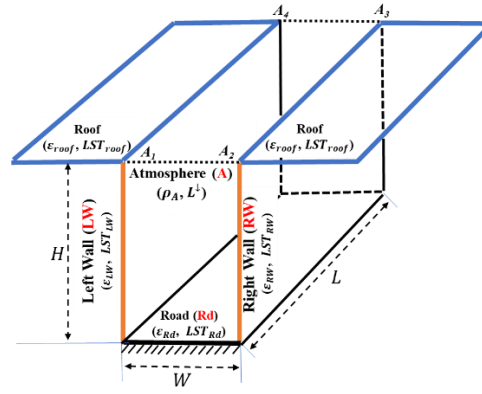

Fig. 7. Illustration d'un canyon de rue dans les zones urbaines.

Ensuite, la mesure TIR par satellite en tenant compte de l'impact des structures 3-D et de leur rayonnement a été modélisée comme:

$$L^{TOA\_3D} = B(T^{TOA\_3D}) = \tau(\theta)L^{Gnd\_3D} + L^{\uparrow}(\theta) \qquad \text{Eq. 4}$$

$$L^{Gnd\_3D} = B(T^{Gnd\_3D}) = \frac{\Omega_{roof}}{\Omega_{IFOV}} L^{Gnd}_{roof} + \frac{\Omega_{road}}{\Omega_{IFOV}} L^{Gnd\_3D}_{Rd} + \frac{\Omega_{wall}}{\Omega_{IFOV}} L^{Gnd\_3D}_{wall} \qquad \text{Eq. 5}$$

dans lequel, L^{TOA_3D} et T^{TOA_3D} représentent respectivement la radiance et la température de rayonnement du pixel cible sur un canyon de rue observée par satellite, en tenant compte de l'impact des structures 3-D et de leur rayonnement. $\tau(\theta)$ et $L^{\uparrow}(\theta)$ sont la transmittance atmosphérique totale et le radiance d'upwelling atmosphérique le long de la direction d'observation avec un angle zénithal de θ, respectivement. L^{Gnd_3D} et T^{Gnd_3D} représentent la radiance et la température de rayonnement du pixel cible sur un canyon de rue observée depuis le terrain, respectivement, en tenant compte de l'impact des structures 3-D et de leur rayonnement. Ω_{IFOV} est l'angle solide de l'IFOV entier du capteur; Ω_{roof}, Ω_{road}, et Ω_{wall} sont respectivement les angles solides des projections par rapport aux composants du toit, de la rue et du mur à l'intérieur de l'IFOV du capteur. L^{Gnd}_{roof} est la

radiance du toit observé depuis le terrain; et $L_{Rd}^{Gnd\_3D}$ et $L_{wall}^{Gnd\_3D}$ sont, respectivement, le radiance de la rue et du mur observé depuis le terrain avec l'impact des structures 3-D et leur rayonnement.

L'impact des structures 3-D et de leur rayonnement sur les mesures TIR sur un canyon de rue observée depuis le terrain (ΔT_{3D-2D}^{Gnd}) et par satellite (ΔT_{3D-2D}^{TOA}) a été défini par les équations suivantes comme:

$$\Delta T_{3D-2D}^{Gnd} = T^{Gnd\_3D} - T^{Gnd} \qquad \text{Eq. 6}$$

$$\Delta T_{3D-2D}^{TOA} = T^{TOA\_3D} - T^{TOA} \qquad \text{Eq. 7}$$

$$L^{TOA} = B(T^{TOA}) = \tau(\theta)L^{Gnd} + L^{\uparrow}(\theta) \qquad \text{Eq. 8}$$

$$L^{Gnd} = B(T^{Gnd}) = \frac{\Omega_{roof}}{\Omega_{IFOV}}L_{roof}^{Gnd} + \frac{\Omega_{road}}{\Omega_{IFOV}}L_{Rd}^{Gnd} + \frac{\Omega_{wall}}{\Omega_{IFOV}}L_{wall}^{Gnd} \qquad \text{Eq. 9}$$

dans lequelles, L^{TOA} et T^{TOA} représentent respectivement la radiance et la température de rayonnement du pixel cible sur un canyon de rue observée par satellite, sans tenir compte de l'impact des structures 3-D et de leur rayonnement. L^{Gnd} et T^{Gnd} représentent respectivement la radiance et la température de rayonnement du pixel cible sur un canyon de rue observée depuis le terrain, sans tenir compte de l'impact des structures 3-D et de leur rayonnement. L_{Rd}^{Gnd} et L_{wall}^{Gnd} sont, respectivement, le radiance de la rue et du mur observé depuis le terrain sans l'impact des structures 3-D et de leur rayonnement.

Différents scénarios simulés ont été réalisés pour étudier quantitativement l'amplitude de l'impact des structures 3-D et de leur rayonnement dans différentes conditions (Table 2).

Table 2. Entrées de simulation pour étudier l'impact des structures 3-D et leur rayonnement.

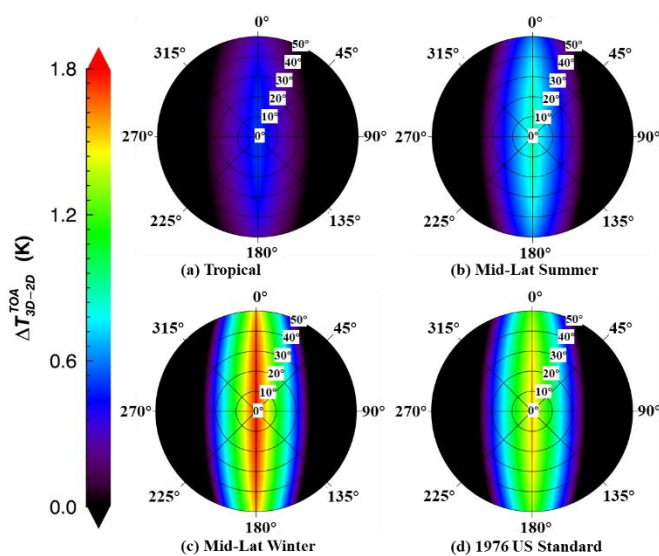| **Propriétés géométriques**		
H/W	0.5, 1.0, 2.0 (Défaut), 4.0	
Propriétés radiatives		
	Emissivité (Min, Mean, Max)	Température (K)
Mur	0.415, 0.906 (Défaut), 0.967	260, 280, 300 (Défaut). 320, 340
Rue	0.921, 0.950 (Défaut), 0.973	260, 280, 300 (Défaut). 320, 340
Toit	0.016, 0.813 (Défaut), 0.988	260, 280, 300 (Défaut). 320, 340
Paramètres atmosphériques		
Type atmosphérique (Teneur totale en vapeur d'eau / température de la couche inférieure)	Tropical (4.11 g/cm² / 300.15 K), Mid-Latitude Summer (2.92 g/cm² / 294.15 K), Mid-Latitude Winter (0.85 g/cm² / 272.15 K), 1976 US Standard (1.42 g/cm² / 288.15 K, Défaut)	
Angle d'observation		
Angle zénith	0° ~ 50° Angle	0° ~ 360°

Fig. 8. Amplitude de l'impact des structures 3-D et de leur rayonnement sur les mesures TIR sur un canyon de rue observé par satellite pour différents types atmosphériques. Les paramètres supplémentaires requis ont été définis comme valeurs par défaut répertoriées dans Table 2.
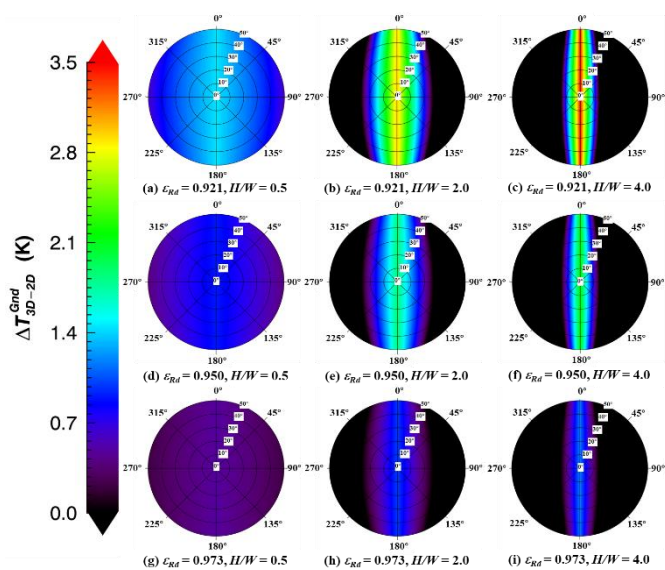

Fig. 9. Amplitude de l'impact des structures 3-D et de leur rayonnement sur les mesures TIR sur un canyon de rue observé depuis le terrain sous différentes combinaisons d'émissivité et H/W. Les paramètres supplémentaires ont été définis comme valeurs par défaut répertoriées dans Table 2.
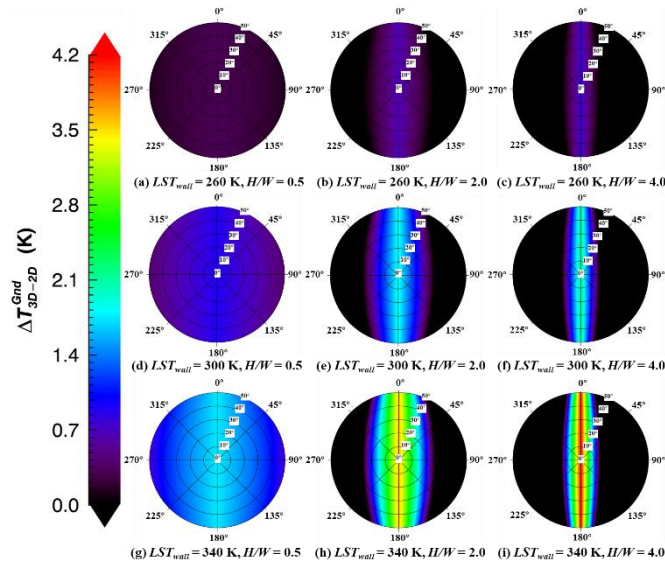
Fig. 10. Amplitude de l'impact des structures 3-D et de leur rayonnement sur les mesures TIR sur un canyon de rue observé depuis le terrain sous différentes combinaisons de température de mur et H/W. Les températures du mur gauche et droit ont été définies pour être les mêmes pour simplification. Les paramètres supplémentaires ont été définis comme valeurs par défaut répertoriées dans Table 2.

La Fig. 8 montre que, sur un canyon de rue, l' amplitude de l'impact des structures 3-D et de leur rayonnement sur les mesures TIR par satellite dans une atmosphère chaude et humide est plus petite que celle dans une atmosphère froide et sèche. Il est également montré que l'impact des structures 3-D et de leur rayonnement est toujours le plus important au nadir. De plus, l'augmentation de H/W, la diminution de l'émissivité de la rue et l'augmentation de la température des murs pourraient tous augmenter l'amplitude de l'impact des structures 3-D et de leur rayonnement sur une mesure TIR (Fig. 9 - Fig. 10).

4. Développement d'une méthode sans connaissance préalable (PKF) pour une détermination précise du LST à partir de données satellitaires

Les avantages et les inconvénients complémentaires des algorithmes SW et TES ont été étudiés pour développer une nouvelle méthode qui ne requiert aucune connaissance préalable (PKF : Prior-Knowledge-Free) pour une détermination précise du LST à partir des données satellite. Premièrement, des paires de canaux spécifiques dans la région spectrale TIR ont été déterminées pour obtenir des températures de rayonnement au niveau du sol à partir d'observations par satellite en utilisant une méthode similaire à la méthode

SW (Eq. 10). Ensuite, la LST peut être obtenue avec précision, sans aucune connaissance préalable de LSE ou de paramètres atmosphériques, après application de la méthode TES à ces températures   au niveau du sol (Fig. 11).

$$T_{gi} = A_0 + A_1 T_i + A_2(T_i - T_j) + A_3(T_i - T_j)^2 \qquad \text{Eq. 10}$$

dans lequelle, l'indice i, j sont le canal i et le canal j; T_{gi}, T_i et T_j sont respectivement la température de rayonnement sol, la température de rayonnement du canal i et la température de rayonnement du canal j; A_0, A_1, A_2 et A_3 sont des constantes.
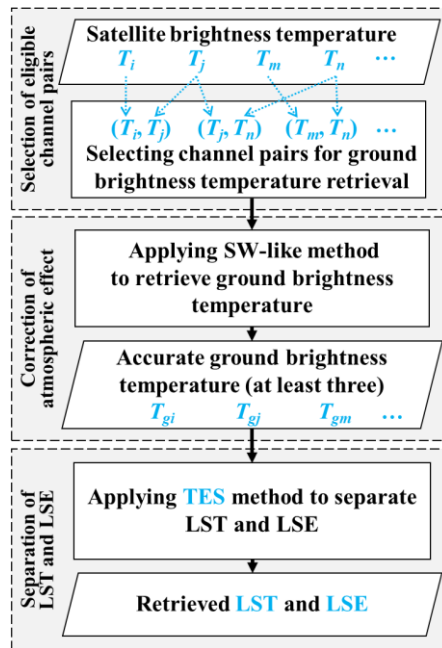

Fig. 11. Illustration de la méthode proposée pour une détermination précise du LST.

La procédure utilisée pour déterminer les paires de canaux éligibles pour une détermination précise de la température de rayonnement sur le terrain est donnée dans la Fig. 12.
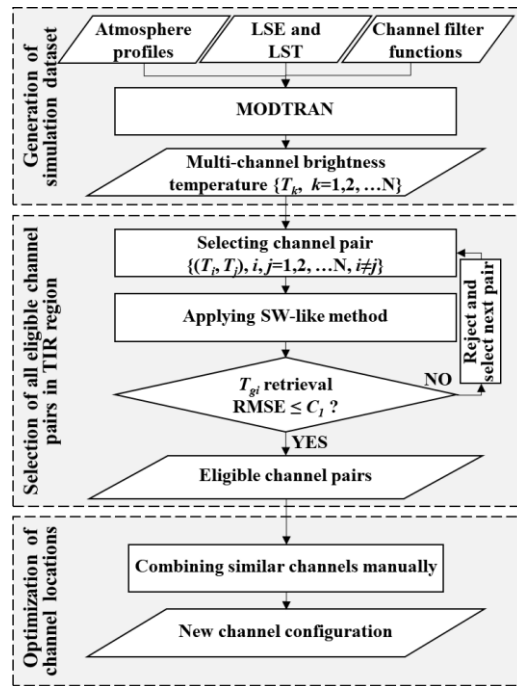
Fig. 12. Organigramme pour déterminer la nouvelle configuration de canal. T_k, T_i, et T_j sont des températures de rayonnement de canal, C_l est une constante pour tester si une paire de canaux est éligible pour récupérer une température de rayonnement sur le terrain précise.

Enfin, cinq canaux centrés sur 8,6 µm, 9,0 µm, 10,4 µm, 11,3 µm et 12,5 µm ont été sélectionnés comme option appropriée. Selon des simulations, le T_{gi} à 8,6 µm, 9,0 µm et 10,4 µm pourrait être acquis avec une précision d'environ 0,65 K (Fig. 13a), et la LST pourrait être récupéré avec une précision de ≤1,0 K en utilisant ces trois T_{gi} (Fig. 13b).
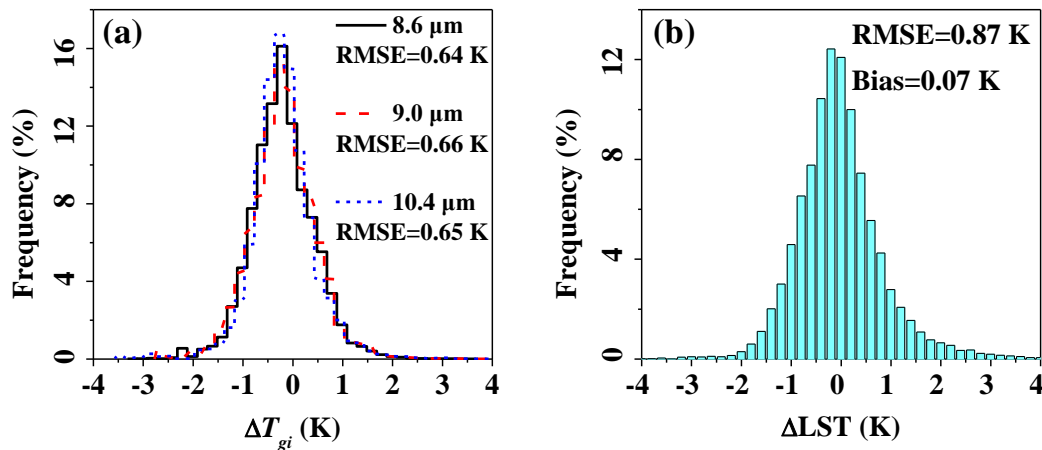

Fig. 13. (a) Histogrammes des résidus entre la température de rayonnement sol obtenue   et vraie (T_{gi}) pour différents canaux. (b) Histogramme des résidus entre la LST obtenue et vraie.

Cette configuration de canal sélectionnée a également été appliquée aux observations satellitaires réelles d'AIRS en Australie et comparée au produit MODIS LST (Fig. 14).
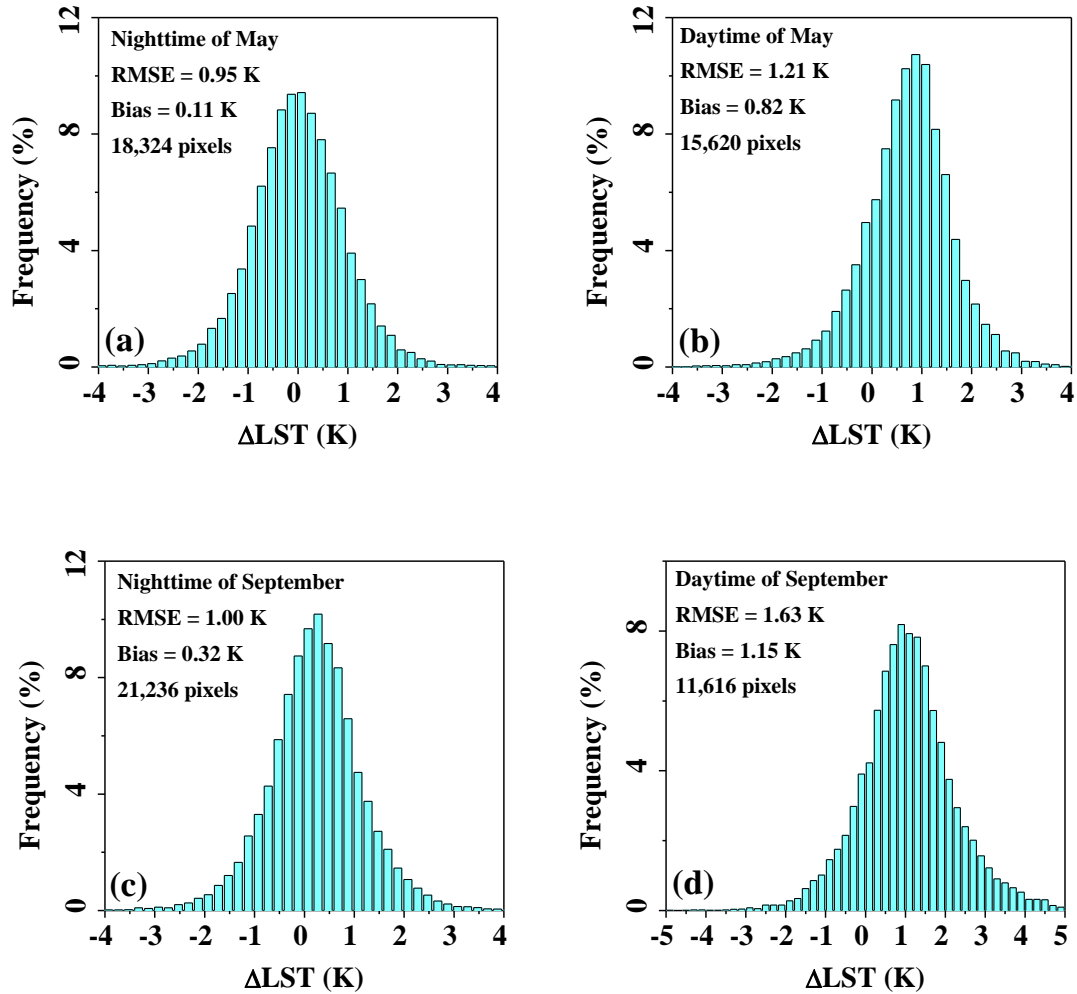
Fig. 14. Histogrammes résiduels de la LST obtenue pour les observations de l'Australie acquises (a) la nuit en mai 2018; (b) pendant la journée de mai 2018; (c) la nuit en septembre 2018; et (d) pendant la journée de septembre 2018.

Il est démontré que les écarts entre le résultat obtenu et le produit MODIS est meilleurs pour les observations nocturnes que pour les observations diurnes, avec une RMSE de détermination de la LST d'environ 1,0 K et 1,6 K, respectivement.

5. Exploration pour le développement d'une méthode améliorée de détermination du LST pour les mesures TIR à haute résolution spatiale en zones urbaines

Sur la base des recherches dans les trois sections ci-dessus, une exploration primaire sur le développement d'une méthode améliorée de détermination du LST pour les mesures TIR

à haute résolution spatiale des zones urbaines a été donnée (Fig. 15). Pour être précis, tout d'abord, la méthode PKF a été appliquée directement aux mesures TIR urbaines pour obtenir les premières déterminations de la LST. Ensuite, le FAERTM et l'ATIMOU ont été combinés avec la méthode PKF pour traiter l'effet d'adjacence et les impacts 3-D. Enfin, à l'aide d'un processus d'itération, la LST urbain améliorée a pu enfin être obtenue.
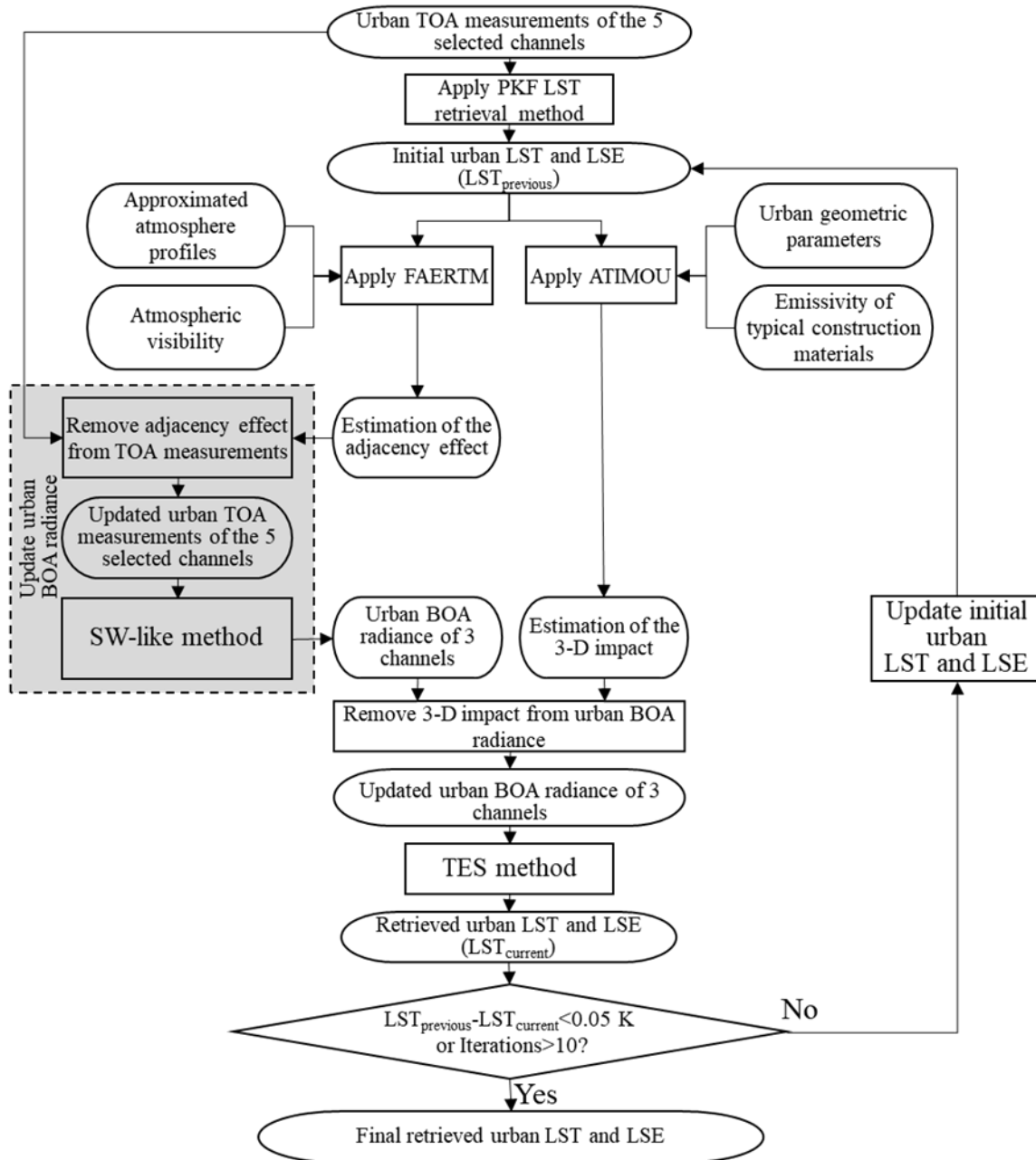

Fig. 15. Conception globale du schéma de la méthode améliorée de détermination de la LST pour les mesures TIR à haute résolution spatiale en zones urbaines.

Sur la base des profils atmosphériques typiques, des spectres d'émissivité des matériaux de construction et des paramètres géométriques d'un canyon de rue, un ensemble de

données de mesures TIR simulées à haute résolution spatiale des zones urbaines a été réalisé. Au total, 331,776 cas ont été générés, sur la base desquels, la méthode améliorée de détermination du LST a été évaluée (Fig. 16 - Fig. 17).
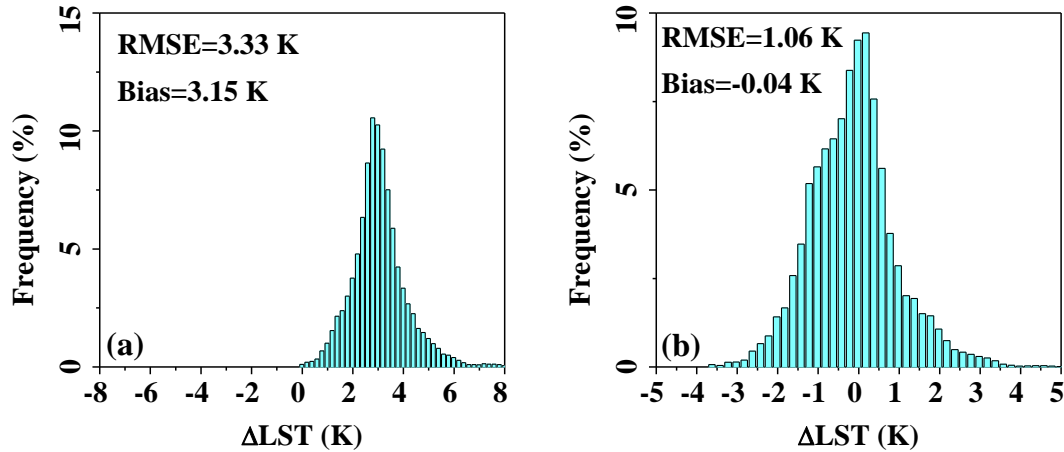

Fig. 16. Histogramme des résidus concernant (a) les déterminations initiales de la LST urbaine obtenues en appliquant la méthode PKF directement aux mesures TOA urbaines, et (b) les déterminations finales de la LST urbaine obtenues en appliquant la méthode proposée.
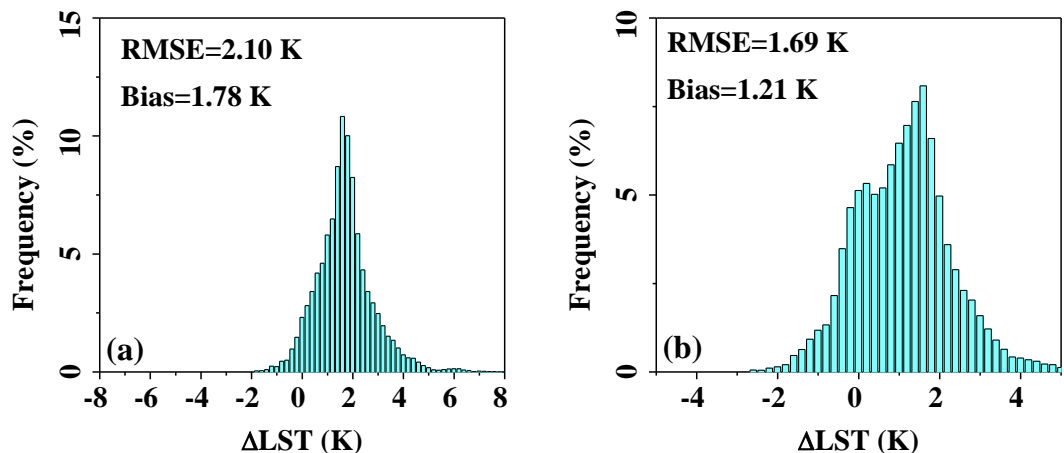
Fig. 17. Histogramme des résidus concernant (a) les déterminations finales de la LST urbaine obtenues en appliquant la méthode proposée avec correction de l'effet d'adjacence mais sans correction des impacts 3-D, et (b) les déterminations finales de la LST urbaine obtenues en appliquant la proposition sans correction de l'effet d'adjacence mais avec correction des impacts 3-D.

Il est démontré que le RMSE du LST récupéré est passé de 3,33 K à 1,06 K après la mise en œuvre de la méthode proposée. De plus, indépendamment de l'effet d'adjacence dans la méthode de détermination LST proposée, le RMSE de la détermination LST pourrait passer de 1,06 K à 1,69 K, tandis que le RMSE de la détermination LST passerait de 1,06

K à 2,10 K si les impacts 3-D ont été négligés. Cela indique que l'effet d'adjacence et les impacts 3-D doivent être pris en compte lors de la détermination du LST urbain à partir de mesures TIR à haute résolution spatiale.

6. Conclusions and perspectives

Cette thèse se concentre sur l'étude des facteurs influençant les mesures TIR par satellite et la précision de la détermination de la LST, dont le but final est de développer une méthode de détermination de la LST améliorée pour les mesures TIR par satellite à haute résolution spatiale en zones urbaines.

Tout d'abord, un modèle de simulation d'effet d'adjacence physique, FAERTM, a été développé et utilisé pour quantifier l'effet d'adjacence sur les mesures TIR pour différentes conditions atmosphériques et d'imagerie. Il fournit un outil utile pour traiter l'effet d'adjacence.

Deuxièmement, un nouveau modèle analytique de transfert radiatif TIR (ATIMOU), qui tient compte de l'impact des structures 3-D et de leur rayonnement sur les mesures TIR, a été développé, qui pourrait être utilisé pour corriger l'impact des structures 3-D et de leur rayonnement pendant la détermination de LST urbaine.

Troisièmement, une méthode sans connaissance préalable (PKF) a été développée qui pourrait être utilisée pour récupérer LST avec précision sans utiliser d'informations supplémentaires sur l'atmosphère et LSE sur la base d'une nouvelle configuration de canaux TIR.

Enfin, une exploration primaire a été fournie sur le développement d'une méthode améliorée de détermination du LST pour les mesures TIR à haute résolution spatiale des zones urbaines basée sur le FAERTM, l'ATIMOU et la méthode de PKF LST. Nous considérons pense que la méthode améliorée de détermination de la LST est en mesure d'améliorer considérablement la précision de la détermination de la LST urbaine.

Néanmoins, cette thèse a ses limites et nécessite des recherches supplémentaires à l'avenir :

(1) Les angles de vision devront être pris en compte dans l'FAERTM.

(2) Les canyons de rue asymétriques devront être pris en compte dans l'ATIMOU.

(3) Les angles de vision, la teneur en vapeur d'eau, et les observations multi-canaux

pourraient être pris en compte dans la méthode de PKF LST pour améliorer ses performances.

(4) Plus d'expériences simulées et des expériences sur le terrain dans les zones urbaines sont souhaitées pour valider l'exactitude absolue des LST urbaines obtenues. Et les nouvelles méthodes de récupération du LST avec prise en compte de l'effet d'adjacence et l'impact des structures 3-D et de leur rayonnement en théorie doivent être développées.

Références

Anderson, M.C., Norman, J.M., Kustas, W.P., Houborg, R., Starks, P.J., & Agam, N. (2008). A thermal-based remote sensing technique for routine mapping of land-surface carbon, water and energy fluxes from field to regional scales. *Remote Sensing of Environment, 112*, 4227-4241.

Bureau, P.R. (2019). 2019 world population data sheet

Hulley, G.C., Ghent, D., Göttsche, F.M., Guillevic, P.C., Mildrexler, D.J., & Coll, C. (2019). Land surface temperature. In G.C. Hulley, & D. Ghent (Eds.), *Taking the Temperature of the Earth* (pp. 57-127): Elsevier.

Li, Z.-L., Tang, B.-H., Wu, H., Ren, H., Yan, G., Wan, Z., Trigo, I.F., & Sobrino, J.A. (2013). Satellite-derived land surface temperature: current status and perspectives. *Remote Sensing of Environment, 131*, 14-37.

Zheng, X., Gao, M., Li, Z.-L., Chen, K.-S., Zhang, X., & Shang, G. (2020). Impact of 3-D structures and their radiation on thermal infrared measurements in urban areas. *IEEE Transactions on Geoscience and Remote Sensing, Early Access*, 1-15.

Zheng, X., Li, Z.-L., Nerry, F., & Zhang, X. (2019a). A new thermal infrared channel configuration for accurate land surface temperature retrieval from satellite data. *Remote Sensing of Environment, 231*, 1-12.

Zheng, X., Li, Z.-L., Zhang, X., & Shang, G. (2019b). Quantification of the adjacency effect on measurements in the thermal infrared region. *IEEE Transactions on Geoscience and Remote Sensing, 57*, 9674-9687.

TRAVAUX PUBLIES LORS DE LA THESE

Journal papers:

X. Zheng, Z.-L. Li, F. Nerry, and X. Zhang, "A new thermal infrared channel configuration for accurate land surface temperature retrieval from satellite data," Remote Sensing of Environment, vol. 231, no. (2019) 111216, pp. 1-12, May 2019.

X. Zheng, Z.-L. Li, X. Zhang, and G. Shang, "Quantification of the adjacency effect on measurements in the thermal infrared region," IEEE Transactions on Geoscience and Remote Sensing, vol. 57, no. 12, pp. 9674-9687, Jul. 2019.

X. Zheng, M. Gao, Z.-L. Li, K.-S. Chen, X. Zhang, and G. Shang, "Impact of 3-d structures and their radiation on thermal infrared measurements in urban areas," IEEE Transactions on Geoscience and Remote Sensing, vol. Early Access, no. Early Access, pp. 1-15, May 2020.

Conference proceedings:

X. Zheng, Z.-L. Li, K.-S. Chen, X. Zhang, and G. Shang (2019). Assessment of the urban three-dimensional structural influence on the satellite thermal infrared measurement. In, *IEEE PhotonIcs & Electromagnetics Research Symposium – Spring* (pp. 377-386), Rome, Italy: IEEE.

Xiaopo ZHENG

Land surface temperature retrieval in urban areas from high spatial resolution thermal infrared data

Résumé

Mots-clés: LST, TIR, transfert radiatif, effet d'adjacence, tridimensionnel

La température de la surface terrestre (LST) est un paramètre très important. Cependant, certains facteurs influencent encore la précision de la récupération du LST dans les zones urbaines, mais n'ont pas encore été bien pris en compte dans les algorithmes de récupération du LST existants: (1) l'effet d'adjacence dans la région spectrale infrarouge thermique (TIR); (2) l'impact des structures tridimensionnelles et de leur rayonnement; (3) la dépendance de la connaissance préalable de l'atmosphère et/ou de l'émissivité de la surface terrestre. Dans cette thèse, deux modèles de transfert radiatif et une nouvelle méthode de récupération du LST ont été développés pour traiter ces trois facteurs, sur ces modèles, une méthode de récupération du LST urbain à partir de mesures TIR à haute résolution spatiale a été donnée. Les résultats montrent que la précision de récupération du LST urbain pourrait être améliorée d'environ 2,0 K, indiquant les bonnes performances de la méthode proposée.

Résumé en anglais

Keywords: LST, TIR, radiative transfer, adjacency effect, three-dimensional

Land surface temperature (LST) is an important parameter of the Earth surface. However, there are still some factors influencing the urban LST retrieval accuracy but have not been well addressed in existing LST retrieval algorithms: (1) the adjacency effect in the thermal infrared (TIR) spectral region; (2) the impact of the three-dimensional structures and their radiation on the TIR measurements; (3) the dependence of existing LST retrieval algorithms on the information of atmosphere and/or the Earth surface emissivity. In this thesis, two forward radiative transfer models and one new LST retrieval method have been developed to deal with these three factors, based on which, a preliminary exploration on developing an improved urban LST retrieval method from high spatial resolution satellite TIR measurements has been given. Results show that the urban LST retrieval accuracy could be improved by about 2.0 K, indicating the good performance of the proposed method.